Probing IrTe₂ crystal symmetry by polarized Raman scattering

N. Lazarević,[1] E. S. Bozin,[2] M. Šćepanović,[1] M. Opačić,[1] Hechang Lei (雷和畅),[2] C. Petrovic,[2] and Z. V. Popović[1]

[1]*Center for Solid State Physics and New Materials, Institute of Physics Belgrade, University of Belgrade,*
Pregrevica 118, 11080 Belgrade, Serbia
[2]*Condensed Matter Physics and Materials Science Department, Brookhaven National Laboratory, Upton, New York 11973-5000, USA*

Polarized Raman scattering measurements on IrTe₂ single crystals carried out over the 15–640 K temperature range, and across the structural phase transition, reveal different insights regarding the crystal symmetry. In the high temperature regime three Raman active modes are observed at all of the studied temperatures above the structural phase transition, rather than two as predicted by the factor group analysis for the assumed $P\bar{3}m1$ symmetry. This indicates that the actual symmetry of the high temperature phase is lower than previously thought. The observation of an additional E_g mode at high temperature can be explained by doubling of the original trigonal unit cell along the c axis and within the $P\bar{3}c1$ symmetry. In the low temperature regime (below 245 K) the other Raman modes appear as a consequence of the symmetry lowering phase transition and the corresponding increase of the primitive cell. All of the modes observed below the phase transition temperature can be assigned within the monoclinic crystal symmetry. The temperature dependence of the Raman active phonons in both phases is mainly driven by anharmonicity effects. The results call for reconsideration of the crystallographic phases of IrTe₂.

I. INTRODUCTION

Although known for some time [1,2], the interest in IrTe₂ has been renewed recently with the discovery of superconductivity [3–6]. By doping this layered compound with Pt, Pd, and Cu, the phase transition which occurs at low temperatures [7] is suppressed and superconductivity emerges [3–6,8]. At room temperature IrTe₂ has a trigonal symmetry with edge-sharing IrTe₆ octahedra forming layers stacked along the c axis [7], as shown in Fig. 1. As temperature is decreased, the system undergoes a symmetry lowering phase transition in the temperature range between 220 and 280 K, with the exact transition temperature T_{PT} presumably depending on the sample form (powder versus single crystal) and the thermal cycle details (cooling or warming) [3–7,9]. The phase transition is accompanied by a hump in electrical resistivity and a drop in magnetic susceptibility [10], anomalies reminiscent of those associated with the onset of a charge-density-wave (CDW) state observed in other TX_2 systems [11]. However, the exact nature of the low temperature phase remains controversial, since no signatures of the CDW gap in IrTe₂ have been seen in angle resolved photoemission and optical spectroscopy studies [5,9,10]. Recent band structure calculations combined with x-ray absorption spectroscopy measurements suggest that the dramatic change in the interlayer and intralayer hybridizations could play an important role in the structural phase transition of IrTe₂ [6]. More recently, it has also been suggested that the depolymerization of the polymeric Te-Te bonds might be responsible for the structural phase transition [9].

Although prior crystallographic analyses showed that the IrTe₂ crystal structure changes from trigonal to monoclinic with decreasing temperature, the low temperature structure is still a subject of debate [7]. It was argued that the initially assigned monoclinic $C2/m$ symmetry cannot fully describe the structure below the phase transition [11–13]. Consequently, the proposed crystal symmetry was further lowered down to

triclinic $P\bar{1}$ [11] and even $P1$ [13]. Moreover, it was also suggested that the trigonal and monoclinic structures coexist intrinsically below the phase transition [12]. The nature of the phase transition as well as the symmetry of the low temperature phase therefore still remain open questions.

Important information concerning the symmetry of the crystal system can be obtained by utilizing the properties of Raman spectroscopy and by performing the measurements in different polarization configurations whereby one can probe different scattering channels. Raman spectroscopy also emerges as a valuable tool for detecting the intrinsic phase separation [14].

Here we present results of a systematic Raman scattering study on IrTe₂ single crystals. The spectra were collected in different scattering geometries at various temperatures. The room temperature Raman spectra were analyzed within the trigonal crystal symmetry. Three instead of two peaks, which are predicted by the factor group analysis (FGA) for the $P\bar{3}m1$ space group, are observed in the Raman spectra, suggesting a different crystal symmetry of IrTe₂ in the high temperature phase from that previously assumed. The same phonon structure persists at $T \gg T_{PT}$, indicating that it is a true characteristic of the high temperature phase. At temperatures below $T_{PT} = 245$ K, the clear fingerprint of the first order structural phase transition is observed in the Raman spectra. The observed modes are interpreted within the monoclinic crystal symmetry. No signatures of the trigonal unit cell presence have been detected in the low temperature Raman scattering spectra. All temperature induced effects in both phases are mostly anharmonic. These observations provide important insights and constraints for possible crystal symmetries of this system in different temperature regimes.

II. EXPERIMENT

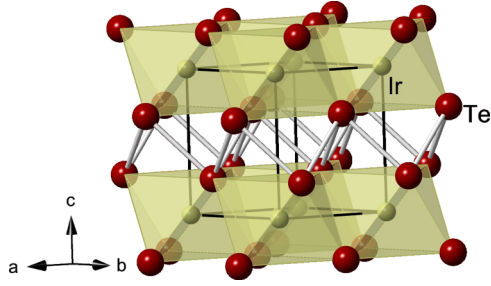Single crystals of IrTe₂ were prepared by the self-flux method. Ir and Te were mixed in an 18:82 stoichiometric

FIG. 1. (Color online) Crystal structure of $IrTe_2$ in the trigonal phase. Solid lines represent a single $P\bar{3}m1$ unit cell, with yellow (red) spheres indicating the positions of Ir (Te).

ratio, heated in alumina crucibles under an Ar atmosphere up to 1160 °C, kept at that temperature for 24 h, and then cooled to 400 °C over 130 h. Excess Te flux was removed at 400 °C by centrifugation. Platelike mm-size crystals were obtained. Magnetization and resistivity data were measured by warming the sample from 5 K. They are in good agreement with published values [3].

Raman scattering measurements were performed using a JY T64000 Raman system with 1800/1800/1800 grooves/mm gratings and a TriVista 557 Raman system with the 900/900/1800 grooves/mm gratings combination, both in a backscattering micro-Raman configuration. The 514.5 nm line of a mixed Ar^+/Kr^+ gas laser was used as an excitation source. High temperature measurements were preformed in an Ar environment by using a Linkam THGS600 heating stage. Low temperature measurements were performed using a KONTI CryoVac continuous flow cryostat with a 0.5 mm thick window in the warming regime. Complementary atomic pair distribution function (PDF) measurements at 300 K were performed on a finely pulverized sample at the X17A beamline of the National Synchrotron Light Source (NSLS) at Brookhaven National Laboratory, utilizing a 67.42 keV x-ray beam within a commonly used rapid-acquisition setup [15] featuring a sample to detector distance of 204.25 mm, and with access to a wide momentum transfer range up to 28 $Å^{-1}$. Standard corrections, PDF-data processing, and structure modeling protocols were utilized, as described in detail elsewhere [16].

III. RESULTS AND DISCUSSION

$IrTe_2$ crystallizes in a trigonal type of structure ($P\bar{3}m1$ space group) with one molecular unit per unit cell (Fig. 1) [7,18]. The crystal structure consists of $IrTe_2$ layers which are made up of edge-sharing $IrTe_6$ octahedra. Short Te-Te bonds between adjacent $IrTe_2$ result in three-dimensional polymeric networks, thereby reducing the c/a ratio in comparison with the standard hexagonal closed packing of the CdI_2 structure [1,9,19]. This is related to the Ir^{+3} state and the fractional oxidation state of Te anions ($Te^{-1.5}$) [2,9].

A. High temperature phase

Figure 2 shows the room temperature polarized Raman scattering spectra of $IrTe_2$ single crystals measured from the (001) plane of the sample. Although the FGA for the
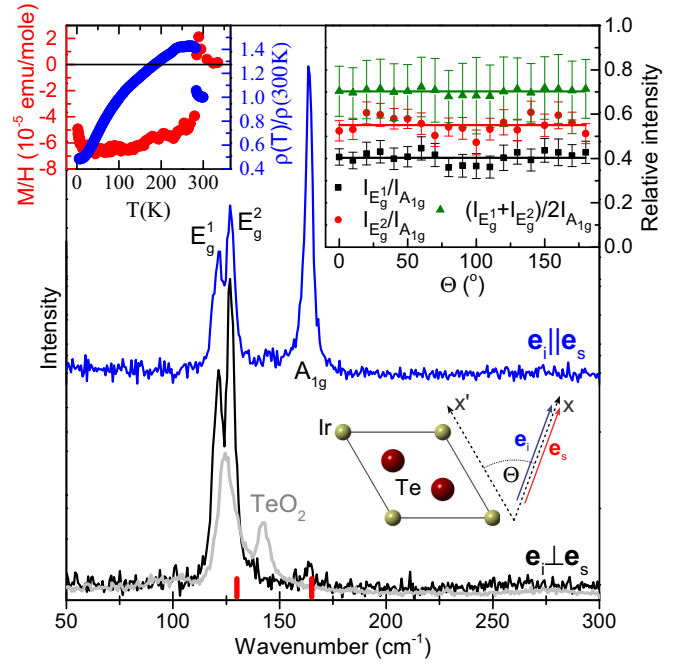

FIG. 2. (Color online) Room temperature Raman scattering spectra of $IrTe_2$ measured using a JY T64000 Raman system in different polarization configurations. Gray lines represent the spectra of TeO_2 with scaled intensity. Red markers represent phonon energies at Γ point calculated by Cao *et al.* [11]. Inset on the left: Magnetization and resistivity data measured by warming the sample from the base temperature. Inset on the right: Relative intensities of the Raman active modes measured in a parallel polarization configuration for different orientations of the sample with respect to the laboratory axis.

$P\bar{3}m1$ space group predicts only two Raman active modes ($A_{1g} + E_g$) to be observed in the scattering experiment, three peaks are clearly distinguished in the data. A contribution to the Raman spectra originating from scattering on possible TeO_2 impurities can be safely excluded (see Fig. 2). According to the selection rules for the trigonal system, summarized in Table I, the A_{1g} mode can only be observed in a parallel but not in a crossed polarization configuration, whereas the E_g mode can be observed in both parallel and crossed polarization configurations. Consequently, the peak at about 164 cm^{-1}, which is indeed observed in a parallel but not in a cross polarization configuration, is attributed to the A_{1g} symmetry mode. The energy of this mode is in very good agreement with the calculated value [11] (red mark in Fig. 2). Whereas the numerical calculations [11] further predict a single E_g mode at about 130 cm^{-1} to be observed in the Raman scattering experiment, two peaks at about 121 and 126 cm^{-1} are unambiguously observed in the data in this energy range (see Fig. 2). These modes are observed in both parallel and cross polarization configurations, which suggests their E_g symmetry. The appearance of two modes in the energy range where only one mode is expected indicates that the original crystal symmetry assignment for the high temperature phase may be inadequate, and that the actual symmetry is in fact lower. We consider the issue of the symmetry of the high temperature phase in more detail next.

TABLE I. Considerations of Raman tensors for three different crystal systems and the Raman mode distribution in the Γ point and various space groups of interest for IrTe$_2$.

Crystal system	Raman tensors [17]			Raman modes
Trigonal ($O_z \parallel C_3\ O_y \parallel C_2$)	$\hat{R}_{A_{1g}} = \begin{pmatrix} a & 0 & 0 \\ 0 & a & 0 \\ 0 & 0 & b \end{pmatrix}$	$\hat{R}_{E_g} = \begin{pmatrix} -c & 0 & 0 \\ 0 & c & 0 \\ 0 & 0 & 0 \end{pmatrix}, \begin{pmatrix} 0 & c & 0 \\ c & 0 & 0 \\ 0 & 0 & 0 \end{pmatrix}$		$\Gamma_{P\bar{3}m1} = A_{1g} + E_g$ $\Gamma_{P\bar{3}c1} = A_{1g} + A_{2g}(\text{silent}) + 2E_g$
Monoclinic ($O_y \parallel C_2$)	$\hat{R}_{A_g} = \begin{pmatrix} b & 0 & d \\ 0 & c & 0 \\ d & 0 & a \end{pmatrix}$	$\hat{R}_{B_g} = \begin{pmatrix} 0 & f & 0 \\ f & 0 & e \\ 0 & e & 0 \end{pmatrix}$		$\Gamma_{C2/m} = 2A_g + B_g$
Triclinic	$\hat{R}_A = \hat{R}_{A_g} = \begin{pmatrix} a & d & e \\ d & b & f \\ e & f & c \end{pmatrix}$			$\Gamma_{P\bar{1}} = 21A_g$ $\Gamma_{P1} = 222A$

The first possibility is that the IrTe$_2$ symmetry is lowered at room temperature to some t subgroup of the $P\bar{3}m1$ [20]. This would imply splitting of a double degenerate E_g mode into an A_g-B_g doublet [21]. Hereby the obtained modes would display different angular Raman intensity dependencies as the sample orientation is varied in a parallel polarization configuration (see Fig. 2). On the contrary (as can be seen in the inset of Fig. 2), both modes at 121 and 126 cm^{-1} exhibit the same angular intensity dependence, thereby excluding the possibility of the E_g mode splitting, i.e., symmetry lowering to some t subgroup of the $P\bar{3}m1$. Furthermore, it confirms the E_g nature of the 121 and 126 cm^{-1} modes since, for a trigonal system (see Table I), both A_{1g} and E_g mode intensities are independent on the sample orientation when measured in a parallel polarization configuration.

The second possibility which could explain the observed appearance of the two E_g modes instead of a single E_g mode is the symmetry change to some k subgroup of $P\bar{3}m1$ [20]. The simplest option is $P\bar{3}c1$ ($Z = 2$) with Ir atoms located on the 2b site and Te atoms at the 4d site. The $P\bar{3}c1$ unit cell is built by doubling of the $P\bar{3}m1$ unit cell along the c axis (see Fig. 1). The FGA for the $P\bar{3}c1$ predicts three Raman active modes to be observed in the Raman scattering experiment ($A_{1g} + 2E_g$), which is in complete agreement with our findings. To further verify the plausibility of this assumption, we performed a structural analysis of room temperature x-ray PDF data of IrTe$_2$ using the $P\bar{3}c1$ model. The fit results are shown in Fig. 3 and summarized in Table II.

Importantly, the observed phonon structure and, consequently, the crystal $P\bar{3}c1$ symmetry persist at temperatures
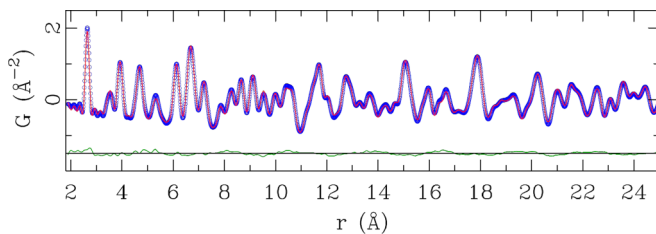
$T \gg T_{PT}$ deep in the high temperature regime, as is evident from Fig. 4, indicating that these are the characteristics of the high temperature phase. As the temperature is increased, all of the modes are shifted toward lower energies and become progressively broader (see the inset of Fig. 4). All of the changes of the spectra induced by a temperature increase are in accordance with the well known anharmonicity model [22–24].

B. Low temperature phase

By lowering the temperature, IrTe$_2$ undergoes the phase transition in the range between 220 and 280 K [7,11,13]. The origins of the phase transition as well as the crystal symmetries of IrTe$_2$ at low temperatures are still under vigorous debate [7,11–13].

Polarized Raman scattering spectra of IrTe$_2$ measured at low temperatures (between 15 and 300 K) in parallel and cross polarization configurations are presented in Fig. 5. Significant changes in the spectra in both polarization configurations are observed around 245 K. A lower transition temperature is a consequence of the local heating effects of the sample by the laser beam. Unlike in the case of a canonical CDW phase transition where additional modes gradually appear [25], the observed sudden change in the phonon spectra suggests the first order character of the phase transition. The existence of at least 11 peaks in the low temperature phase indicates lowering of the symmetry and/or an increase of the unit cell size.

Figure 6 shows polarized Raman scattering spectra of IrTe$_2$ measured at 15 K in parallel and cross polarization configurations. A significant difference in the spectra measured in the parallel and crossed polarization configurations

FIG. 3. (Color online) Room temperature x-ray PDF of IrTe$_2$: Experimental data (blue open symbols), $P\bar{3}c1$ model (red solid line), and difference curve (green solid line) which is offset for clarity. Structural parameters are summarized in Table II.

TABLE II. Structural parameters for the $P\bar{3}c1$ phase obtained from PDF analysis at 300 K. The lattice parameters are $a = b = 3.929(4)$ Å, $c = 10.805(2)$ Å. U_{ij} (Å$^2 \times 10^3$) are nonzero components of the displacement tensor.

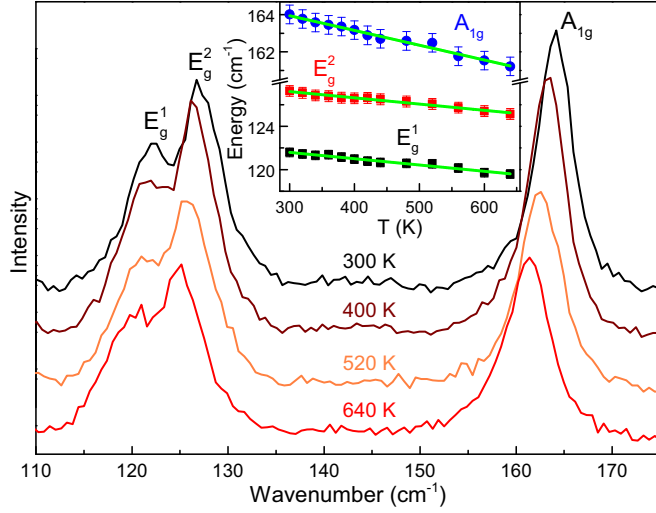| Atom	x	y	z	$U_{11} = U_{22}$	U_{33}
Ir	0	0	0	6(2)	6(3)
Te	1/3	2/3	0.126(1)	7(2)	9(4)
			$\chi^2 = 0.002$		
			$R_{wp} = 0.106$		

FIG. 4. (Color online) Raman scattering spectra of IrTe$_2$ single crystals measured at various temperatures, as indicated, in the high temperature regime using a TriVista 557 Raman system. Inset: Energy temperature dependence of the A_{1g}, E_g^1, and E_g^2 Raman active modes. The solid green lines represent calculated spectra by using the standard three-phonon anharmonicity model [22], where [$\omega_0 = 123.4(2)$ cm^{-1}, $C = 0.26(2)$ cm^{-1}], [$\omega_0 = 129.0(2)$ cm^{-1}, $C = 0.27(2)$ cm^{-1}], and [$\omega_0 = 160.4(2)$ cm^{-1}, $C = 0.48(3)$ cm^{-1}] are the best fit parameters for the E_g^1, E_g^2, and A_{1g} Raman active modes, respectively.

indicates the existence of the two separate scattering channels in the low temperature phase. Symmetry arguments suggest that in the case of the triclinic crystal structure only one channel can be observed. Due to the proposed orientation of the triclinic lattice [11,13] in relation to the trigonal lattice,
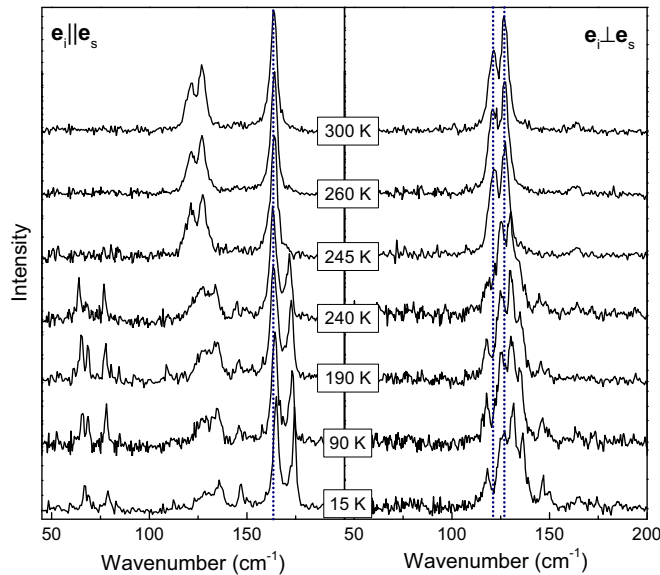

FIG. 5. (Color online) Polarized Raman scattering spectra of IrTe$_2$ measured at various temperatures, as indicated, in the low temperature regime using a JY T64000 Raman system in parallel and cross polarization configurations. The spectra were measured by warming the sample from 15 K. Dotted vertical lines represent a guide to the eyes.
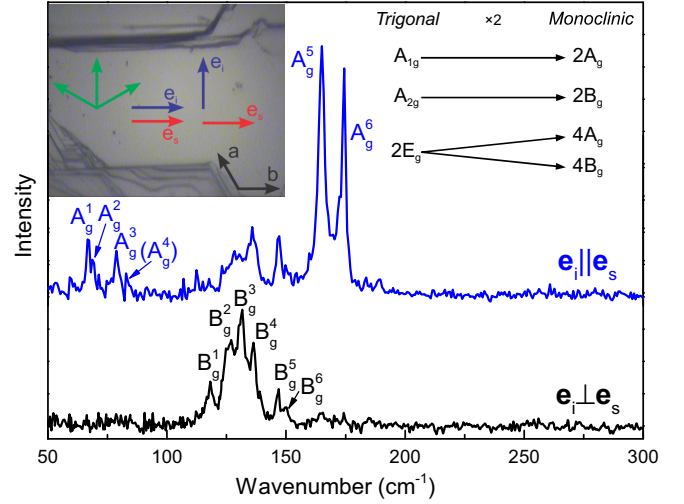

FIG. 6. (Color online) Polarized Raman scattering spectra of IrTe$_2$ measured at 15 K using a JY T64000 Raman system in parallel and cross polarization configurations. Inset on the left: Image of the IrTe$_2$ sample. Inset on the right: Correlation diagram connecting Raman active phonons for trigonal and monoclinic types of structures.

the contribution to the scattering intensity (in our scattering geometry) would come from nearly all the components of the Raman tensor (see Table I) and the cancellation of some Raman modes in different polarization configurations is highly unlikely. Furthermore, for both $P1$ and $P\bar{1}$ space groups, a substantially larger number of Raman modes is expected to be observed in the measured spectra. All this suggests that the IrTe$_2$ crystal symmetry in the low temperature phase should be higher than triclinic ($P1$ or $P\bar{1}$). The next crystal system with two different scattering channels is monoclinic (see Table I). The obtained spectra may be interpreted within the monoclinic crystal symmetry provided that the optical axis of the low temperature phase is orthogonal to the direction of incident light in the Raman scattering experiment, i.e., if it lies in the (001) plane of the trigonal phase. This is consistent with the picture proposed by Matsumoto *et al.* [7]. At this point one should have in mind that symmetry breaking may occur along three equivalent directions, as indicated by the green arrows in the left inset of Fig. 6. For generality we assume the contributions from all three possible orientations. Consequently, one may expect the appearance of the B_g modes in both parallel and cross polarization configurations. Although the A_g modes may be also observed in both parallel and cross polarization configurations (with the assumption of twinning), in the crossed polarization configuration the intensity of the A_g modes depends on the $|b - c|^2$ and the cancellation can be easily achieved.

Following the previous arguments, the peaks at about 67, 69, 79, 165, and 174 cm^{-1} which can be observed in parallel but not in cross polarization configurations may be assigned as the A_g symmetry modes. We believe that the weak structure at about 83 cm^{-1} may also be the A_g symmetry mode, however, very low intensity prevents unambiguous assignation. Six peaks at about 118, 126, 131, 136, 148, and 150 cm^{-1} that can be observed in both parallel and crossed polarization configurations are assigned as the B_g symmetry modes.
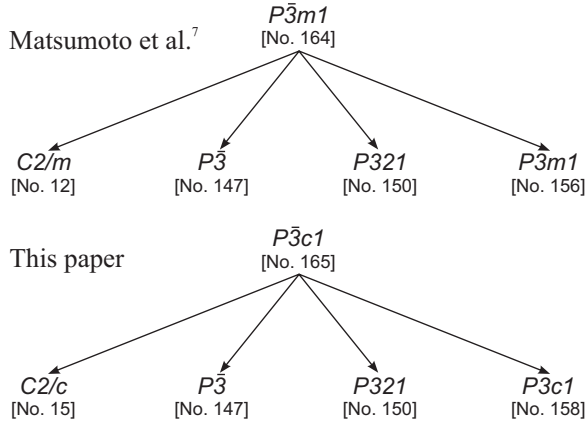
FIG. 7. Schematics of maximal nonisomorphic subgroup relations of the space group $P\bar{3}m1$ [7] (upper panel) and $P\bar{3}c1$ (lower panel) for the t subgroup. The number of the space group is given in the parentheses.

Although the properties of the observed Raman modes can, in principle, be interpreted within the monoclinic crystal system, the proposed [7] unit cell of the $C2/m$ symmetry group with $Z = 2$ cannot account for the number of observed Raman modes. According to FGA for $C2/m$ ($Z = 2$), only three modes are expected to be observed in the Raman scattering experiment (see Table I). Consequently, a larger unit cell within the monoclinic crystal system is needed to reproduce the observed Raman spectra. Following the previous arguments and the discussion regarding the symmetry of the high temperature phase, we may conclude that the space group symmetry of IrTe₂ at low temperatures should be searched for within the monoclinic $C2/c$ space group or some of its t subgroups (see Fig. 7) [20].

The temperature evolution of the Raman spectra (see Fig. 5) across the phase transition can be seen as the splitting of the two E_g modes into A_g (A_g^1-A_g^4) and B_g (B_g^1-B_g^4) quartets due to symmetry lowering and (at least) a two times increase of the primitive cell size (see the right inset in Fig. 6). The A_g^5 and A_g^6 most likely originate from the A_{1g} mode whereas the B_g^5 and B_g^6 originate from the A_{2g} mode of the trigonal phase. The absence of the E_g^1 and E_g^2 modes (within our experimental resolution), characteristic for the trigonal phase, in the low temperature Raman spectra of IrTe₂ suggests the absence of the trigonal lattice at low temperatures [12].

The temperature dependence of the energy and linewidth for the highest intensity Raman modes is shown in Fig. 8. A clear fingerprint of the first order phase transition is observed in both the energy and the linewidth of the observed modes. The solid lines represent the calculated spectra for the low temperature phase by using the three-phonon anharmonicity model [22]. Good agreement with the experimental data confirms that anharmonicity plays a major role in the temperature dependence of the temperature phase phonon self-energy below T_{PT}.

IV. CONCLUSION

A Raman scattering study of IrTe₂ single crystals has been presented. At room temperature, three instead of two
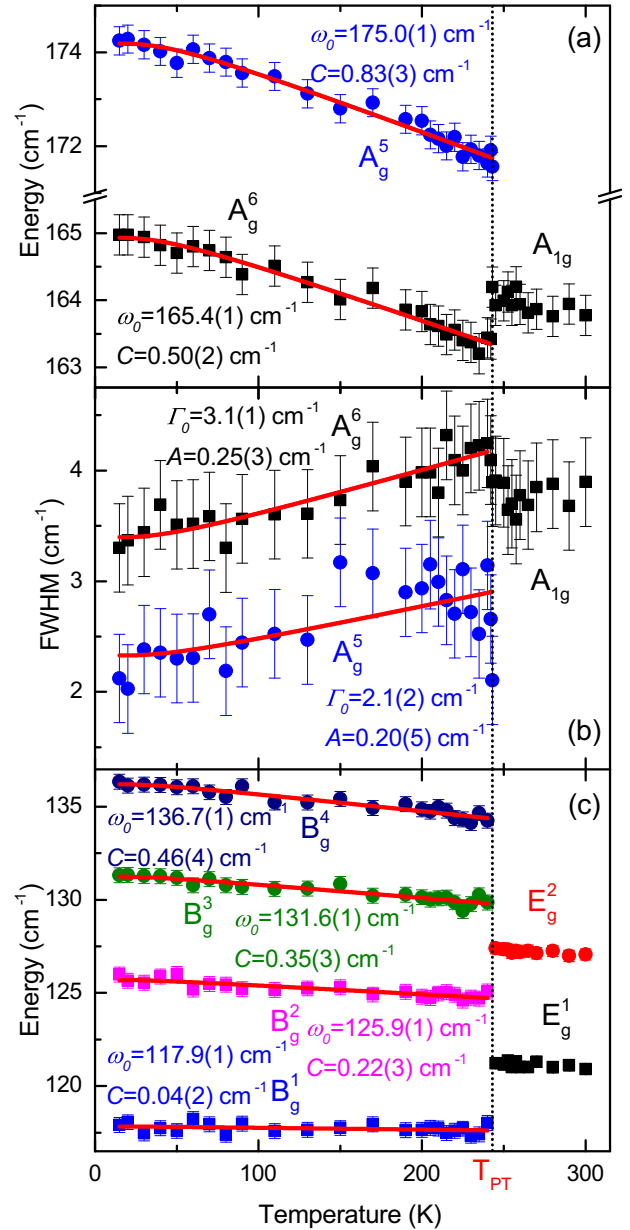

FIG. 8. (Color online) Temperature dependence of the highest intensity Raman mode energy (a) and (c) and linewidth (b). Solid lines represent the calculated spectra by using the standard three-phonon anharmonicity model [22]. The spectra were measured by warming the sample from 15 K.

Raman active modes predicted by the factor group analysis for the $P\bar{3}m1$ symmetry group are observed. The Raman data showed that the $P\bar{3}c1$ rather than the $P\bar{3}m1$ crystal symmetry is needed to describe the phonon structure of IrTe₂ at room temperature. The sudden change in the Raman spectra below $T_{PT} = 245$ K revealed the first order structural phase transition. The properties of the phonon spectra below T_{PT} are well interpreted within the monoclinic crystal symmetry. The splitting of the E_g modes at the T_{PT} comes from the symmetry lowering and the increase in the size of the unit cell. We believe that the space group symmetry of IrTe₂ at low temperatures should be searched for within the monoclinic $C2/c$ space group or some of its t subgroups. Further structural

investigations of both trigonal and monoclinic phases of $IrTe_2$ are needed. Apart from the symmetry change at T_{PT}, the temperature dependence of the energy and linewidth of the Raman active modes of $IrTe_2$ is mostly anharmonic.

ACKNOWLEDGMENTS

[1] S. Jobic, P. Deniard, R. Brec, J. Rouxel, A. Jouanneaux, and A. N. Fitch, Z. Anorg. Allg. Chem. **598**, 199 (1991).

[2] S. Jobic, R. Brec, and J. Rouxel, J. Solid State Chem. **96**, 169 (1992).

[3] J. J. Yang, Y. J. Choi, Y. S. Oh, A. Hogan, Y. Horibe, K. Kim, B. I. Min, and S.-W. Cheong, Phys. Rev. Lett. **108**, 116402 (2012).

[4] S. Pyon, K. Kudo, and M. Nohara, J. Phys. Soc. Jpn. **81**, 053701 (2012).

[5] D. Ootsuki, Y. Wakisaka, S. Pyon, K. Kudo, M. Nohara, M. Arita, H. Anzai, H. Namatame, M. Taniguchi, N. L. Saini, and T. Mizokawa, Phys. Rev. B **86**, 014519 (2012).

[6] M. Kamitani, M. S. Bahramy, R. Arita, S. Seki, T. Arima, Y. Tokura, and S. Ishiwata, Phys. Rev. B **87**, 180501 (2013).

[7] N. Matsumoto, K. Taniguchi, R. Endoh, H. Takano, and S. Nagata, J. Low Temp. Phys. **117**, 1129 (1999).

[8] A. Kiswandhi, J. S. Brooks, H. B. Cao, J. Q. Yan, D. Mandrus, Z. Jiang, and H. D. Zhou, Phys. Rev. B **87**, 121107 (2013).

[9] Y. S. Oh, J. J. Yang, Y. Horibe, and S.-W. Cheong, Phys. Rev. Lett. **110**, 127209 (2013).

[10] A. F. Fang, G. Xu, T. Dong, P. Zheng, and N. L. Wang, Sci. Rep. **3**, 1153 (2013).

[11] H. Cao, B. C. Chakoumakos, X. Chen, J. Yan, M. A. McGuire, H. Yang, R. Custelcean, H. Zhou, D. J. Singh, and D. Mandrus, Phys. Rev. B **88**, 115122 (2013).

[12] L. Zhang, X. Zhu, L. Ling, C. Zhang, L. Pi, and Y. Zhang, Philos. Mag. **94**, 439 (2014).

[13] G. L. Pascut, K. Haule, M. J. Gutmann, S. A. Barnett, A. Bombardi, S. Artyukhin, D. Vanderbilt, J. J. Yang, S.-W. Cheong, and V. Kiryukhin, arXiv:1309.3548.

[14] N. Lazarević, M. Abeykoon, P. W. Stephens, H. Lei, E. S. Bozin, C. Petrovic, and Z. V. Popović, Phys. Rev. B **86**, 054503 (2012).

[15] P. J. Chupas, X. Qiu, J. C. Hanson, P. L. Lee, C. P. Grey, and S. J. L. Billinge, J. Appl. Cryst. **36**, 1342 (2003).

[16] T. Egami and S. J. L. Billinge, *Underneath the Bragg Peaks: Structural Analysis of Complex Materials*, 2nd ed. (Elsevier, Amsterdam, 2012).

[17] H. Kuzmany, *Solid-State Spectroscopy: An Introduction* (Springer, Berlin, 2009).

[18] C. Soulard, P. Petit, P. Deniard, M. Evain, S. Jobic, M.-H. Whangbo, and A.-C. Dhaussy, J. Solid State Chem. **178**, 2008 (2005).

[19] E. Canadell, S. Jobic, R. Brec, J. Rouxel, and M.-H. Whangbo, J. Solid State Chem. **99**, 189 (1992).

[20] T. Hahn, U. Shmueli, A. A. J. C. Wilson, and E. Prince, *International Tables for Crystallography* (Reidel, Dordrecht, 2005).

[21] W. G. Fateley, F. R. Dollish, N. T. McDevitt, and F. F. Bentley, *Infrared and Raman Selection Rules for Molecular and Lattice Vibrations: The Correlation Method* (Wiley-Interscience, New York, 1972).

[22] M. Balkanski, R. F. Wallis, and E. Haro, Phys. Rev. B **28**, 1928 (1983).

[23] N. Lazarević, Z. V. Popović, R. Hu, and C. Petrovic, Phys. Rev. B **81**, 144302 (2010).

[24] N. Lazarević, M. Radonjić, M. Šćepanović, H. Lei, D. Tanasković, C. Petrovic, and Z. V. Popović, Phys. Rev. B **87**, 144305 (2013).

[25] N. Lazarević, Z. V. Popović, R. Hu, and C. Petrovic, Phys. Rev. B **83**, 024302 (2011).

Lattice dynamics of BaFe$_2$X$_3$(X = S, Se) compounds

Z. V. Popović, M. Šćepanović, N. Lazarević, and M. Opačić

Center for Solid State Physics and New Materials, Institute of Physics Belgrade, University of Belgrade,
Pregrevica 118, 11080 Belgrade, Serbia

M. M. Radonjić

Scientific Computing Laboratory, Institute of Physics Belgrade, University of Belgrade, Pregrevica 118, 11080 Belgrade, Serbia,
and Center for Electronic Correlations and Magnetism, Theoretical Physics III, Institute of Physics, University of Augsburg,
D-86135 Augsburg, Germany

D. Tanasković

Scientific Computing Laboratory, Institute of Physics Belgrade, University of Belgrade, Pregrevica 118, 11080 Belgrade, Serbia

Hechang Lei (雷和畅)[*] and C. Petrovic

Condensed Matter Physics and Materials Science Department, Brookhaven National Laboratory, Upton, New York 11973-5000, USA

We present the Raman scattering spectra of the BaFe$_2$X$_3$ (X = S, Se) compounds in a temperature range between 20 and 400 K. Although the crystal structures of these two compounds are both orthorhombic and very similar, they are not isostructural. The unit cell of BaFe$_2$S$_3$(BaFe$_2$Se$_3$) is base-centered *Cmcm* (primitive *Pnma*), giving 18 (36) modes to be observed in the Raman scattering experiment. We have detected almost all Raman active modes, predicted by factor group analysis, which can be observed from the cleavage planes of these compounds. Assignment of the observed Raman modes of BaFe$_2$S(Se)$_3$ is supported by the lattice dynamics calculations. The antiferromagnetic long-range spin ordering in BaFe$_2$Se$_3$ below T_N = 255 K leaves a fingerprint both in the A_{1g} and B_{3g} phonon mode linewidth and energy.

I. INTRODUCTION

Iron-based compounds are one of the top research fields in condensed matter physics [1]. These materials are not only superconducting [2] but also form low-dimensional magnetic structures—spin chains, spin ladders, or spin dimers [3], similar to the cases of cuprates [4] or vanadates [5]. Properties of iron-based selenide superconductors and other low-dimensional magnetic phases of iron-chalcogenides are reviewed in Ref. [6].

BaFe$_2$S$_3$ and BaFe$_2$Se$_3$ belong to the family of the iron-based $S = 2$ two-leg spin-ladder compounds. The crystal structure of these materials can be described as alternate stacking of Fe-S(Se) layers and Ba cations along the crystallographic a axis (b axis). In the Fe-S(Se) plane, only one-dimensional (1D) double chains of edge-shared [FeS(Se)]$_4$ tetrahedra propagate along the a axis (b axis), as shown in Fig. 1. Although the crystal structures of the BaFe$_2$S$_3$ and BaFe$_2$Se$_3$ are isomorphic, they are not isostructural. BaFe$_2$S$_3$ crystalizes in a base-centered orthorhombic structure with *Cmcm* space group [7]. The unit cell of BaFe$_2$Se$_3$ is also orthorhombic but primitive of the *Pnma* space group. The main crystal structure difference of these compounds is an alternation of the Fe-Fe distances in BaFe$_2$Se$_3$ along the chain direction which does not exist in BaFe$_2$S$_3$, where all distances between Fe atoms along the chain direction are the same;

see Figs. 1(b) and 1(c). This difference probably leads to the diverse magnetic properties of these two compounds at low temperatures.

BaFe$_2$S$_3$ is a quasi-one-dimensional semiconductor. The magnetic susceptibility of BaFe$_2$S$_3$, measured at 100 Oe, showed the divergence of the field-cooled susceptibility and zero-field-cooled susceptibility with the cusp at 25 K (freezing temperature) [8], indicating the presence of short-range magnetic correlations and spin-glass-like behavior below 25 K. On the basis of these observations Gönen *et al.* [8] proposed that each [Fe$_2$S$_3$]$^{2-}$ chain possess strong intrachain antiferromagnetic coupling of Fe ions that is mediated through the sulfide ions. The combination of antiferromagnetic coupling, additional crystal field splitting due to neighboring Fe atoms, and direct Fe-Fe interactions presumably give rise to $S = 0$ ground states in this compound [8].

BaFe$_2$Se$_3$ is an insulator down to the lowest measured temperature with a long-range antiferromagnetic (AFM) order with T_N around 255 K and short-range AFM order at higher temperatures [9–12]. It was shown that a dominant order involves 2 × 2 blocks of ferromagnetically aligned four iron spins, whereas these blocks order antiferromagnetically in the same manner as the block AFM $\sqrt{5} \times \sqrt{5}$ state of the iron vacancy ordered A$_2$Fe$_4$Se$_5$ [13–15].

To the best of our knowledge there are no data about the phonon properties of these compounds. In this paper we have measured polarized Raman scattering spectra of BaFe$_2$X$_3$(X = S, Se) in the temperature range between 20 and 400 K. We have observed the Raman active optical phonons, which are assigned using polarized measurements and the lattice dynamical calculations. At temperatures below

---

[*]Present address: Department of Physics, Renmin University of China, 59 Zhongguancun Street, Haidian District, Beijing 100872, China.
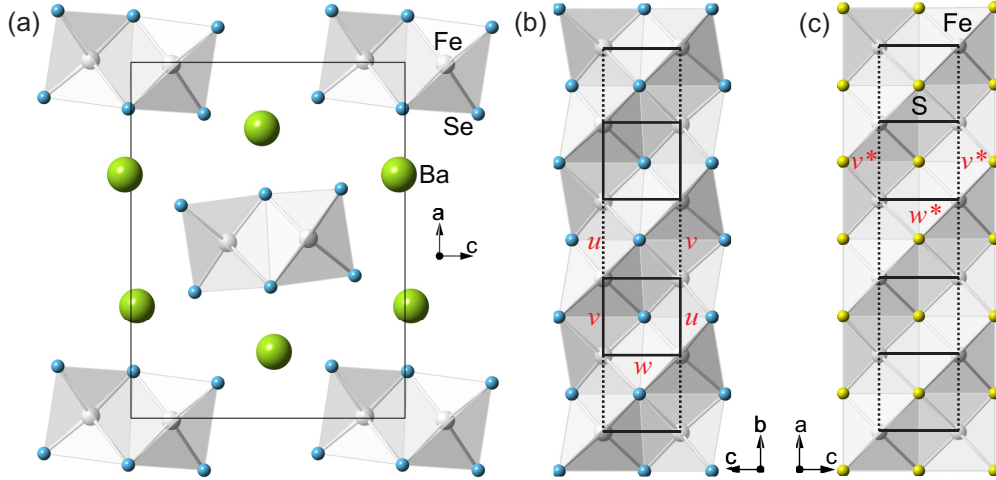
FIG. 1. (Color online) Schematic representation of the $BaFe_2X_3(X = S, Se)$ crystal structure. (a) Projection of the $BaFe_2Se_3$ crystal structure in the (ac) plane. (b) The double chain of Fe-Se tetrahedra connected via common edges along the *b* axis. (c) The Fe-S double chain in the (010) projection. w, u, v represents Fe-Fe distances of ladder rungs ($w = 0.2697$ nm; $w* = 0.2698$ nm) and legs ($u = 0.2688$ nm, $v = 0.2720$ nm; $v* = 0.2643$ nm). Note that in the case of $BaFe_2S_3$ the Fe atoms form an "ideal" ladder (all Fe-Fe distances along the ladder legs are equivalent, which is not the case in $BaFe_2Se_3$).

$T_N = 255$ K in $BaFe_2Se_3$ the Raman modes shows an abrupt change of energy and linewidth due to the antiferromagnetic spin ordering.

II. EXPERIMENT AND NUMERICAL METHOD

Single crystals of $BaFe_2X_3(X = S, Se)$ were grown using self-flux method with nominal composition Ba:Fe:$X = 1$:2:3. Details were described in Ref. [16]. Raman scattering measurements were performed on (110)(sulfide) [(100) (selenide)]-oriented samples in the backscattering micro-Raman configuration. Low-temperature measurements were performed using KONTI CryoVac continuous flow cryostat coupled with JY T64000 and TriVista 557 Raman systems. The 514.5-nm line of an Ar^+/Kr^+ mixed gas laser was used as excitation source. The Raman scattering measurements at higher temperatures were done using a LINKAM THMS600 heating stage.

We calculated phonon energies of the nonmagnetic $BaFe_2S(Se)_3$ single crystals at the center of the Brillouin zone. Calculations were performed within the theory of linear response using the density functional perturbation theory (DFPT) [17] as implemented in the QUANTUM ESPRESSO package [18]. In the first step, we obtained the electronic structure by applying the pseudopotentials based on the projected augmented waves method with the Perdew-Burke-Ernzerhof exchange-correlation functional and nonlinear core correction. Used energy cutoffs for the wave functions and electron densities were 80 (64) Ry and 960 (782) Ry for $BaFe_2S(Se)_3$, respectively. We have carried out the calculation with experimental values of the $BaFe_2S(Se)_3$ unit cell parameters $a = 0.878\,35$ nm, $b = 1.1219$ nm, $c = 0.5286$ nm [7] ($a = 1.188\,34$ nm, $b = 0.541\,41$ nm, $c = 0.914\,09$ nm [11]), and the relaxed fractional coordinates; see Table I. Relaxation was applied to place atoms in their equilibrium positions in respect to used pseudopotentials (all forces acting on every atom were smaller than 10^{-4} Ry/a.u.). The difference between experimental and relaxed coordinates is less than 3% for almost

all atom coordinates, except for the *x* direction of the Ba atoms in $BaFe_2Se_3$, which is 6%. Reduction of the *x* coordinate of Ba atoms by relaxation leads to an increase of the distance between the Ba layers. The Brillouin zone was sampled with $8 \times 8 \times 8$ Monkhorst-Pack **k**-space mesh. Calculated Γ point phonon energies of the $BaFe_2S_3$ and $BaFe_2Se_3$ are listed in Tables II and Table IV, respectively.

The DFPT calculation of the phonon-mode energies is performed assuming the paramagnetic solution and the comparison of energies is performed with the experimental results at room temperature. The paramagnetic density functional theory (DFT) solution is metallic, whereas $BaFe_2Se_3$ is AFM insulator at low temperatures. Therefore, we have performed also the spin-polarized DFT calculations, assuming AFM ordering of 2×2 ferromagnetic iron blocks [10–12]. We find the AFM solution and opening of the gap at the Fermi level in agreement with earlier DFT calculations by Saparov *et al.* [10]. Accordingly, we attempted to calculate the phonon

TABLE I. Experimental and relaxed (in square brackets) fractional coordinates of $BaFe_2S_3$ (Ref. [7]) and $BaFe_2Se_3$ (Ref. [11]) crystal structures.

Atom	Site	x	y	z
$BaFe_2S_3$				
Ba	(4c)	0.50 [0.50]	0.1859 [0.1817]	0.25 [0.25]
Fe	(8e)	0.3464 [0.3553]	0.50 [0.50]	0.00 [0.00]
S1	(4c)	0.50 [0.50]	0.6147 [0.6051]	0.25 [0.25]
S2	(8g)	0.2074 [0.2108]	0.3768 [0.3945]	0.25 [0.25]
$BaFe_2Se_3$				
Ba	(4c)	0.186 [0.175]	0.25 [0.25]	0.518 [0.513]
Fe	(8d)	0.493 [0.490]	0.002 [−0.001]	0.353 [0.358]
Se1	(4c)	0.355 [0.366]	0.25 [0.25]	0.233 [0.230]
Se2	(4c)	0.630 [0.613]	0.25 [0.25]	0.491 [0.485]
Se3	(4c)	0.402 [0.415]	0.25 [0.25]	0.818 [0.809]

TABLE II. Calculated and experimentally observed values of Raman active phonon mode energies (in cm^{-1}) of BaFe$_2$S$_3$ single crystal.

Symmetry	Calculation relax. (unrelax.)	Experiment 300 K	Experiment 100 K	Activity	Symmetry	Calculation relax. (unrelax.)	Experiment 300 K	Experiment 100 K	Activity
A_g^1	42.3 (51.2)		39	(xx,yy,zz)	B_{1g}^1	16.7 (63)			(xy)
A_g^2	154.2 (156)		157	(xx,yy,zz)	B_{1g}^2	55.1 (81.8)	44	48	(xy)
A_g^3	201.9 (167.4)	152	165	(xx,yy,zz)	B_{1g}^3	138.8 (153.1)	127	133	(xy)
A_g^4	366.9 (294.8)	295	301	(xx,yy,zz)	B_{1g}^4	243.5 (221.9)	203	214	(xy)
A_g^5	385.8 (307.1)	365	372	(xx,yy,zz)	B_{1g}^5	337.8 (241.6)		332(?)	(xy)
					B_{1g}^6	400.2 (330)	374	381	(xy)
B_{2g}^1	107.8 (113.7)	107	109	(xz)	B_{3g}^1	55.1 (66.8)			(yz)
B_{2g}^2	224.1 (180.8)	181	193	(xz)	B_{3g}^2	201.1 (171.1)	181	193	(yz)
B_{2g}^3	347.8 (283.6)			(xz)	B_{3g}^3	311.2 (308.7)	297	307	(yz)
					B_{3g}^4	369.3 (351.7)			(yz)

energies in the spin-polarized case. However, having now 48 atoms in the unit cell, this calculation turned out to be computationally too demanding. Furthermore, we do not believe that such a calculations would gives us in this case important new insights since the number of phonon modes becomes $2 \times 72 - 1 = 143$ (one mode is degenerate), and it is not likely that small splitting of the modes could be compared with the experiments. Also, the phonon frequencies are not particularly sensitive on the precise form of the density of states near the Fermi level (or gap opening) if the overall spectral function remains similar. Therefore, we believe that the usage of the nonmagnetic DFT is a reasonable method for identification of vibrational modes and comparison with the experimental data.

III. RESULTS AND DISCUSSION

A. BaFe$_2$S$_3$

The BaFe$_2$S$_3$ crystal symmetry is orthorhombic, space group $Cmcm$ and $Z = 4$ [7]. The site symmetries of atoms in $Cmcm$ space group are C_{2v}^y (Ba, S1), C_2^x(Fe), and C_s^{xy} (S2). Factor group analysis yields

$$\left(C_{2v}^y\right): \Gamma = A_g + B_{1g} + B_{3g} + B_{1u} + B_{2u} + B_{3u},$$

$$\left(C_2^x\right): \Gamma = A_g + 2B_{1g} + 2B_{2g} + B_{3g}$$
$$+ A_u + 2B_{1u} + 2B_{2u} + B_{3u}.$$

$$\left(C_s^{xy}\right): \Gamma = 2A_g + 2B_{1g} + B_{2g} + B_{3g} + A_u$$
$$+ B_{1u} + 2B_{2u} + 2B_{3u}.$$

Summarizing these representations and subtracting the acoustic ($B_{1u} + B_{2u} + B_{3u}$) and silent ($2A_u$) modes, we obtained the following irreducible representations of BaFe$_2$S$_3$ vibrational modes:

$$\Gamma_{\text{BaFe}_2\text{S}_3}^{\text{optical}} = 5A_g(xx,yy,zz) + 6B_{1g}(xy) + 3B_{2g}(xz)$$
$$+ 4B_{3g}(yz) + 4B_{1u}(E \parallel z) + 5B_{2u}(E \parallel y)$$
$$+ 4B_{3u}(E \parallel x).$$

Thus 18 Raman and 13 infrared active modes are expected to be observed in the BaFe$_2$S$_3$ infrared and Raman spectra. Because

our BaFe$_2$S$_3$ single-crystal samples have (110) orientation, we were able to observe all symmetry modes in the Raman scattering experiment.

The polarized Raman spectra of BaFe$_2$S$_3$, measured from the (110) plane at 100 K, are given in Fig. 2. Five A_g symmetry modes at about 39, 157, 165, 301, and 373 cm^{-1} (100 K) are clearly observed for the $x'(zz)\bar{x}'$ polarization configuration ($x' = [110]$, $y' = [1\bar{1}0]$, $z = [001]$). For parallel polarization along the y' axis, the A_g and B_{1g} symmetry modes may be observed. By comparison ($y'y'$) with (zz) polarized spectrum we assigned the modes at 48, 133, 214, 332, and 381 cm^{-1} as the B_{1g} ones. The intensity of the 332 cm^{-1} mode is at a level of noise. Because of that, assignment of this mode as B_{1g}^5 should be taken as tentative.

For the $x'(y'z)\bar{x}'$ polarization configuration both the B_{2g} and the B_{3g} symmetry modes can be observed. Because we cannot distinguish the B_{2g} and B_{3g} by selection rules from the (110) plane, the assignment of these modes was done with help of the lattice dynamics calculation; see Table II. Features between 40 and 100 cm^{-1} come after subtracting of nitrogen
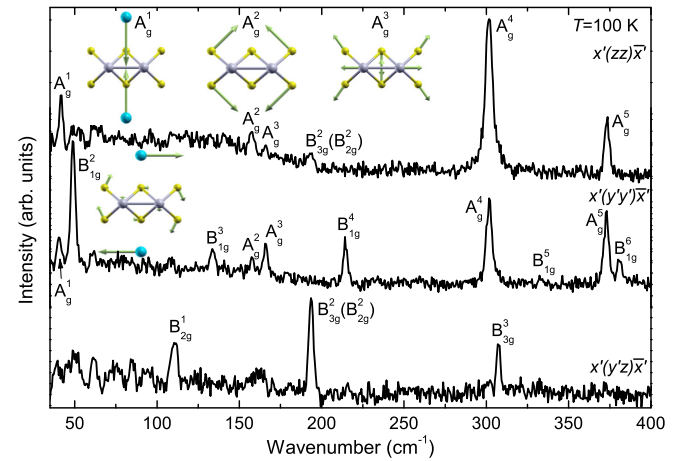

FIG. 2. (Color online) The polarized Raman scattering spectra of BaFe$_2$S$_3$ single crystal measured at 100 K. Insets are the normal modes of the A_g^1, A_g^2, A_g^3, and B_{1g}^2 vibrations. $x' = [110]$, $y' = [1\bar{1}0]$, and $z = [001]$.
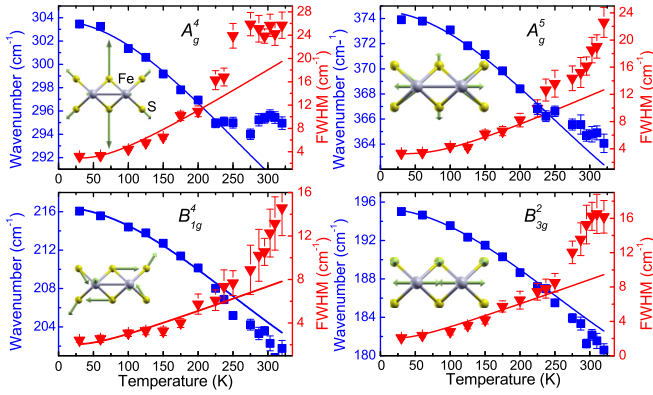
FIG. 3. (Color online) Experimental values (symbols) and calculated temperature dependence (solid lines) of the $BaFe_2S_3$ Raman mode energies and broadenings. Insets represent the normal modes of the A_g^4, A_g^5, B_{1g}^4, and B_{3g}^2 vibrations.

vibration modes. Bump at about 160 cm^{-1} is a leakage of A_g^2 and A_g^3 modes from parallel polarization.

The normal modes of some of A_g, B_{1g}, and B_{3g} vibrations, obtained by the lattice dynamics calculations, are given as insets in Figs. 2 and 3. According to these representations the lowest energy A_g^1 mode (39 cm^{-1}) originates from the Ba atom vibrations along the y axis, and the A_g^2 mode (157 cm^{-1}) represents dominantly S atom vibrations, which tend to elongate $[Fe_2S_3]^{2-}$ chains along the y axis. The A_g^3 mode originates from both the sulfur and the iron atom vibrations, which tend to stretch ladders along the x axis. The A_g^4 mode (Fig. 3) is sulfur atoms breathing vibrations, and the A_g^5 symmetry mode represents the S and Fe atom vibrations with the opposite tendency. The Fe atoms vibrate in opposite directions along the x axis, elongating the ladder, together with S atom vibrations, which tend to compress ladder structure.

Temperature dependence of the A_g^4, A_g^5, B_{1g}^4, and B_{3g}^2 mode energy and linewidth are given in Fig. 3.

In general, temperature dependance of Raman mode energy can be described with [19]

$$\omega(T) = \omega_0 + \Delta(T), \qquad (1)$$

where ω_0 is temperature-independent contribution to the energy of the phonon mode, whereas $\Delta(T)$ can be decomposed in

$$\Delta(T) = \Delta^V + \Delta^A. \qquad (2)$$

The first term in Eq. (2) represents change of phonon energy due to the thermal expansion of the crystal lattice, and is given by [20]

$$\Delta^V = -\omega_0 \gamma \frac{\Delta V(T)}{V_0}, \qquad (3)$$

where γ is the Grüneisen parameter of a given mode.

The second term in Eq. (2) is a contribution to the Raman mode energy from phonon-phonon scattering. By taking into account only three-phonon processes,

$$\Delta^A = -C\left(1 + \frac{4\lambda_{\text{ph-ph}}}{e^{\hbar\omega_0/2k_BT} - 1}\right). \qquad (4)$$

TABLE III. The best fit parameters of $BaFe_2S_3$ and $BaFe_2Se_3$.

Mode symmetry	$\omega_0(\text{cm}^{-1})$	γ	$\Gamma_0(\text{cm}^{-1})$	λ
$BaFe_2S_3$				
A_g^4	303.7(2)	3.7(2)	2.9(2)	2.8(5)
A_g^5	374.6(2)	2.6(2)	3.3(2)	1.9(3)
B_{1g}^4	216.5(2)	4.8(2)	2.0(3)	0.9(3)
B_{3g}^2	195.3(1)	5.2(2)	2.0(3)	1.0(1)
$BaFe_2Se_3$				
A_g^8	200.0(1)	1.6(2)	2.3(1)	0.4(1)
A_g^9	272.6(2)	1.4(1)	2.3(1)	0.6(1)
A_g^{10}	288.1(3)	1.8(2)	5.2(1)	0.3(1)
A_g^{11}	297.1(4)	1.4(2)	5.6(2)	0.4(1)

C and $\lambda_{\text{ph-ph}}$ are the anharmonic constant and phonon-phonon interaction constant, respectively.

Temperature dependence of Raman mode linewidth is caused only by phonon anharmonicity:

$$\Gamma(T) = \Gamma_0\left(1 + \frac{2\lambda_{\text{ph-ph}}}{e^{\hbar\omega_0/2k_BT} - 1}\right), \qquad (5)$$

where Γ_0 is the anharmonic constant.

Parameter C is connected with ω_0 and Γ_0 via relation [19]

$$C = \frac{\Gamma_0^2}{2\omega_0}. \qquad (6)$$

ω_0 and Γ_0 can be determined by extrapolation of the corresponding experimental data to 0 K. With these parameters known, we can fit the phonon mode linewidth, using Eq. (5), to obtain $\lambda_{\text{ph-ph}}$. Then, by determining parameter C via Eq. (6), Raman mode energy can be properly fitted, with γ as the only unknown parameter. Using data from Ref. [12] for the temperature change of the lattice constants of $BaFe_2Se_3$ one can perform the corresponding analysis of the Raman mode energies' temperature dependance.

The best-fit parameters are collected in Table III. Because the Γ_0 is very small in comparison to ω_0, for all modes of both compounds (Table III), according to Eq. (6) the C anharmonic parameter becomes very small. Thus, contribution to the Raman mode energy from the phonon-phonon interaction can be neglected. In fact, a change of Raman mode energy with temperature is properly described only with the thermal expansion term Δ^V, Eq. (3).

The most intriguing finding in Fig. 3 is a dramatic change of slope of the A_g^4 mode linewidth (energy) temperature dependence at about 275 K. Because a hump in the inverse molar magnetic susceptibility [8] and a change of slope of the electrical resistivity [21] temperature dependence are observed in $BaFe_2S_3$ at about the same temperature we concluded that the deviation from anharmonic behavior for A_g^4 mode could be related to spin and charge. In fact, many of iron-based spin-ladder materials have the 3D-antiferromagnetic phase transition at about 260 K. We believe that in the case of $BaFe_2S_3$ the antiferromagnetic ordering of spins within the ladder legs changes from short-range to the long-range state, without 3D antiferromagnetic spin ordering (the Néel state) of the whole crystal. This transition is followed with change
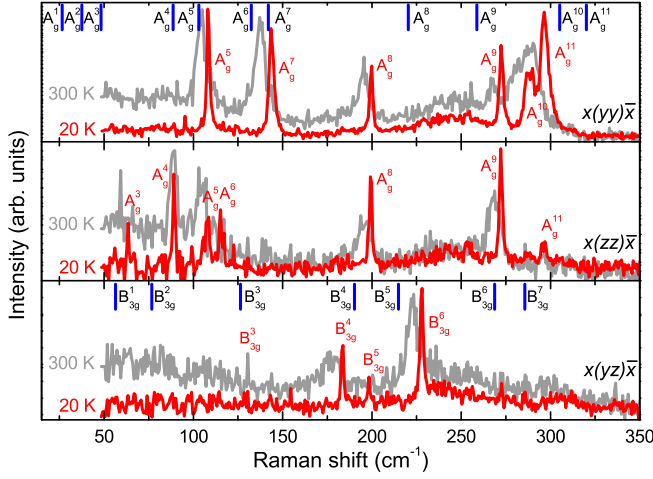
FIG. 4. (Color online) The $x(yy)\bar{x}$, $x(zz)\bar{x}$, and $x(yz)\bar{x}$ polarized Raman scattering spectra of BaFe$_2$Se$_3$ single crystals measured at room temperature and at 20 K. Vertical bars are calculated values of the A_g and the B_{3g} symmetry Raman active vibrations.

of the electronic structure, which could explain the abrupt increase of the resistivity at this temperature [21]. A lack of the BaFe$_2$S$_3$ low-temperature crystallographic and transport properties measurements did not allow a more detailed study of a possible origin of the phonon energy and linewidth deviation from the anharmonic picture at about 275 K.

B. BaFe$_2$Se$_3$

The BaFe$_2$Se$_3$ unit cell consists of four formula units comprising of 24 atoms. The site symmetries of atoms in

Pnma space group are C_s^{xz} (Ba, Se1, Se2, Se3) and C_1 (Fe). Factor group analysis yields

$$(C_s^{xz}): \Gamma = 2A_g + 1B_{1g} + 2B_{2g} + 1B_{3g}$$
$$+ A_u + 2B_{1u} + 1B_{2u} + 2B_{3u},$$
$$(C_1): \Gamma = 3A_g + 3B_{1g} + 3B_{2g} + 3B_{3g}$$
$$+ 3B_{1u} + 3B_{2u} + 3B_{3u}.$$

Summarizing these representations and subtracting the acoustic ($B_{1u} + B_{2u} + B_{3u}$) and silent ($4A_u$) modes, we obtained the following irreducible representations of BaFe$_2$Se$_3$ vibrational modes:

$$\Gamma_{\text{BaFe}_2\text{Se}_3}^{\text{optical}} = 11A_g + 7B_{1g} + 11B_{2g} + 7B_{3g}$$
$$+ 11B_{1u} + 7B_{2u} + 11B_{3u}$$

Thus 36 Raman and 29 infrared active modes are expected to be observed in the BaFe$_2$Se$_3$ vibrational spectra. Because the BaFe$_2$Se$_3$ single crystals have the (100) orientation (the crystallographic a axis is perpendicular to the plane of the single crystal), we were able to access only the A_g and the B_{3g} symmetry modes in the Raman scattering experiment.

The polarized Raman spectra of BaFe$_2$Se$_3$, measured from (100) plane at room temperature and 20 K, for the parallel and crossed polarization configurations, are given in Fig. 4. The spectra measured for parallel polarization configurations consist of the A_g symmetry modes. Six modes at about 108, 143.5, 200, 272, 288.7, and 296.5 cm^{-1} (20 K) are clearly observed for the $x(yy)\bar{x}$ polarization configuration and three additional modes are observed at about 63.4, 89, and 115 cm^{-1} for the $x(zz)\bar{x}$ polarization configuration. For the $x(yz)\bar{x}$ polarization configuration, three Raman active B_{3g} symmetry

TABLE IV. Calculated and experimentally observed values of Raman active phonon mode energies (in cm^{-1}) of BaFe$_2$Se$_3$ single crystal.

Symmetry	Calc.	Experiment 300 K	Experiment 20 K	Activity	Symmetry	Calc.	Experiment 300 K	Experiment 20 K	Activity
A_g^1	26.5			(xx,yy,zz)	B_{2g}^1	25.8			(xz)
A_g^2	37.5			(xx,yy,zz)	B_{2g}^2	48.0			(xz)
A_g^3	48.3	59	63.4	(xx,yy,zz)	B_{2g}^3	68.7			(xz)
A_g^4	88.6	88	89	(xx,yy,zz)	B_{2g}^4	88.8			(xz)
A_g^5	103.0	104.3	108	(xx,yy,zz)	B_{2g}^5	100.4			(xz)
A_g^6	132.4	111	115	(xx,yy,zz)	B_{2g}^6	138.2			(xz)
A_g^7	142.0	137	143	(xx,yy,zz)	B_{2g}^7	144.5			(xz)
A_g^8	220.4	195.6	200	(xx,yy,zz)	B_{2g}^8	212.9			(xz)
A_g^9	258.8	267	272	(xx,yy,zz)	B_{2g}^9	261.7			(xz)
A_g^{10}	305.2	280	288.7	(xx,yy,zz)	B_{2g}^{10}	303.9			(xz)
A_g^{11}	320.2	290	296.5	(xx,yy,zz)	B_{2g}^{11}	321.5			(xz)
B_{1g}^1	56.4			(xy)	B_{3g}^1	56.4			(yz)
B_{1g}^2	72.8			(xy)	B_{3g}^2	76.7			(yz)
B_{1g}^3	126.2			(xy)	B_{3g}^3	126.4			(yz)
B_{1g}^4	191.4			(xy)	B_{3g}^4	190.2	177	183.8	(yz)
B_{1g}^5	210.5			(xy)	B_{3g}^5	214.9		198	(yz)
B_{1g}^6	267.1			(xy)	B_{3g}^6	268.8	222.8	228	(yz)
B_{1g}^7	285.2			(xy)	B_{3g}^7	285.7			(yz)

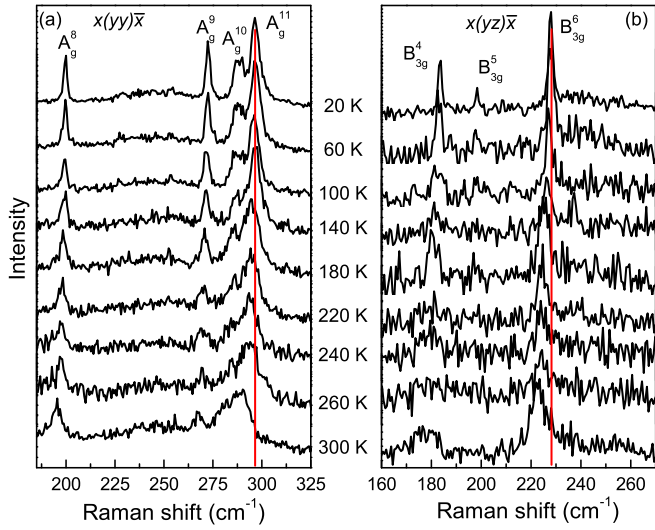FIG. 5. (Color online) The polarized Raman spectra of BaFe₂Se₃ single crystals measured at various temperatures. (a) $x(yy)\bar{x}$ polarization configuration; (b) $x(yz)\bar{x}$ polarization configuration.

FIG. 6. (Color online) Experimental values (symbols) and calculated temperature dependence (solid lines) of BaFe₂Se₃ Raman mode energies. The best-fit parameters, for the temperature range below T_N, are given in Table III. Insets represent normal modes of the A_g^8, A_g^9, A_g^{10}, and A_g^{11} vibrations.

modes at 183.8, 198, and 228 cm⁻¹ (20 K) are observed. Vertical bars in Fig. 4 denote the calculated energies of the A_g and B_{3g} symmetry modes, which are in rather good agreement with experimentally observed ones. The results of the lattice dynamics calculations, together with the experimental data, are summarized in Table IV.

According to the lattice dynamics calculations the lowest energy A_g^1 mode is dominated by Ba atom vibrations along the ⟨101⟩ directions and the A_g^2 mode represents vibrations of Fe and Se atoms which tend to rotate [Fe₂Se₃]²⁻ chains around of the b axis. The A_g^3 mode involves all atom vibrations, which tend to stretch crystal structure along the ⟨101⟩ directions, whereas the A_g^4 mode originates from Se atom vibrations along the c axis and the Fe atom vibrations along the ⟨101⟩ directions. The A_g^5 mode represents vibration of Fe and Se atoms, which leads to [Fe₂Se₃]²⁻ -chain compression along the c axis. The A_g^6 mode originates from Se and Fe atom vibrations which stretch [Fe₂Se₃]²⁻ chains along the c axis. Finally, the A_g^7 mode originates from Fe atom vibrations toward each other along the chain direction together with vibrations of the Se atoms along the c axis. The normal coordinates of the A_g^8, A_g^9, A_g^{10}, and A_g^{11} modes are given as insets in Fig. 6. As can be seen from Fig. 6 the A_g^8 mode originates dominantly from Se atom stretching vibrations, whereas the A_g^9, A_g^{10}, and A_g^{11} modes represent vibrations of both the Se and Fe atoms. In fact, the A_g^9 mode represents mostly Se atom vibrations along the c axis, and the A_g^{10} mode consists of Fe and Se vibrations along the c axis, which tend to elongate ladder structure along the b axis. Finally, the A_g^{11} mode represents the Fe atom vibrations toward each other along the chain axis, together with Se atom vibrations perpendicular to the chain direction.

By lowering the temperature, the lattice parameters of BaFe₂Se₃ decrease continuously without the crystal symmetry change around the magnetic ordering temperature [11,12] $T_N = 255$ K. Consequently we should expect the Raman mode hardening, without any abrupt change. Contrary to
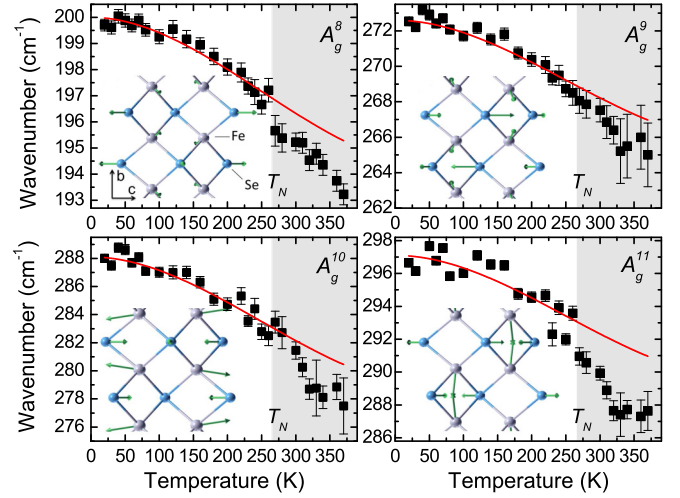
expectations, the A_g and B_{3g} modes (see Figs. 5, 6, and 7) sharply increase their energies below the phase transition temperature T_N, as shown in details in Fig. 6. Because a significant local lattice distortion (Fe atom displacement along
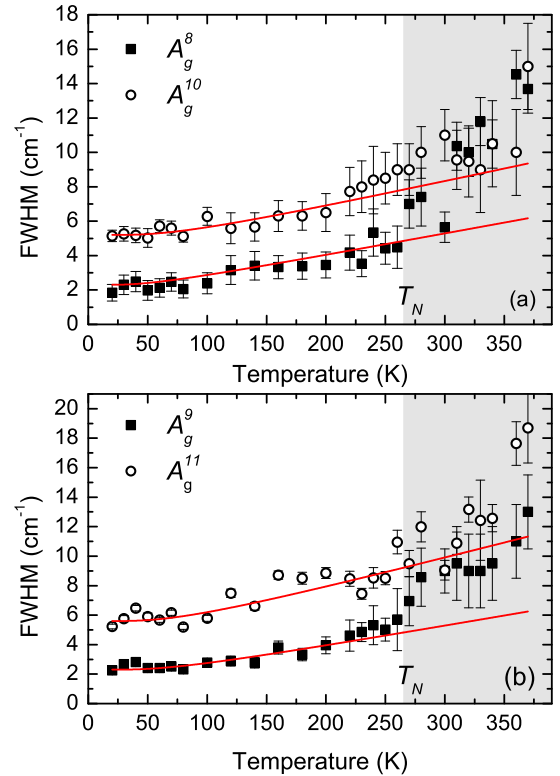

FIG. 7. (Color online) Linewidth vs temperature dependence of (a) A_g^8 and A_g^{10} modes and (b) A_g^9 and A_g^{11} modes of BaFe₂Se₃. Solid lines are calculated using Eq. (5). The best-fit parameters for a temperature range below T_N are given in Table III.

the *b* axis is as large as approximately 0.001 nm) [11,12] exists, driven by the magnetic order, we concluded that spin-phonon (magnetoelastic) coupling is responsible for Raman mode energy and linewith change in the antiferromagnetic phase. In fact, the existence of local displacements in the Fe atoms at T_N have a significant impact on the electronic structure due to rearrangement of electrons near the Fermi level [11] and consequently the change in the phonon energy and broadening. Raman mode linewidth change at about T_N is clearly observed as deviation from the usual anharmonicity temperature dependence (solid lines in Fig. 7) for all modes presented in Fig. 6.

IV. CONCLUSION

We have measured the polarized Raman scattering spectra of the BaFe$_2$S$_3$ and BaFe$_2$Se$_3$ single crystals in a temperature range between 20 and 400 K. Almost all Raman-active modes predicted by factor-group analysis to be observed from the cleavage planes of BaFe$_2$S$_3$ (110) and BaFe$_2$Se$_3$ (100) single crystals are experimentally detected and assigned.

Energies of these modes are in rather good agreement with the lattice dynamics calculations. The BaFe$_2$Se$_3$ Raman modes linewidth and energy change substantially at temperatures below $T_N = 255$ K, where this compound becomes antiferromagneticaly long-range ordered.

[1] C. King and D. A. Pendlebury, Web of knowledge research fronts 2013: 100 top-ranked specialties in the sciences and social sciences, http://sciencewatch.com/sites/sw/files/sw-article/media/research-fronts-2013.pdf

[2] Y. Kamihara, T. Watanabe, M. Hirano, and H. Hosono, J. Am. Chem. Soc. **130**, 3296 (2008).

[3] Z. V. Popović, M. Šćepanović, N. Lazarević, M. M. Radonjić, D. Tanasković, H. Lei, and C. Petrovic, Phys. Rev. B **89**, 014301 (2014).

[4] Z. V. Popović, M. J. Konstantinović, V. A. Ivanov, O. P. Khuong, R. Gajić, A. Vietkin, and V. V. Moshchalkov, Phys. Rev. B **62**, 4963 (2000).

[5] M. J. Konstantinović, Z. V. Popović, M. Isobe, and Y. Ueda, Phys. Rev. B **61**, 15185 (2000).

[6] E. Dagotto, Rev. Mod. Phys. **85**, 849 (2013).

[7] H. Hong and H. Steinfink, J. Solid State Chem. **5**, 93 (1972).

[8] Z. S. Gönen, P. Fournier, V. Smolyaninova, R. Greene, F. M. Araujo-Moreira, and B. Eichhorn, Chem. Mater. **12**, 3331 (2000).

[9] H. Lei, H. Ryu, A. I. Frenkel, and C. Petrovic, Phys. Rev. B **84**, 214511 (2011).

[10] B. Saparov, S. Calder, B. Sipos, H. Cao, S. Chi, D. J. Singh, A. D. Christianson, M. D. Lumsden, and A. S. Sefat, Phys. Rev. B **84**, 245132 (2011).

[11] J. M. Caron, J. R. Neilson, D. C. Miller, A. Llobet, and T. M. McQueen, Phys. Rev. B **84**, 180409 (2011).

[12] Y. Nambu, K. Ohgushi, S. Suzuki, F. Du, M. Avdeev, Y. Uwatoko, K. Munakata, H. Fukazawa, S. Chi, Y. Ueda, and T. J. Sato, Phys. Rev. B **85**, 064413 (2012).

[13] F. Ye, S. Chi, W. Bao, X. F. Wang, J. J. Ying, X. H. Chen, H. D. Wang, C. H. Dong, and M. Fang, Phys. Rev. Lett. **107**, 137003 (2011).

[14] N. Lazarević, M. Abeykoon, P. W. Stephens, H. Lei, E. S. Bozin, C. Petrovic, and Z. V. Popović, Phys. Rev. B **86**, 054503 (2012).

[15] N. Lazarević, H. Lei, C. Petrovic, and Z. V. Popović, Phys. Rev. B **84**, 214305 (2011).

[16] H. Lei, H. Ryu, V. Ivanovski, J. B. Warren, A. I. Frenkel, B. Cekic, W.-G. Yin, and C. Petrovic, Phys. Rev. B **86**, 195133 (2012).

[17] S. Baroni, S. de Gironcoli, A. Dal Corso, and P. Giannozzi, Rev. Mod. Phys. **73**, 515 (2001).

[18] P. Giannozzi, S. Baroni, N. Bonini, M. Calandra, R. Car, C. Cavazzoni, D. Ceresoli, G. L. Chiarotti, M. Cococcioni, I. Dabo, A. D. Corso, S. de Gironcoli, S. Fabris, G. Fratesi, R. Gebauer, U. Gerstmann, C. Gougoussis, A. Kokalj, M. Lazzeri, L. Martin-Samos, N. Marzari, F. Mauri, R. Mazzarello, S. Paolini, A. Pasquarello, L. Paulatto, C. Sbraccia, S. Scandolo, G. Sclauzero, A. P. Seitsonen, A. Smogunov, P. Umari, and R. M. Wentzcovitch, J. Phys.: Condens. Matter **21**, 395502 (2009).

[19] H.-M. Eiter, P. Jaschke, R. Hackl, A. Bauer, M. Gangl, and C. Pfleiderer, Phys. Rev. B **90**, 024411 (2014).

[20] V. Gnezdilov, Y. Pashkevich, P. Lemmens, A. Gusev, K. Lamonova, T. Shevtsova, I. Vitebskiy, O. Afanasiev, S. Gnatchenko, V. Tsurkan, J. Deisenhofer, and A. Loidl, Phys. Rev. B **83**, 245127 (2011).

[21] W. Reiff, I. Grey, A. Fan, Z. Eliezer, and H. Steinfink, J. Solid State Chem. **13**, 32 (1975).

Evidence of superconductivity-induced phonon spectra renormalization in alkali-doped iron selenides

M Opačić[1], **N Lazarević**[1], **M Šćepanović**[1], **Hyejin Ryu**[2,3,4], **Hechang Lei**[2,5], **C Petrovic**[2,3] **and Z V Popović**[1]

[1] Center for Solid State Physics and New Materials, Institute of Physics Belgrade, University of Belgrade, Pregrevica 118, 11080 Belgrade, Serbia
[2] Condensed Matter Physics and Materials Science Department, Brookhaven National Laboratory, Upton, NY 11973-5000, USA
[3] Department of Physics and Astronomy, Stony Brook University, Stony Brook, NY 11794-3800, USA

E-mail: nenadl@ipb.ac.rs

CrossMark

Abstract

Polarized Raman scattering spectra of superconducting $K_xFe_{2-y}Se_2$ and non-superconducting $K_{0.8}Fe_{1.8}Co_{0.2}Se_2$ single crystals were measured in the temperature range from 10 K up to 300 K. Two Raman active modes from the I4/mmm phase and seven from the I4/m phase are observed in the frequency range from 150 to 325 cm^{-1} in both compounds, suggesting that the $K_{0.8}Fe_{1.8}Co_{0.2}Se_2$ single crystal also has a two-phase nature. The temperature dependence of the Raman mode energy is analyzed in terms of lattice thermal expansion and phonon–phonon interaction. The temperature dependence of the Raman mode linewidth is dominated by temperature-induced anharmonic effects. It is shown that the change in Raman mode energy with temperature is dominantly driven by thermal expansion of the crystal lattice. An abrupt change of the A_{1g} mode energy near T_C was observed in $K_xFe_{2-y}Se_2$, whereas it is absent in non-superconducting $K_{0.8}Fe_{1.8}Co_{0.2}Se_2$. Phonon energy hardening at low temperatures in the superconducting sample is a consequence of superconductivity-induced redistribution of the electronic states below the critical temperature.

Keywords: iron selenides, Raman scattering, superconductivity

(Some figures may appear in colour only in the online journal)

1. Introduction

Since the discovery of superconductivity in the FeSe layered compound $K_xFe_{2-y}Se_2$ [1], considerable attention has been focused on iron selenide materials due to their relatively high superconducting transition temperatures (T_C) [2–5]. Recent investigations of single-layer FeSe films grown on SrTiO$_3$ revealed superconductivity with T_C above 100 K, which is the highest critical temperature among all iron-based materials discovered

so far [6]. Alkali metal-doped iron chalcogenides have some interesting features that distinguish them from other iron-based superconductors [7, 8]. Angle-resolved photoemission measurements showed that there are no hole pockets at the Fermi level in $K_xFe_{2-y}Se_2$, which opens the possibility for a different type of pairing mechanism than in the iron pnictides [9]. This is consistent with observed negative values of the Hall constant R_H in the temperature range 0–150 K [10], which implies that conduction is predominantly governed by electron-like carriers.

The most striking feature of $K_xFe_{2-y}Se_2$ single crystals is the presence of two distinct phases: insulating and metallic/superconducting [8, 11, 12]. The insulating phase has antiferromagnetically, $\sqrt{5} \times \sqrt{5}$, ordered Fe vacancies with large iron magnetic moments, whereas the superconducting

[4] Present address: Advanced Light Source, EO Berkeley National Laboratory, Berkely, California 94729, USA
[5] Present address: Department of Physics, Renmin University, Beijing 100872, China

phase is free of vacancies [11]. Resistivity measurements on a sample with nominal composition $K_{0.8}Fe_2Se_2$ revealed that superconductivity occurs below $T_C \sim 30$ K [1]. However, it was later established that superconductivity appears only in Fe-deficient samples. A broad hump in the in-plane resistivity $\rho_{ab}(T)$, whose position varies between 105 K and 240 K (depending on the sample preparation), presumably occurs due to the type of connection between the two phases [10, 13]. Below the hump, $K_xFe_{2-y}Se_2$ is metallic due to an intrinsic property of the metallic/superconducting state, since insulating regions do not contribute to the spectral weight close to the Fermi energy, as observed by angle-resolved photoemission spectroscopy [14, 15]. It was also shown that M-doping on the Fe site (M = Cr, Co, Ni, Zn) strongly suppresses superconductivity [16, 17]. However, the correlation between antiferromagnetically ordered iron vacancies and superconductivity remains unclear.

Raman scattering studies of $K_xFe_{2-y}Se_2$ single crystals have been performed by several groups [18–20]. Zhang *et al* [18] considered phonon properties of this compound in terms of the I4/m space group. They observed and assigned 11 out of 18 Raman active modes. Their analysis revealed that a phonon of unknown origin, at about $180\,cm^{-1}$ (which was assigned as the A_g symmetry mode) exhibits abrupt hardening of $\sim 1\,cm^{-1}$ at the superconducting critical temperature T_C. Lazarević *et al* [19] analyzed lattice dynamics of $K_xFe_{2-y}Se_2$ in terms of I4/m and I4/mmm phases. They observed and assigned two (of two possible) modes from the high-symmetry phase and 16 out of 18 phonon modes from the low-symmetry phase. They also observed a Raman mode at about $180\,cm^{-1}$ and assigned it as of A_{1g} symmetry originating from the superconducting I4/mmm phase. In [20], the authors argued that new Raman modes, at about 165, 201 and $211\,cm^{-1}$, appear on cooling the sample below 250 K. Based on this, it is concluded that a $K_xFe_{2-y}Se_2$ single crystal exhibits a structural phase transition from I4/m to I4 space group. They assumed a Fano-like shape for some phonons and analyzed the temperature dependence of the Raman mode energy and linewidth in terms of lattice anharmonicity. To the best of our knowledge, the Raman spectrum of $K_xFe_{2-y}Se_2$ single crystals doped with Co is unknown.

In order to determine the impact of superconductivity on the phonon properties of alkali-doped iron selenides, we have performed a Raman scattering study of superconducting $K_xFe_{2-y}Se_2$ and non-superconducting $K_{0.8}Fe_{1.8}Co_{0.2}Se_2$ single crystals. Raman spectra were measured in the temperature range from 10 to 300 K. All phonons expected to appear in the investigated energy range, according to [19], are observed in both single crystals. A detailed analysis of the temperature dependence of energy and linewidth for seven observed Raman active modes is performed.

2. Experiment

$K_xFe_{2-y}Se_2$ and $K_{0.8}Fe_{1.8}Co_{0.2}Se_2$ single crystals were grown and characterized as described in detail elsewhere [21]. Raman scattering measurements were performed on (0 0 1)-oriented samples, using a TriVista 557 Raman system, in backscattering micro-Raman configuration. The 514.5 nm line of an Ar^+/Kr^+ mixed
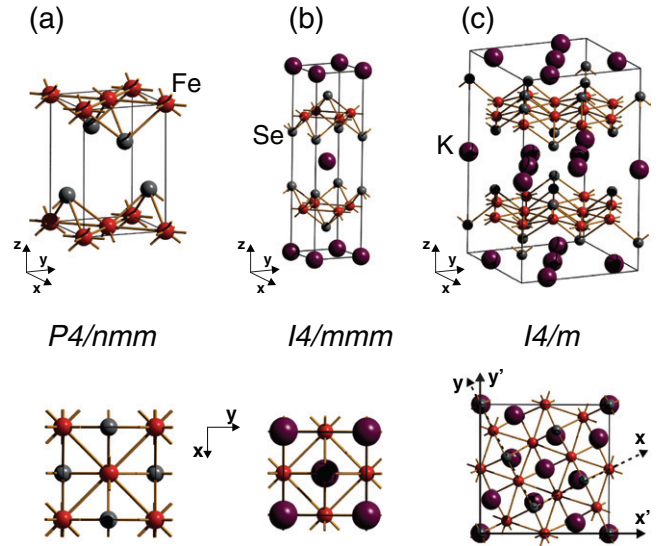

Figure 1. Unit cell for (a) FeSe, (b) and (c) $K_xFe_{2-y}Se_2$ single crystals. In the lower right part I4/m and I4/mmm unit cells are shown together (**x, y** denote the crystallographic axes of the I4/mmm phase, whereas **x′, y′** are crystallographic axes of the I4/m phase domain).

gas laser was used as an excitation source. The Raman scattering measurements were carried out at low laser power, in order to minimize local heating of the sample. All measurements were performed in vacuum, using a KONTI CryoVac continuous flow cryostat with 0.5 mm thick window. The samples were cleaved just before their placement in the cryostat in order to obtain a flat shiny surface. For the data extraction from the Raman spectra, a Voigt profile has been used, where a Gaussian width of $2\,cm^{-1}$ represents the spectral resolution of the instrument.

The FeSe layer is the basic building block for all iron selenide superconductors. An FeSe single crystal (see figure 1(a)) crystallizes in the tetragonal crystal lattice (P4/nmm space group), with two formula units per unit cell [22]. The site symmetries of individual atoms in this space group are D_{2d} (Fe) and C_{4v} (Se). Factor group analysis gives the normal mode distribution in the Brillouin zone center:

$$(D_{2d}) : \Gamma = A_{2u} + B_{1g} + E_g + E_u,$$
$$(C_{4v}) : \Gamma = A_{1g} + A_{2u} + E_g + E_u.$$

In total, $A_{1g}(\alpha_{xx+yy}, \alpha_{zz})$, $B_{1g}(\alpha_{xx-yy})$ and $2E_g(\alpha_{xz}, \alpha_{yz})$ phonons are Raman active. A_{1g} (B_{1g}) modes represent vibrations of Se (Fe) ions along the z-axis, whereas E_g modes originate from vibrations of Fe and Se ions within the *ab* plane [23].

A $K_xFe_{2-y}Se_2$ single crystal consists of K ions intercalated between the FeSe slabs, which dominantly determines its physical properties [1]. At high temperature it crystallizes in the I4/mmm space group. On cooling below 532 K partial symmetry breaking occurs, as a consequence of Fe vacancy ordering [8]. Recent studies revealed that, at low temperatures, $K_xFe_{2-y}Se_2$ single crystals consist of two phases separated at the nanometer scale: a superconducting phase (I4/mmm) and an insulating phase (I4/m) [11, 12, 19]. By comparing the crystallographic data for FeSe [22] and $K_xFe_{2-y}Se_2$ [1], it can be seen that the intralayer Fe–Fe distances and Fe–Se bond lengths increase in $K_xFe_{2-y}Se_2$ by only a few per cent.

Site symmetries of atoms in the I4/mmm group (see figure 1(b)) are D_{4h} (K), C_{4v} (Se) and D_{2d} (Fe). By applying symmetry analysis, it follows that

$$(D_{4h}) : \Gamma = A_{2u} + E_u,$$
$$(D_{2d}) : \Gamma = A_{2u} + B_{1g} + E_g + E_u,$$
$$(C_{4v}) : \Gamma = A_{1g} + A_{2u} + E_g + E_u,$$

giving the same distribution of Raman active modes in the Brillouin zone center as in the case of FeSe. When measuring in the (0 0 1) plane of the sample, only A_{1g} and B_{1g} modes are observable in the Raman scattering experiment [24]. In [19], these modes have been observed at about 180 and 207 cm^{-1} (at 85 K), respectively. Gnezdilov *et al* [23] recently showed that A_{1g} and B_{1g} phonons in a FeSe single crystal, originating from the same vibrations as in the case of $K_xFe_{2-y}Se_2$, appear in the Raman scattering spectra at similar frequencies (~182 and ~205 cm^{-1}, respectively, at 80 K). Together with *ab initio* phonon calculations for the I4/mmm space group with magnetic ordering included [25], this confirms the assignation given in [19].

The I4/m crystal structure is shown in figure 1(c). The lower part of figure 1(c) illustrates I4/m and I4/mmm unit cells projected on the (0 0 1) plane of the sample. It should be noted that the crystallographic axes of the I4/m phase ($\mathbf{x}'$, $\mathbf{y}'$) are rotated by an angle $\alpha \approx 26.6°$ with respect to the axes ($\mathbf{x}$, $\mathbf{y}$) of the I4/mmm phase, due to $\sqrt{5} \times \sqrt{5}$ vacancy order. Site symmetries of atoms in I4/m space group are C_{4h} and C_S (K), S_4 and C_1 (Fe), C_4 and C_1 (Se). Factor group analysis yields

$$(C_{4h}) : \Gamma = A_u + E_u,$$
$$(C_S) : \Gamma = 2A_g + A_u + 2B_g + B_u + E_g + 2E_u,$$
$$(S_4) : \Gamma = A_u + B_g + E_g + E_u,$$
$$(C_4) : \Gamma = A_g + A_u + E_g + E_u,$$
$$(C_1) : \Gamma = 3A_g + 3A_u + 3B_g + 3B_u + 3E_g + 3E_u.$$

One can expect 27 Raman active phonons originating from the I4/m phase: $9A_g(\alpha_{x'x'+y'y'}, \alpha_{z'z'})$, $9B_g(\alpha_{x'x'-y'y'}, \alpha_{x'y'})$ and $9E_g(\alpha_{x'z}, \alpha_{y'z})$ modes. Due to the (0 0 1) orientation of our samples, only A_g and B_g modes can be observed in the Raman spectra [26]. According to the analysis of Raman mode intensities, A_g phonons vanish in the crossed polarization configuration, whereas B_g modes are observable in both crossed and parallel polarization configurations [19].

3. Results and discussion

Figure 2(a) shows polarized Raman scattering spectra of $K_xFe_{2-y}Se_2$ single crystals, in the spectral range between 150 and 325 cm^{-1}, measured from the (0 0 1) plane of the sample at various temperatures. The observed Raman modes are assigned according to [19] (see figure 2(a)) and in agreement with previously discussed selection rules for the high-symmetry (I4/mmm) and low-symmetry (I4/m) phases of this phase-separated sample [11]. The Raman active mode appearing in crossed polarization configuration at about 206 cm^{-1} (marked by an arrow in figure 3) could be assigned as the B_{1g} symmetry mode [19]. However, a high-intensity A_g^6 mode
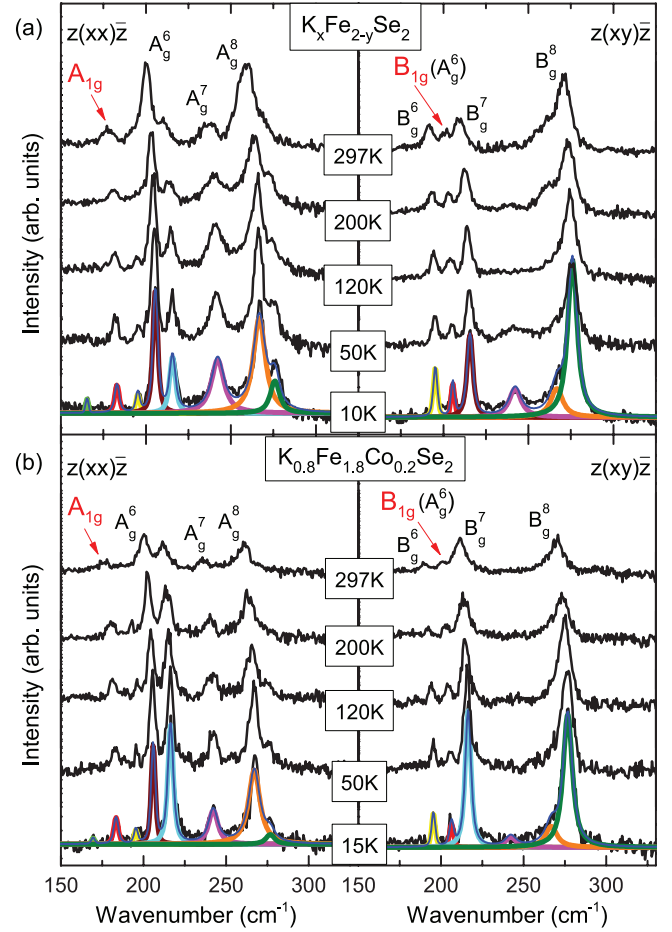

Figure 2. Temperature-dependent Raman spectra of (a) $K_xFe_{2-y}Se_2$ and (b) $K_{0.8}Fe_{1.8}Co_{0.2}Se_2$ single crystals in parallel (left panel) and crossed (right panel) polarization configuration ($\mathbf{x} = [1\,0\,0]$, $\mathbf{y} = [0\,1\,0]$). Phonon modes originating from the high-symmetry I4/mmm phase are marked by arrows.

phonon is present in the parallel polarization configuration at almost the same frequency (see figure 3). Due to the possible leakage of the A_g^6 mode, unambiguous assignment of the marked Raman mode cannot be made here.

Polarized Raman scattering spectra of $K_{0.8}Fe_{1.8}Co_{0.2}Se_2$ single crystals, measured from the (0 0 1) plane of the sample at various temperatures, are presented in figure 2(b). Energies of Raman active phonons are close to the energies of the corresponding modes in $K_xFe_{2-y}Se_2$. Based on this, it can be concluded that doping of a $K_xFe_{2-y}Se_2$ single crystal with a small amount of Co does not have a significant impact on the phonon spectrum in the normal state.

Ignatov *et al* [20] argued that the Raman active mode at about 203 cm^{-1} in $K_xFe_{2-y}Se_2$ (at 3 K) disappears above 250 K, together with two other modes at about 163 and 210 cm^{-1}. They concluded that these modes belong to the I4 space group. As can be seen in figure 2, this phonon (206 cm^{-1}) is clearly visible in our Raman spectra of both compounds up to room temperature, and it is assigned in [19] as the B_{1g} mode, originating from the I4/mmm phase. Due to the absence of new Raman modes below 250 K, there are no indications of a structural phase transition in our samples.
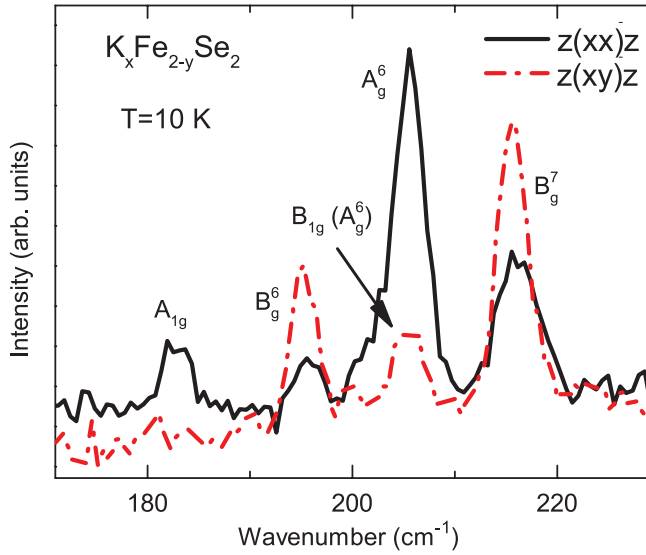
Figure 3. Raman scattering spectra of $K_xFe_{2-y}Se_2$ single crystals measured at 10 K in parallel ($\mathbf{z(xx)\bar{z}}$) and crossed ($\mathbf{z(xy)\bar{z}}$) polarization configurations, in the frequency range from 170 to 230 cm^{-1}. The presence of the A_g^6 mode at about 206 cm^{-1} prevents unambiguous assignation of the low-intensity Raman mode appearing at almost the same frequency in the crossed polarization configuration.
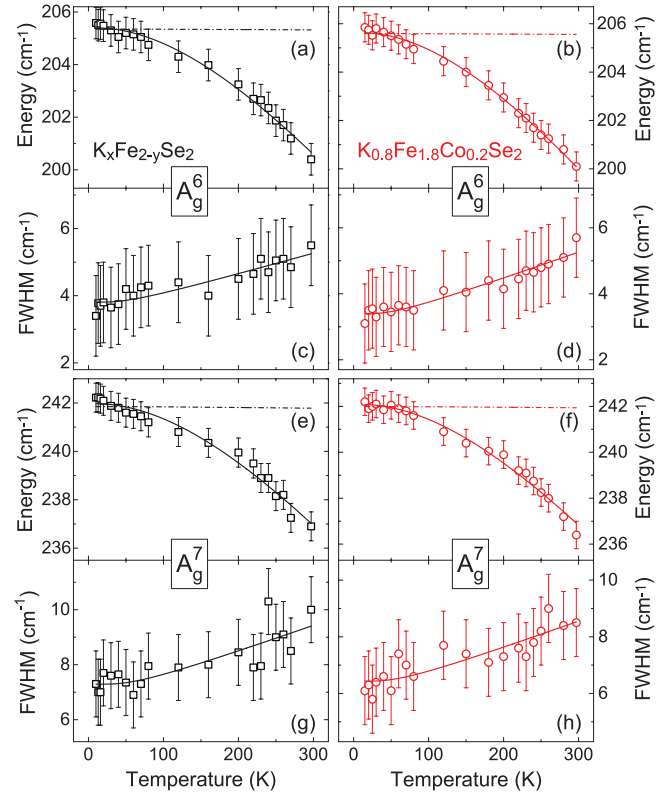

Figure 4. Energy and linewidth of (a)–(d) A_g^6 and (e)–(h) A_g^7 Raman modes of $K_xFe_{2-y}Se_2$ (left panels) and $K_{0.8}Fe_{1.8}Co_{0.2}Se_2$ (right panels) single crystals as functions of temperature. Solid lines represent theoretical dependences, according to (2) and (6), with Δ^A neglected. The dependence of the A_g^6 and A_g^7 mode energies on temperature with only anharmonic contributions included is shown by dash–dot lines.

The behavior of the phonon modes with temperature can be properly described in terms of the phonon self-energy [27]:

$$\Sigma_i(T) = \Delta_i(T) + i\Gamma_i(T), \qquad (1)$$

where $\Delta_i(T)$ represents the change in the Raman mode energy and $\Gamma_i(T)$ is the mode linewidth, which is inversely proportional to the phonon lifetime τ.

Therefore, the temperature dependence of the Raman mode energy can be described using

$$\omega_i(T) = \omega_{0,i} + \Delta_i(T), \qquad (2)$$

where $\omega_{0,i}$ is the temperature-independent contribution to the energy of the phonon mode i and $\Delta_i(T)$ can be decomposed as [27, 28]

$$\Delta_i(T) = \Delta_i^V + \Delta_i^A. \qquad (3)$$

The first term in (3) represents the change in phonon energy due to the thermal expansion of the crystal lattice, and is given by [27]

$$\Delta_i^V = \omega_{0,i}\left(e^{-3\gamma_i\int_0^T \alpha(T')\,dT'} - 1\right), \qquad (4)$$

where γ_i is the Grüneisen parameter of a given mode and $\alpha(T)$ is the thermal expansion coefficient of the material under investigation.

The second term in (3) describes the contribution of phonon–phonon scattering (lattice anharmonicity) to the Raman mode energy. If we describe anharmonic effects by three-phonon processes, it follows [28] that

$$\Delta_i^A = -C_i\left(1 + \frac{4\lambda_{\mathrm{ph-ph},i}}{e^{\hbar\omega_0/2k_BT} - 1}\right). \qquad (5)$$

C and $\lambda_{\mathrm{ph-ph}}$ are the anharmonic constant and phonon–phonon interaction constant, respectively.

The temperature dependence of the Raman mode linewidth is caused only by phonon anharmonicity [28]:

$$\Gamma_i(T) = \Gamma_{0,i}\left(1 + \frac{2\lambda_{\mathrm{ph-ph},i}}{e^{\hbar\omega_0/2k_BT} - 1}\right), \qquad (6)$$

where Γ_0 is the anharmonic constant.

The parameter C is connected with ω_0 and Γ_0 via the relation [28]

$$C_i = \frac{\Gamma_{0,i}^2}{2\omega_{0,i}}. \qquad (7)$$

ω_0 and Γ_0 can be determined by the extrapolation of the corresponding experimental data to 0 K. With these parameters known, we can fit the phonon mode linewidth, using (6), to obtain $\lambda_{\mathrm{ph-ph}}$. Then, by determining parameter C via (7), the Raman mode energy can be properly fitted, with γ as the only free parameter.

To the best of our knowledge, the thermal expansion coefficient $\alpha(T)$ of $K_xFe_{2-y}Se_2$ is unknown. Because of that, we used experimental data for FeSe, given in figure 2 of [29].

The temperature dependences of the energy and linewidth of the A_g^6 and A_g^7 modes of $K_xFe_{2-y}Se_2$ and $K_{0.8}Fe_{1.8}Co_{0.2}Se_2$

Table 1. Best fit parameters for the temperature dependence of energy and linewidth for the observed Raman modes (ω_0—temperature-independent phonon energy, γ—Grüneisen parameter, Γ_0, C—anharmonic constants, λ_{ph-ph}—phonon–phonon interaction constant).

	A_{1g}	A_g^6	A_g^7	B_g^6	$B_{1g}(A_g^6)$	B_g^7	B_g^8
$K_xFe_{2-y}Se_2$							
ω_0 (cm^{-1})	182.2(2)	205.43(6)	242.06(9)	195.15(5)	205.34(9)	215.62(7)	275.79(6)
γ	1.6(1)	1.74(5)	1.52(6)	1.57(4)	1.63(8)	2.10(5)	1.42(4)
Γ_0 (cm^{-1})		2.8(1)	7.2(2)	1.9(1)		3.2(1)	6.31(6)
λ_{ph-ph}		0.29(3)	0.13(2)	0.42(5)		0.36(3)	0.25(2)
C (cm^{-1})		0.018(2)	0.106(4)	0.009(1)		0.023(2)	0.072(2)
$K_{0.8}Fe_{1.8}Co_{0.2}Se_2$							
ω_0 (cm^{-1})	183.14(6)	205.63(5)	242.16(7)	195.55(5)	206.06(7)	216.08(7)	276.56(6)
γ	2.57(6)	2.05(4)	1.61(5)	1.94(3)	2.07(6)	1.81(5)	1.78(3)
Γ_0 (cm^{-1})		2.31(7)	6.3(2)	1.40(9)		3.1(1)	6.6(1)
λ_{ph-ph}		0.28(3)	0.15(3)	0.61(7)		0.44(4)	0.17(2)
C (cm^{-1})		0.0130(9)	0.083(4)	0.0052(7)		0.023(2)	0.080(3)

Note: The temperature dependence of the linewidth has not been analyzed for the A_{1g} and B_{1g} modes due to large relative errors.

single crystals are presented in figure 4. Using (2), (4), (6) and (7), and following the previously described procedure, we have obtained best fit parameters, which are shown in table 1. It can be seen that the parameter C has very small values for both modes, thus the contribution to the Raman mode energy from the phonon–phonon interaction (as can be seen in figures 4(a), (b), (e) and (f)) can be neglected. For this reason, the change in the Raman mode energy with temperature is properly described only by the thermal expansion term Δ^V (solid lines in figures 4(a), (b), (e) and (f)).

Figure 5 shows the energy and linewidth of the B_g^6, B_g^7 and B_g^8 phonon modes of $K_xFe_{2-y}Se_2$ and $K_{0.8}Fe_{1.8}Co_{0.2}Se_2$ single crystals as functions of temperature. Analysis of the temperature dependence of energy and linewidth for these modes was carried out as in the case of the A_g phonons. Best fit parameters are listed in table 1. Small values of the parameter C allow us to omit the contribution from the lattice anharmonicity to the phonon mode energy. Good agreement of the theoretical curves with experimental data justifies our assumption. The Grüneisen parameter is close to the conventional value $\gamma \sim 2$ for B_g modes, as well as for the other analyzed Raman active phonons.

The dependence of the A_{1g} and $B_{1g}(A_g^6)$ mode energy of $K_xFe_{2-y}Se_2$ and $K_{0.8}Fe_{1.8}Co_{0.2}Se_2$ single crystals on temperature is given in figure 6. Rather small values of intrinsic linewidth for both modes ($\Gamma_0 \sim 2$ cm^{-1}) give negligible values of parameter C. Therefore, the temperature dependence of A_{1g} and $B_{1g}(A_g^6)$ phonon energy is analyzed using (2) with only the Δ^V term included. The $B_{1g}(A_g^6)$ mode energy of both single crystals exhibits a good agreement between experimental data and expected behavior (represented by solid lines in figure 6) over the whole temperature range. However, the temperature dependence of the A_{1g} mode energy is well described by the proposed model only in the case of the Co-doped (non-superconducting) sample. An abrupt change in the A_{1g} mode energy around T_C in the

superconducting sample (see inset of figure 6) has been observed. This results in a clear deviation from the expected behavior described with (2) and is governed by some other interaction.

It is well established that, upon entering the superconducting state, some of the phonons are renormalized due to the change in electronic structure with the opening of the superconducting gap, and therefore electron–phonon coupling. Depending on the values of the corresponding phonon energies and the magnitude of the superconducting gap, this may result in hardening or softening of the phonons [30]. Recently, the superconductivity-induced self-energy effect has also been reported in some iron arsenides [31–33]. We believe that the A_{1g} mode hardening around T_C, observed for the superconducting sample and absent for the non-superconducting one (see inset of figure 6), is caused by superconductivity-induced phonon renormalizaton. Moreover, the hardening around T_C has been observed only for the mode corresponding to the vibrations of the superconducting high-symmetry (I4/mmm) phase in the superconducting $K_xFe_{2-y}Se_2$ sample, and it is in agreement with the expected behavior ($2\Delta_c < \omega_{A_{1g}}$, $2\Delta_c \sim 130$ cm^{-1}) [9, 11, 30].

From the observed renormalization of the A_{1g} mode energy at T_C, the strength of electron–phonon coupling in a $K_xFe_{2-y}Se_2$ single crystal can be estimated at the Γ-point. By using the formula $\lambda = -\kappa \mathrm{Re}\left(\frac{\sin u}{u}\right)$ [33, 34], where $\kappa = \frac{\omega^{SC}}{\omega^N} - 1 \approx 0.55\%$ is the superconductivity-induced renormalization constant (ω^{SC} and ω^N are phonon energies in the superconducting and normal states, respectively), and $u = \pi + 2i \cosh^{-1}\left(\frac{\omega^N}{2\Delta}\right)$, we obtained $\lambda_{A_{1g}}^{\Gamma} \approx 0.002$, indicating weak electron–phonon interaction.

As can be seen from figures 4–6, the connection between electronic transport channels in $K_xFe_{2-y}Se_2$, which manifests as a broad hump in the in-plane resistivity $\rho_{ab}(T)$ [1, 10, 13], does not have a significant impact on the temperature dependences of the energy and linewidth for all investigated Raman active modes.
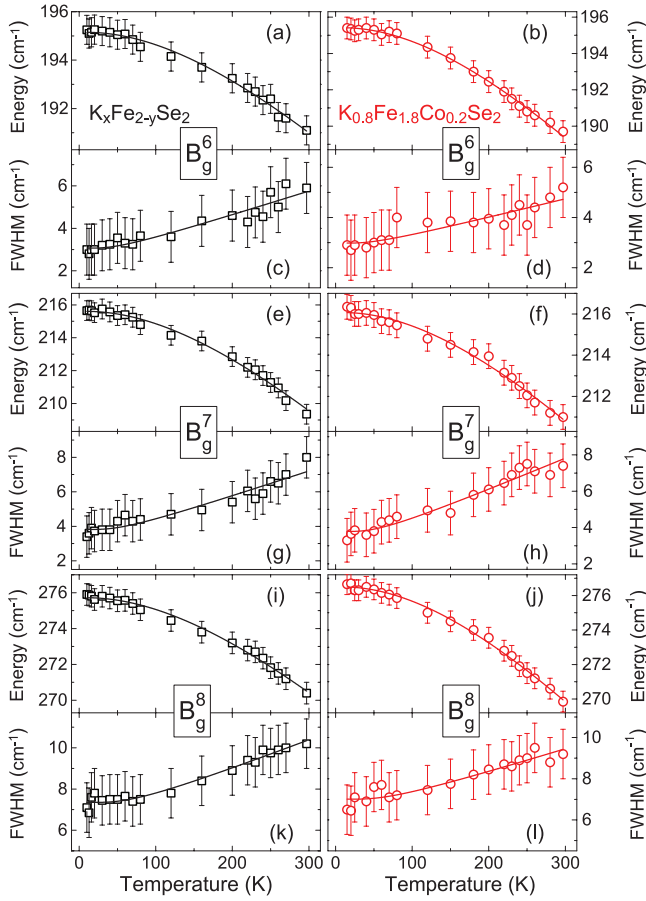
Figure 5. Temperature dependence of energy and linewidth for (a)–(d) B_g^6, (e)–(h) B_g^7 and (i)–(l) B_g^8 modes of $K_xFe_{2-y}Se_2$ (left panels) and $K_{0.8}Fe_{1.8}Co_{0.2}Se_2$ (right panels) single crystals. Solid lines are plotted according to (2) (taking into account only the volume contribution to the phonon mode energy) and (6).
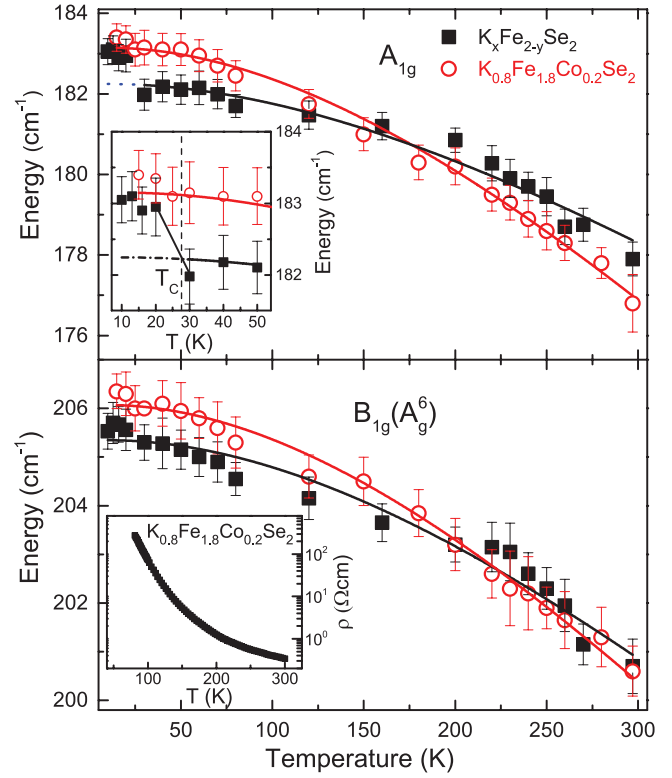

Figure 6. Temperature dependence of the energy for the A_{1g} and $B_{1g}(A_g^6)$ Raman modes of $K_xFe_{2-y}Se_2$ and $K_{0.8}Fe_{1.8}Co_{0.2}Se_2$ single crystals. Upper inset: an enlarged view of the dependence of the A_{1g} mode energy on temperature in a low-temperature region near T_C. Lower inset: the temperature dependence of the electrical resistivity for $K_{0.8}Fe_{1.8}Co_{0.2}Se_2$ shows the nonmetallic behavior of this single crystal.

4. Conclusion

In this article a Raman scattering study of superconducting $K_xFe_{2-y}Se_2$ and non-superconducting $K_{0.8}Fe_{1.8}Co_{0.2}Se_2$ single crystals has been presented. Two Raman active modes from the superconducting (I4/mmm) phase and seven phonon modes from the insulating (I4/m) phase are observed in the investigated frequency range. The same number of observed modes in these two compounds, together with their similar energies, suggests that phase separation is also present in a $K_{0.8}Fe_{1.8}Co_{0.2}Se_2$ single crystal. The temperature-induced change of Raman mode linewidth is in good agreement with the lattice anharmonicity model. The behavior of the Raman mode energy as a function of temperature for all the analyzed modes is well described by the contribution from the lattice thermal expansion alone. The sudden change in the A_{1g} mode energy near T_C in $K_xFe_{2-y}Se_2$ is due to the rearrangement of the electronic states to which this mode couples as the superconducting gap opens. A rather small electron–phonon coupling constant at the Γ-point is obtained from the superconductivity-induced A_{1g} phonon energy renormalization.

References

[1] Guo J, Jin S, Wang G, Wang S, Zhu K, Zhou T, He M and Chen X 2010 *Phys. Rev.* B **82** 180520
[2] Stewart G R 2011 *Rev. Mod. Phys.* **83** 1589–652
[3] Liu R H *et al* 2011 *Europhys. Lett.* **94** 27008
[4] Fang M, Wang H, Dong C and Huang Q 2013 *J. Phys.: Conf. Ser.* **449** 012015
[5] Litvinchuk A P, Hadjiev V G, Iliev M N, Lv B, Guloy A M and Chu C W 2008 *Phys. Rev.* B **78** 060503
[6] Ge J-F, Liu Z-L, Liu C, Gao C-L, Qian D, Xue Q-K, Liu Y and Jia J-F 2015 *Nat. Mater.* **14** 285–9

[7] Dagotto E 2013 *Rev. Mod. Phys.* **85** 849–67

[8] Bao W, Huang Q-Z, Chen G-F, Green M A, Wang D-M, He J-B and Qiu Y-M 2011 *Chin. Phys. Lett.* **28** 086104

[9] Xu M *et al* 2012 *Phys. Rev. B* **85** 220504

[10] Ding X, Pan Y, Yang H and Wen H-H 2014 *Phys. Rev. B* **89** 224515

[11] Li W *et al* 2012 *Nat. Phys.* **8** 126–30

[12] Chen F *et al* 2011 *Phys. Rev. X* **1** 021020

[13] Liu Y, Xing Q, Dennis K W, McCallum R W and Lograsso T A 2012 *Phys. Rev. B* **86** 144507

[14] Yi M *et al* 2013 *Phys. Rev. Lett.* **110** 067003

[15] Ding X, Fang D, Wang Z, Yang H, Liu J, Deng Q, Ma G, Meng C, Hu Y and Wen H-H 2013 *Nat. Commun.* **4** 1897

[16] Tan D *et al* 2011 *Phys. Rev. B* **84** 014502

[17] Ryu H, Abeykoon M, Wang K, Lei H, Lazarević N, Warren J B, Bozin E S, Popović Z V and Petrovic C 2015 *Phys. Rev. B* **91** 184503

[18] Zhang A M, Liu K, Xiao J H, He J B, Wang D M, Chen G F, Normand B and Zhang Q M 2012 *Phys. Rev. B* **85** 024518

[19] Lazarević N, Abeykoon M, Stephens P W, Lei H, Bozin E S, Petrovic C and Popović Z V 2012 *Phys. Rev. B* **86** 054503

[20] Ignatov A, Kumar A, Lubik P, Yuan R H, Guo W T, Wang N L, Rabe K and Blumberg G 2012 *Phys. Rev. B* **86** 134107

[21] Lei H and Petrovic C 2011 *Phys. Rev. B* **84** 212502

[22] Margadonna S, Takabayashi Y, McDonald M T, Kasperkiewicz K, Mizuguchi Y, Takano Y, Fitch A N, Suard E and Prassides K 2008 *Chem. Commun.* **43** 5607–9

[23] Gnezdilov V, Pashkevich Y G, Lemmens P, Wulferding D, Shevtsova T, Gusev A, Chareev D and Vasiliev A 2013 *Phys. Rev. B* **87** 144508

[24] Lazarević N, Radonjić M, Šćepanović M, Lei H, Tanasković D, Petrovic C and Popović Z V 2013 *Phys. Rev. B* **87** 144305

[25] Mittal R, Gupta M K, Chaplot S L, Zbiri M, Rols S, Schober H, Su Y, Brueckel T and Wolf T 2013 *Phys. Rev. B* **87** 184502

[26] Lazarević N, Lei H, Petrovic C and Popović Z V 2011 *Phys. Rev. B* **84** 214305

[27] Menéndez J and Cardona M 1984 *Phys. Rev. B* **29** 2051–9

[28] Eiter H-M, Jaschke P, Hackl R, Bauer A, Gangl M and Pfleiderer C 2014 *Phys. Rev. B* **90** 024411

[29] Böhmer A E, Hardy F, Eilers F, Ernst D, Adelmann P, Schweiss P, Wolf T and Meingast C 2013 *Phys. Rev. B* **87** 180505

[30] Cardona M 2002 *Ultrafast Dynamics of Quantum Systems* (*NATO Science Series B* vol 372) (Berlin: Springer) pp 257

[31] Litvinchuk A P, Lv B and Chu C W 2011 *Phys. Rev. B* **84** 092504

[32] Um Y J, Bang Y, Min B H, Kwon Y S and Le Tacon M 2014 *Phys. Rev. B* **89** 184510

[33] Choi K-Y, Lemmens P, Eremin I, Zwicknagl G, Berger H, Sun G L, Sun D L and Lin C T 2010 *J. Phys.: Condens. Matter* **22** 115802

[34] Zeyher R and Zwicknagl G 1990 *Z. Phys. B* **78** 175–90

Sustained phase separation and spin glass in Co-doped K$_x$Fe$_{2-y}$Se$_2$ single crystals

Hyejin Ryu (류혜진),[1,2,*] Kefeng Wang (王克锋),[1,†] M. Opacic,[3] N. Lazarevic,[3] J. B. Warren,[4]
Z. V. Popovic,[3] Emil S. Bozin,[1] and C. Petrovic[1,2]

[1]*Condensed Matter Physics and Materials Science Department, Brookhaven National Laboratory, Upton, New York 11973, USA*
[2]*Department of Physics and Astronomy, Stony Brook University, Stony Brook, New York 11794-3800, USA*
[3]*Center for Solid State Physics and New Materials, Institute of Physics Belgrade, University of Belgrade,*
Pregrevica 118, 11080 Belgrade, Serbia
[4]*Instrument Division, Brookhaven National Laboratory, Upton, New York 11973, USA*

We present Co substitution effects in K$_x$Fe$_{2-y-z}$Co$_z$Se$_2$ ($0.06 \leqslant z \leqslant 1.73$) single-crystal alloys. By 3.5% of Co doping superconductivity is suppressed, whereas phase separation of semiconducting K$_2$Fe$_4$Se$_5$ and superconducting/metallic K$_x$Fe$_2$Se$_2$ is still present. We show that the arrangement and distribution of the superconducting phase (stripe phase) are connected with the arrangement of K, Fe, and Co atoms. Semiconducting spin glass is found in proximity to the superconducting state, persisting for large Co concentrations. At high Co concentrations a ferromagnetic metallic state emerges above the spin glass. This is coincident with changes of the unit cell and arrangement and connectivity of the stripe conducting phase.

I. INTRODUCTION

Since the discovery of high-temperature Fe-based superconductivity [1], many types of Fe-based superconductors have been reported, including K$_x$Fe$_{2-y}$Se$_2$ [2,3]. Various novel phenomena were observed by chemical substitution on the Fe site. For example, Co and Ni doping in FeAs tetrahedra of LaFeAsO and BaFe$_2$As$_2$-based pnictides gives rise to superconductivity [4–7], whereas Co doping in FeSe suppresses superconductivity [8,9]. In particular, A_xFe$_{2-y}$Se$_2$ (A = K, Cs, Rb, Tl) materials are strongly sensitive to chemical substitutions [10–12].

Among several different types of Fe-based superconductors, A_xFe$_{2-y}$Se$_2$ (A = K, Cs, Rb, Tl) materials generate significant attention due to unique characteristics such as the absence of the pocket in the Brillouin zone center and phase separation with the Fe-vacancy order where the crystal separates into (super)conducting stripes (block) and magnetic semiconducting matrix regions on the 0.01–100-μm scale [13–18]. The mechanism of the conducting and nonconducting states in proximity to K$_x$Fe$_{2-y}$Se$_2$ is of great importance for understanding superconductivity [19,20]. Consequently, the details of phase separation, phase stoichiometry, compositions, and their magnetic and electric ground states are currently being debated and are of high interest.

In this study we have investigated K$_x$Fe$_{2-y-z}$Co$_z$Se$_2$ ($0.06 \leqslant z \leqslant 1.73$) single-crystal alloys, where y is a Fe/Co vacancy. A rich phase diagram is discovered, where a phase-separated superconducting state of K$_x$Fe$_{2-y}$Se$_2$ turns into a spin glass and then into a KCo$_{1.73}$Se$_2$ ferromagnetic metal with no phase separation. We show that the microstructure arrangement and connectivity are rather important for ground-state changes, in addition to changes induced by Co substitution for Fe.

II. EXPERIMENT

Single crystals of K$_x$Fe$_{2-y-z}$Co$_z$Se$_2$ ($0.06 \leqslant z \leqslant 1.73$) were synthesized as described previously [21]. Platelike crystals with size up to $10 \times 10 \times 3$ mm^3 were obtained. A high-energy medium-resolution synchrotron x-ray experiment at 300 K was conducted on the X7B beamline of the National Synchrotron Light Source at Brookhaven National Laboratory. The setup utilized an x-ray beam 0.5×0.5 mm in size with a wavelength of 0.3196 Å ($E = 38.7936$ keV) configured with a focusing double-crystal bent Laue monochromator and a Perkin-Elmer amorphous silicon image plate detector mounted perpendicular to the primary beam path. Finely pulverized samples were packed in cylindrical polyimide capillaries 1 mm in diameter and placed 377.81 mm away from the detector. Multiple scans were performed to a total exposure time of 240 s. The two-dimensional (2D) diffraction data were integrated and converted to intensity versus 2θ using the software FIT2D [22]. Structural refinements were carried out using the GSAS modeling program [23] operated by the EXPGUI platform [24]. The backscattered images and energy dispersive x-ray spectroscopy (EDX) mappings were performed in a JEOL-6500 scanning electron microscope (SEM). Electrical transport, thermal transport, heat capacity, and magnetization measurements were carried out in Quantum Design PPMS-9 and MPMS-XL5. Raman scattering measurements were performed on freshly cleaved (001)-oriented samples using TriVista 557 and Jobin Yvon T64000 Raman systems in backscattering micro-Raman configuration. The 514.5-nm laser line of a mixed Ar$^+$/Kr$^+$ gas laser was used as an excitation source. All measurements were carried out at room temperature in the vacuum.

III. RESULTS AND DISCUSSION

The obtained high-energy synchrotron x-ray-diffraction data of the K$_x$Fe$_{2-y-z}$Co$_z$Se$_2$ series [Fig. 1(a)] can be fitted very well with $I4/m$ and $I4/mmm$ space groups for $z \leqslant 0.92(4)$, while they are fitted by the $I4/mmm$ space group only for $z > 0.92(4)$. This implies coexistence of

---

*Present address: Advanced Light Source, E. O. Lawrence Berkeley National Laboratory, Berkeley, California 94720, USA.

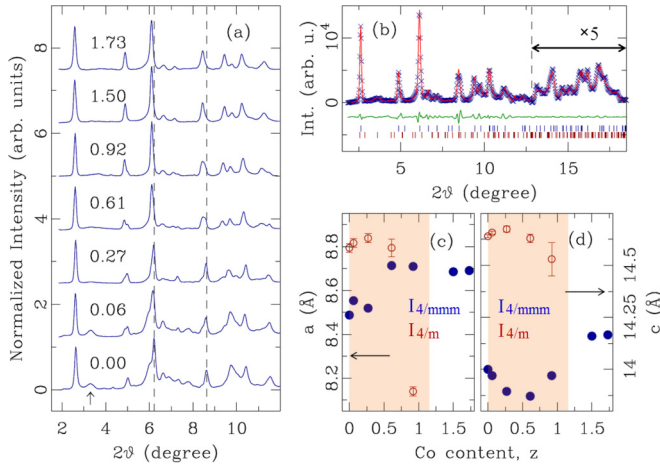†Present address: CNAM, Department of Physics, University of Maryland, College Park, Maryland 20742, USA.

FIG. 1. (Color online) (a) High-energy synchrotron x-ray diffraction data of the $K_x Fe_{2-y-z} Co_z Se_2$ series, normalized by the intensity of (002) reflection for comparison. Data are offset for clarity and labeled by respective Co content as measured by EDX. Vertical dashed lines are provided as a visual reference. Vertical arrow indicates (110) reflection, which is a hallmark of the $I4/m$ phase. Coexistence of the $I4/m$ and $I4/mmm$ phases can be visually tracked up to $z = 0.92(4)$ cobalt content in the samples studied. (b) Modeling of powder diffraction data for a sample with $z = 0.92(4)$. Crosses represent data, red solid line is the model, and green solid line is the difference, which is offset for clarity. Vertical ticks mark the reflections in the $I4/mmm$ (top row) and $I4/m$ (bottom row) phases. (c) and (d) Evolution with EDX-established Co content of refined lattice parameters for $I4/mmm$ (solid blue circles) and $I4/m$ (open red circles). All parameters are expressed in the $I4/m$ metrics (see text). The shaded region is where the signatures of the phase coexistence could be reliably established from the diffraction data.

$I4/m$ and $I4/mmm$ phases when $z \leqslant 0.92(4)$. The typical fit for a phase-separated sample with $z = 0.92(4)$ is shown in Fig. 1(b). Notably, for $0.27 \leqslant z \leqslant 0.92$ intensities of reflections characteristic of the $I4/m$ phase become appreciably weaker and rather broad, indicative of disorder and loss of structural coherence of this structural component, as well as its presumably diminishing contribution. However, quantitative phase analysis was not feasible due to the limited resolution of the measurement and due to the diffuse nature of the signal with broad and overlapping reflections. The evolution of extracted lattice parameters with Co content is shown in Figs. 1(c) and 1(d). Lattice parameters for the a axis of the $I4/mmm$ space group are converted into comparable numbers for the $I4/m$ space group using the formula $I4/m = \sqrt{5}\, I4/mmm$. Nonmonotonic evolution of the lattice parameters highlights the complex crystal structure and bonding in $K_x Fe_{2-y-z} Co_z Se_2$.

The surface morphologies (Fig. 2) show that the Co-doped crystals separate into two regions, a stripe- (domain-) like brighter area that is 1–2 μm thick and a darker matrix area, similar to pure $K_x Fe_{2-y} Se_2$ [17], implying that the phase separation is preserved with Co doping. Distributions of the elements of $K_x Fe_{2-y-z} Co_z Se_2$ in the samples investigated by EDX mapping are shown in Figs. 2(a)–2(c). The bright colored area is the area covered by each element. Se is uniformly distributed for all three samples, while K, Fe, and Co display
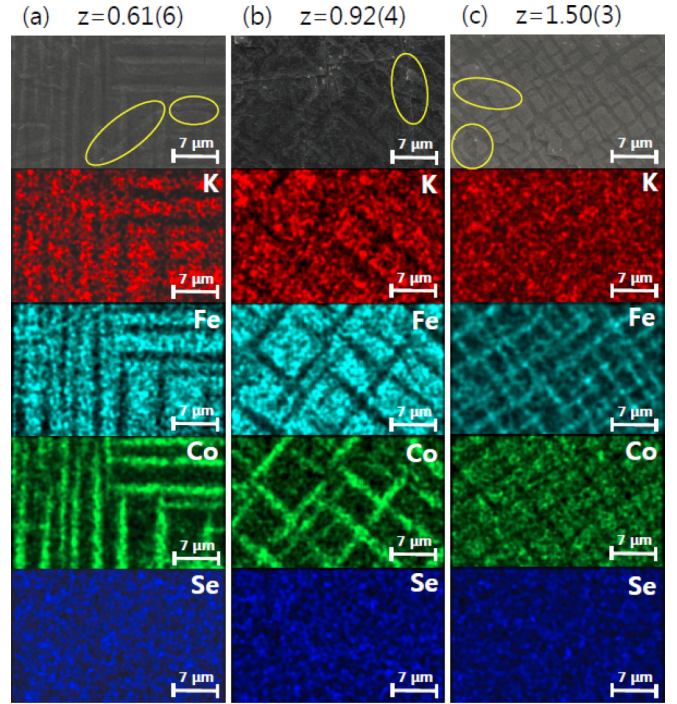

FIG. 2. (Color online) Backscattered electron images of SEM measurement and EDX mappings of $K_x Fe_{2-y-z} Co_z Se_2$ when (a) $z = 0.61(6)$, (b) $z = 0.92(4)$, and (c) $z = 1.50(3)$.

a pattern similar to the backscattered electron image. This suggests that only K, Fe, and Co elements are responsible for phase separation. It is clear that the K and Fe concentrations are lower in the stripes (domains) than in the matrix, while Co concentration is higher in the stripes than in the matrix. Hence, Co atoms prefer to enter into the stripe (domain) phase, which is consistent with the report that Co substitution strongly suppresses superconductivity [12]. The stripe- (domain-) like brighter area maintain its shape across the terraces created by the cleaving, as shown by the marked ellipses in Fig. 2. This may suggest that the stripe- (domain-) like brighter areas form a three-dimensional spider-web-like network [17].

The average stoichiometry was measured by EDX for several single crystals in the same batch with multiple measuring points. The results indicate that the crystals are homogeneous within the scale of around $1 \times 1 \times 0.5$ mm^3. The determined stoichiometries when fixing Se stoichiometry to 2 are shown in Table I. Defects and vacancies of Fe and Co

TABLE I. Summary of measured compositions of $K_x Fe_{2-y-z} Co_z Se_2$ samples.

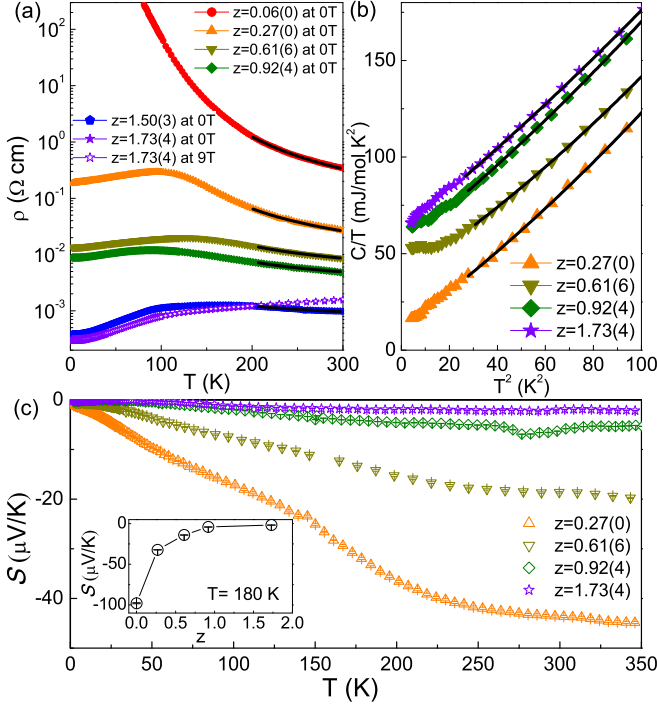| Nominal composition	Measured composition			
K:Fe:Co:Se	K	Fe	Co	Se
1:1.8:0.2:2	0.79(5)	1.37(3)	0.06(0)	2
1:1.4:0.6:2	0.76(1)	1.12(1)	0.27(0)	2
1:1:1:2	0.77(2)	0.92(4)	0.61(6)	2
1:0.6:1.4:2	0.81(2)	0.60(3)	0.92(4)	2
1:0.2:1.8:2	0.78(2)	0.19(1)	1.50(3)	2
1:0:2:2	0.60(6)	0	1.73(4)	2

FIG. 3. (Color online) (a) Temperature dependence of the in-plane resistivity $\rho(T)$ of $K_x Fe_{2-y-z} Co_z Se_2$ series at zero (solid symbols) and 9 T field (open symbols). The black solid lines are the fitted result using the thermal activation model. (b) The relation between C/T and T^2 for $K_x Fe_{2-y-z} Co_z Se_2$ series at low temperature. The solid lines represent fits by the equation $C/T = \gamma + \beta_3 T^2 + \beta_5 T^4$. (c) Temperature dependence of thermoelectric power $S(T)$ for $K_x Fe_{2-y-z} Co_z Se_2$ series. The inset shows the thermoelectric power at $T = 180$ K for different Co concentrations.

are observed for all investigated crystals, which is common in $A_x Fe_{2-y} Se_2$ (A = K, Cs, Rb, Tl) compounds [3,25,26]. As the ratio of Co increases, the sum of Fe and the Co ratio slightly increases, while the K ratio remains almost constant, similar to Ni-doped $K_x Fe_{2-y} Se_2$ series [27].

As shown in Fig. 3(a), 3.5% of Co doping in $K_x Fe_{2-y} Se_2$ completely suppresses the superconductivity and results in a semiconducting $\rho(T)$, consistent with previous research [12]. As Co composition increases, there is a crossover from a semiconductor to metallic state. Besides $K_x Co_{1.73(4)} Se_2$, all other crystals are metallic below a resistivity maximum ρ_{max} and semiconducting above ρ_{max}, similar to $K_x Fe_{2-y} Se_{2-z} S_z$ [21]. The high-temperature part (above 200 K) of $\rho(T)$ can be fitted by the thermal activation model $\rho = \rho_0 \exp(E_a / k_B T)$, where ρ_0 is a prefactor, E_a is an activation energy, and k_B is Boltzmann's constant [Fig. 3(a)]. The obtained ρ_0 and E_a are listed in Table II and are mostly smaller than values for $K_x Fe_{2-y} S_2$ and $KFe_{0.85} Ag_{1.15} Te_2$ [25,28].

The heat capacity of the $K_x Fe_{2-y-z} Co_z Se_2$ series also exhibits the crossover from semiconductor to metal as Co increases, consistent with resistivity [Fig. 3(b)]. $C/T - T^2$ relations between 5 and 10 K can be fitted by the formula $C/T = \gamma + \beta_3 T^2 + \beta_5 T^4$. The Debye temperatures are obtained from $\Theta_D = (12\pi^4 N R / 5\beta)^{1/3}$, where N is the atomic number in the chemical formula and R is the gas constant. The obtained γ values and Debye temperatures Θ_D for different

TABLE II. Summary of ρ_0 values and activation energy E_a in $K_x Fe_{2-y-z} Co_z Se_2$.

z	ρ_0 (mΩ cm)	E_a (meV)
0.06(0)	24.3(4)	67.7(4)
0.27(0)	4.20(9)	47.1(5)
0.61(6)	3.07(1)	26.6(1)
0.92(4)	2.15(3)	21.4(3)
1.50(3)	0.597(7)	12.4(2)

Co ratios are listed in Table III. The Debye temperature for the $K_x Fe_{2-y-z} Co_z Se_2$ series are similar, suggesting that there are no considerable changes in atomic weight, structure, and bonding. A small γ value for $z = 0.27(0)$ implies a low density of states at the Fermi level, similar to typical semiconductors, while large γ values for $z \geq 0.92(4)$ suggest accumulation of the density of states, as expected in metals.

Thermoelectric power $S(T)$ of the $K_x Fe_{2-y-z} Co_z Se_2$ series shows negative values for all different Co concentrations, which reveals that dominant carriers are electrons [Fig. 3(c)]. The magnitude of $S(z)$ decreases as the Co ratio increases to around 50% [$z = 0.92(4)$] and saturates [inset in Fig. 3(c)]. There are no obvious peaks in the thermoelectric power for the $K_x Fe_{2-y-z} Co_z Se_2$ series between 2 and 350 K, suggesting that there are no dramatic Fermi surface changes.

The temperature-dependent dc magnetic susceptibilities of the $K_x Fe_{2-y-z} Co_z Se_2$ series show irreversible behaviors between zero-field cooling (ZFC) and field cooling (FC) at low temperature [Fig. 4(a)]. This is a typical behavior of a spin glass in magnetic field caused by the frozen magnetic spins in random directions below the characteristic temperature T_f. Insets in Figs. 4(a) and 4(b) also suggest a spin glass due to the linear field dependence of the magnetic susceptibility with no hysteresis above T_f (measured at 300 K) and an S-shaped loop of the $M-H$ curve below T_f (measured at 1.8 K). Hence, 3.5% Co doping ($z = 0.06$) not only suppresses superconductivity but also may result in a spin glass. Ferromagnetic behavior appears when $z \geq 1.50(3)$ [29]. High-temperature regions ($T \geq 150$ K) of the $K_x Fe_{2-y-z} Co_z Se_2$ series follow the Curie-Weiss law $\chi(T) = \chi_0 + C/(T - \theta)$, where χ_0 includes core diamagnetism and van Vleck and Pauli paramagnetism, C is the Curie constant, and θ is the Curie-Weiss temperature [Figs. 4(a) and 4(b)]. The obtained parameters are summarized in Table IV. Negative θ values are observed even for crystals that order ferromagnetically, suggesting prevalent antiferromagnetic interactions probably come from the localized moment of the block (stripe) domain due to the phase separation.

TABLE III. Summary of γ values and Debye temperatures of $K_x Fe_{2-y-z} Co_z Se_2$.

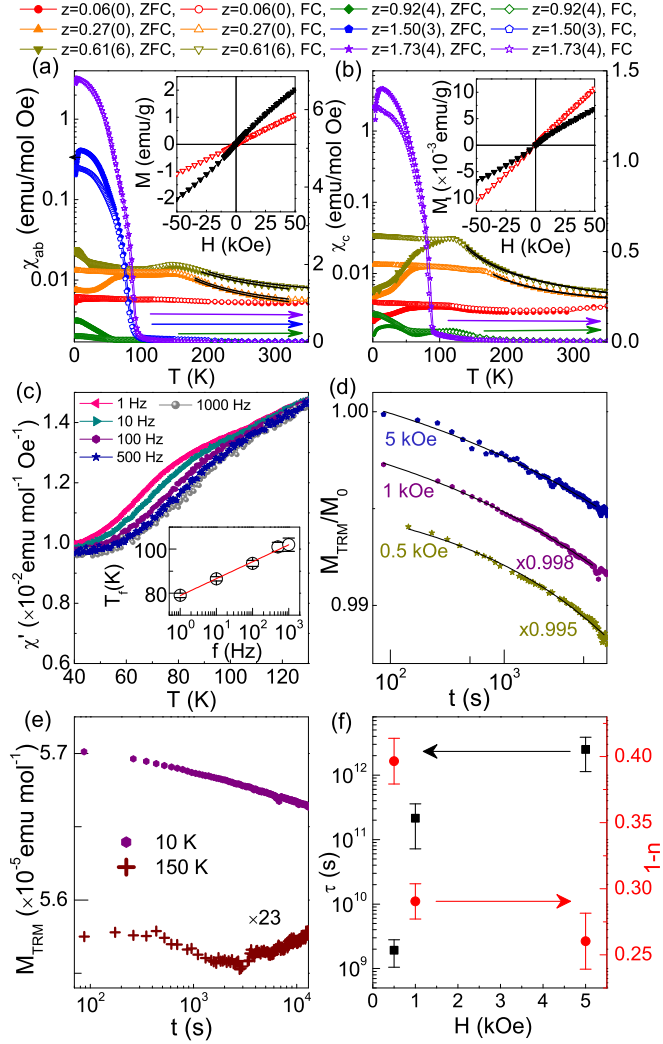| z	γ (mJ mol^{-1} K^{-2})	Θ_D (K)
0.27(0)	11(1)	220(4)
0.61(6)	38(1)	227(3)
0.92(4)	54(1)	215(3)
1.73(4)	63(1)	213(2)

FIG. 4. (Color online) Temperature dependence of dc magnetic susceptibilities of $K_xFe_{2-y-z}Co_zSe_2$ series for (a) $H \perp c$ and (b) $H \parallel c$ at $H = 1$ kOe in ZFC and FC below 350 K. Insets in (a) and (b) are $M-H$ curves of $K_xFe_{2-y-z}Co_zSe_2$ with $z = 0.61(6)$ for $H \perp c$ and $H \parallel c$, respectively, at 1.8 K (black solid inverse triangle) and 300 K (red open inverse triangle). (c) Temperature dependence of ac susceptibility $\chi'(T)$ measured at five different frequencies for $z = 0.27(0)$ of $K_xFe_{2-y-z}Co_zSe_2$. The inset shows the frequency dependence of T_f with the linear fitting (solid line). (d) TRM vs time for $z = 0.27(0)$ of $K_xFe_{2-y-z}Co_zSe_2$ at 10 K and $t_w = 100$ s with different dc fields with fittings using stretched exponential function (solid lines). (e) M_{TRM} vs t at 10 and 150 K with $H = 1$ kOe and $t_w = 100$ s. (f) H-field dependence $\tau(s)$ (black solid square) and $1 - n$ (red solid circle).

Confirmation of the spin glass comes from the frequency dependence of the real part of ac susceptibility and thermoremanent magnetization. The frequency-dependent susceptibility $\chi'(T)$ is shown in Fig. 4(c). As frequency increases, the characteristic temperature T_f peak position increases, whereas its magnitude decreases [30]. The frequency dependence of the peak shift is fitted by $K = \Delta T_f/(T_f \Delta \log f)$ (Fig. 4), and the obtained K value is 0.036(1), in agreement with the canonical spin-glass values ($0.0045 \leqslant K \leqslant 0.08$) [30]. Thermoremanent magnetization (TRM) is shown in Fig. 4(d).

TABLE IV. Summary of χ_0, effective moment μ_{eff}, and θ values from Curie-Weiss fitting of $K_xFe_{2-y-z}Co_zSe_2$.

z		χ_0 (emu mol^{-1}Oe^{-1})	μ_{eff} (μ_B/Fe)	θ (K)
0.27(0)	$H \perp c$	$2.4(2) \times 10^{-3}$	2.33(8)	$-91(5)$
	$H \parallel c$	$2.7(1) \times 10^{-3}$	1.88(6)	$-118(3)$
0.61(0)	$H \perp c$	$1.6(1) \times 10^{-3}$	2.76(3)	$-98(1)$
	$H \parallel c$	$3.7(4) \times 10^{-3}$	2.79(9)	$-81(9)$
0.92(4)	$H \perp c$	$3.6(4) \times 10^{-3}$	2.7(2)	$-120(9)$
	$H \parallel c$	$2.8(1) \times 10^{-3}$	2.38(2)	$-146(1)$
1.50(3)	$H \perp c$	$9.9(1) \times 10^{-3}$	1.42(4)	$-218(2)$
	$H \parallel c$	$8.2(2) \times 10^{-3}$	0.65(9)	$-257(6)$
1.73(4)	$H \perp c$	$7.9(9) \times 10^{-4}$	3.2(4)	$-86(9)$
	$H \parallel c$	$2.9(8) \times 10^{-3}$	1.8(6)	$-138(9)$

The sample was cooled down from 200 K (above T_f) to 10 K (below T_f) in four different magnetic fields, then kept at 10 K for $t_w = 100$ s. After that, the magnetic field was removed, and $M_{TRM}(t)$ was measured. As observed in Fig. 4(d), $M_{TRM}(t)$ decays very slowly for all three different magnetic fields towards its nonzero equilibrium value [30]. On the other hand, $M_{TRM}(t)$ measured at 150 K (above T_f) relaxes quickly in a short time [less than $\sim$100 s; Fig. 4(e)]. Slow relaxation behavior is fitted well by the stretched exponential function, $M_{TRM}(t) \sim M_0 \exp[-(t/\tau)^{1-n}]$, where M_0, τ, and $1 - n$ are the glassy component, the relaxation characteristic time, and the critical exponent, respectively. As shown in Fig. 4(f), the obtained τ increases as the H field increases, while $1 - n$ stays close to 1/3, consistent with theoretical and experimental results for a spin-glass system [31,32].

Figure 5(a) shows polarized Raman scattering spectra of a $K_{0.6}Co_{1.73}Se_2$ single crystal measured from the (001) plane for the two sample orientations at 100 K using the Jobin Yvon T64000 Raman system. According to selection rules for the $I4/mmm$ space group, peaks at about 174 and 184 cm^{-1} (at 100 K) are assigned as B_{1g} and A_{1g} Raman modes, respectively [33,34].

Unpolarized Raman scattering spectra of $K_xFe_{2-y-z}Co_zSe_2$ single crystals are presented in Fig. 5(b). For $z = 1.73(4)$ samples, only two peaks, which were assigned as A_{1g} ($\sim$180 cm^{-1}) and B_{1g} ($\sim$169 cm^{-1}) modes, can be observed in the Raman spectrum. These modes are also observed for $z = 1.50(3)$ and $z = 0.92(4)$ samples. In fact, the A_{1g} mode can be observed in Raman spectra for all concentrations of cobalt, suggesting that superconducting/metallic $K_xFe_2Se_2$ phase is present in all investigated samples. The energy of this mode does not change significantly by varying concentrations of Co or for different transition-metal ions [33,34]. For the intermediate concentration [$0.61(6) \leqslant z \leqslant 1.50(3)$] a broad structure around 250 cm^{-1} has been observed, which probably originates from the crystalline disorder in the semiconducting $K_2Fe_4Se_5$ phase. In general, high disorder may cause relaxation of the selection rules, resulting in the appearance of broad asymmetric structures. With further decreasing the Co concentration [$z \leqslant 0.27(0)$], a large number of Raman modes can be clearly observed in the spectra in addition to the A_{1g} mode of the superconducting/metallic $K_xFe_2Se_2$ phase. These
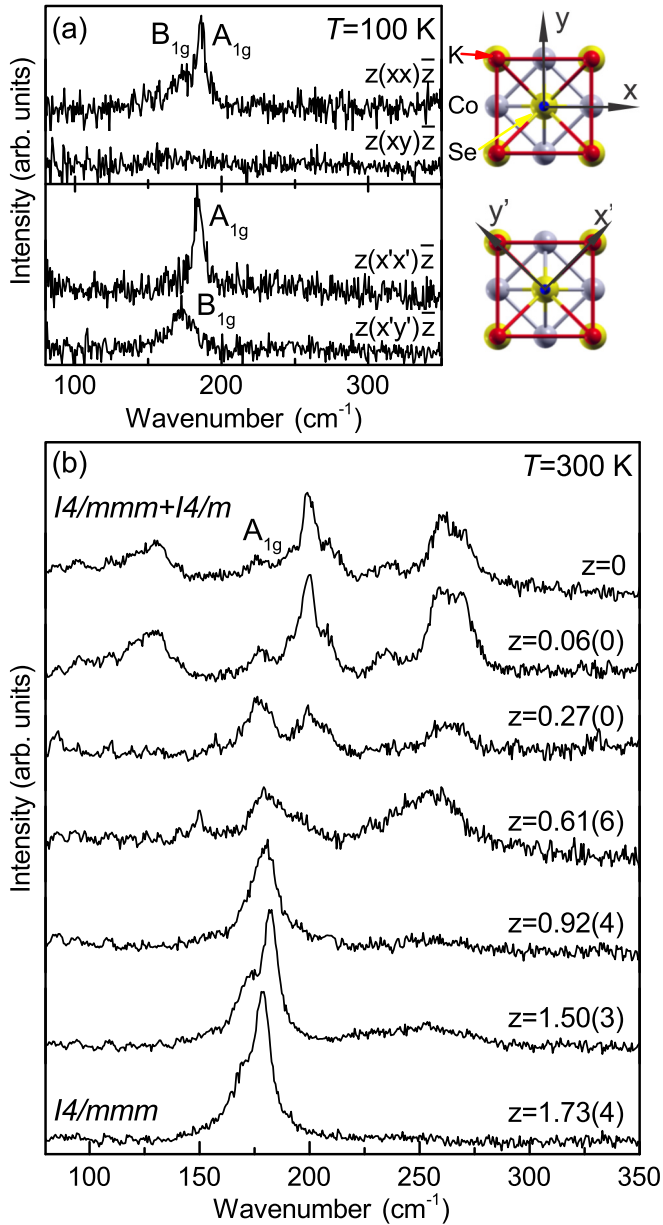
FIG. 5. (Color online) (a) Raman scattering spectra of $K_{0.6}Co_{1.73}Se_2$ single crystals in various scattering configurations $(\mathbf{x} = [100], \mathbf{y} = [010], \mathbf{x}' = 1/\sqrt{2}[110], \mathbf{y}' = 1/\sqrt{2}[1\bar{1}0])$. (b) Raman scattering spectra of $K_xFe_{2-y-z}Co_zSe_2$, $[0 \leqslant z \leqslant 1.73(4)]$ single crystals measured at room temperature from the (001) plane of the samples.

modes originate from the lattice vibrations within the ordered low-symmetry semiconducting $K_2Fe_4Se_5$ phase [33,35].

The magnetic and transport phase diagram of $K_xFe_{2-y-z}Co_zSe_2$ series is presented in Fig. 6. When $z \sim 0$ there is superconductivity below $T_c \sim 30$ K and metallic resistivity below and semiconducting above about 125 K [3]. By 3.5% Co doping, not only is superconductivity completely suppressed, but so is conductivity with emerging spin-glass magnetic order below $T_f \sim 70$ K in 1 kOe. A semiconducting/bad-metal spin glass is found in proximity to the superconducting state, similar to copper oxides. As Co
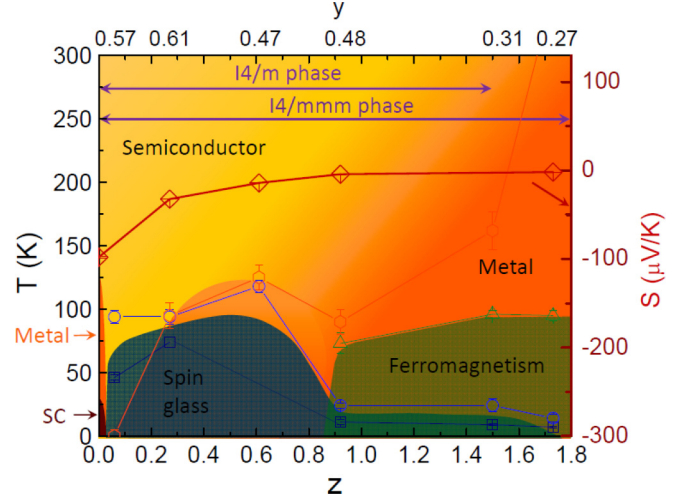

FIG. 6. (Color online) Magnetic and transport phase diagram. Open squares and open circles are spin-glass characteristic temperature T_f for the $H \perp c$ and $H \parallel c$ directions, respectively. Open triangles are the ferromagnetic transition temperature, and open diamonds are the thermoelectric power S_T at 180 K. Open hexagons are resistivity maximums ρ_{max}, which show the semiconductor (brighter yellow region) to metal (darker orange region) crossover. The lines at the top denote the regions of the ordered $I4/m$ and $I4/mmm$ space groups.

concentration increases, the spin-glass state is maintained, while the semiconductor to metal crossover is present at low temperatures up to $z \sim 0.6$. After that, the spin glass and metallicity decrease up to $z \sim 0.9$. With a further increase in Co concentration, metallic conductivity spreads to higher temperatures, while the spin glass is suppressed to the lower-temperature region (below ~ 20 K), and the ferromagnetic ground state emerges above the spin glass. $K_xCo_zSe_2$ with $z = 1.73(4)$ is a metal, consistent with previous reports [29]. We also note that ground-state changes (Fig. 6) are concurrent with lattice parameter variations. Lattice parameters a and c for $I4/m$ show a general drop as z is increased, in contrast to lattice parameters of $I4/mmm$. When the ferromagnetism emerges, lattice parameter c in $I4/mmm$ rapidly increases and is saturated, similar to the temperature dependence of the Curie temperature.

It should be noted that both metallic conductivity and the total area of brighter stripe (block) regions increase with z. This could imply that the brighter stripe (block) area is metallic, whereas the matrix is semiconducting, both with and without Co doping [36,37]. The $z = 0.06(0)$ crystal shows semiconducting behavior through the entire temperature region we measured (1.8 K $\leqslant T \leqslant$ 300 K), even though the metallic brighter stripe (block) areas are present (Fig. 2). This is most likely because the connectivity of the three-dimensional metallic stripe (block) area is insufficient to create metallic percolation in the crystal.

The composite nature of our crystals and nano- to mesoscale mix of (super)conducting and semiconducting magnetic regions may also create states at interfaces [38,39]. This somewhat complicates the physical interpretation of bulk measurements. However, since in $K_xFe_{2-\delta}Se_2$ nanoscale phase

separation exists below $T_s = 560$ K [18], most of the conductivity changes below T_s should come from the metallic regions. This is supported by recent angle-resolved photoemission results where an orbital-selective Mott transition in $K_x Fe_{2-\delta} Se_2$ was observed above the crossover temperature [40]. Therefore, the absolute values of resistivity and magnetization reflect the contribution of both the semiconducting $K_2 Fe_4 Se_5$ and superconducting/metallic $K_x Fe_2 Se_2$ parts of the crystal. Obtained thermoelectric power and heat capacity are contributed by the metallic phase and the semiconducting phase, weighted by their conductivity. The estimated conductivity ratio between two phases is around $\sim 10^3$ at 180 K, which implies the contribution of the metallic region is 1000 times larger than that of the semiconducting region. Co substitution in the superconducting/metallic $K_x Fe_2 Se_2$ unit cell is likely to have a stronger effect on states associated with itinerant d_{xz}/d_{yz} orbitals, for example, via the localization effect in an orbital-selective Mott localization scenario [41,42]. Further Co substitution and disorder might enhance conductivity by raising the chemical potential and enlarging electron pockets, in agreement with our phase diagram [43–45].

IV. CONCLUSION

We have demonstrated how the structure, phase separation, transport, and magnetic property evolve with Co doping concentration in $K_x Fe_{2-y-z} Co_z Se_2$ single crystals. A rich ground-state phase diagram was discovered. By 3.5% Co doping superconductivity is suppressed, while phase separation is still present, which asserts the significance of the arrangement and connectivity of phases for superconductivity. A semiconducting spin glass was discovered in close proximity to the superconducting state in the phase diagram, similar to copper oxides. A ferromagnetic metal state emerged above $\sim$50% Co concentration, in agreement with the structural changes. The metallicity becomes dominant as the area of stripe (block) phases increases; however, the connectivity of stripe phases may also be important for metallic conductivity.

[1] Y. Kamihara, T. Watanabe, M. Hirano, and H. Hosono, J. Am. Chem. Soc. **130**, 3296 (2008).

[2] S. Fujitsu, S. Matsuishi, and H. Hosono, Int. Mater. Rev. **57**, 311 (2012).

[3] J. Guo, S. Jin, G. Wang, S. Wang, K. Zhu, T. Zhou, M. He, and X. Chen, Phys. Rev. B **82**, 180520(R) (2010).

[4] A. S. Sefat, A. Huq, M. A. McGuire, R. Jin, B. C. Sales, D. Mandrus, L. M. D. Cranswick, P. W. Stephens, and K. H. Stone, Phys. Rev. B **78**, 104505 (2008).

[5] S. Matsuishi, Y. Inoue, T. Nomura, H. Yanagi, M. Hirano, and H. Hosono, J. Am. Chem. Soc. **130**, 14428 (2008).

[6] A. Leithe-Jasper, W. Schnelle, C. Geibel, and H. Rosner, Phys. Rev. Lett. **101**, 207004 (2008).

[7] S. R. Saha, N. P. Butch, K. Kirshenbaum, and J. Paglione, Phys. Rev. B **79**, 224519 (2009).

[8] Y. Mizuguchi, F. Tomioka, S. Tsuda, T. Yamaguchi, and Y. Takano, J. Phys. Soc. Jpn. **78**, 074712 (2009).

[9] H. Kotegawa, Y. Hara, S. Masaki, H. Tou, Y. Mizuguchi, and Y. Takano, Phys. C (Amsterdam, Neth.) **470**, S426 (2010).

[10] Y. Yu, C. J. Zhang, W. Tong, L. Zhang, D. Tan, L. Pi, Z. R. Yang, M. L. Tian, S. Tan, and Y. H. Zhang, New J. Phys. **14**, 023032 (2012).

[11] M. T. Li, Z. J. Feng, H. L. Yu, D. M. Deng, B. J. Kang, S. X. Cao, and J. C. Zhang, J. Magn. Magn. Mater. **324**, 3058 (2012).

[12] D. Tan, C. Zhang, C. Xi, L. Ling, L. Zhang, W. Tong, Y. Yu, G. Feng, H. Yu, L. Pi, Z. Yang, S. Tan, and Y. Zhang, Phys. Rev. B **84**, 014502 (2011).

[13] T. Qian, X.-P. Wang, W.-C. Jin, P. Zhang, P. Richard, G. Xu, X. Dai, Z. Fang, J.-G. Guo, X.-L. Chen, and H. Ding, Phys. Rev. Lett. **106**, 187001 (2011).

[14] Z. Wang, Y. J. Song, H. L. Shi, Z. W. Wang, Z. Chen, H. F. Tian, G. F. Chen, J. G. Guo, H. X. Yang, and J. Q. Li, Phys. Rev. B **83**, 140505(R) (2011).

[15] Y. Zhang, L. X. Yang, M. Xu, Z. R. Ye, F. Chen, C. He, H. C. Xu, J. Jiang, B. P. Xie, J. J. Ying, X. F. Wang, X. H. Chen, J. P. Hu, M. Matsunami, S. Kimura, and D. L. Feng, Nat. Mater. **10**, 273 (2011).

[16] W. Li, H. Ding, P. Deng, K. Chang, C. Song, K. He, L. Wang, X. Ma, J.-P. Hu, X. Chen, and Q.-K. Xue, Nat. Phys. **8**, 126 (2012).

[17] X. Ding, D.g Fang, Z. Wang, H. Yang, J. Liu, Q. Deng, G. Ma, C. Meng, Y. Hu, and H.-H. Wen, Nat. Commun. **4**, 1897 (2013).

[18] W. Bao, Q. Z. Huang, G. F. Chen, M. A. Green, D. M. Wang, J. B. He, and Y. M. Qiu, Chin. Phys. Lett. **28**, 086104 (2011).

[19] Z. P. Yin, K. Haule, and G. Kotliar, Nat. Mater. **10**, 932 (2011).

[20] P. Dai, J. Hu, and E. Dagotto, Nat. Phys. **8**, 709 (2012).

[21] H. Lei, M. Abeykoon, E. S. Bozin, K. Wang, J. B. Warren, and C. Petrovic, Phys. Rev. Lett. **107**, 137002 (2011).

[22] A. P. Hammersley, S. O. Svenson, M. Hanfland, and D. Hauserman, High Pressure Res. **14**, 235 (1996).

[23] A. C. Larson and R. B. Von Dreele, Los Alamos National Laboratory, Report No. LAUR 86-748, 1994 (unpublished).

[24] B. H. Toby, J. Appl. Crystallogr. **34**, 210 (2001).

[25] H. Lei, M. Abeykoon, E. S. Bozin, and C. Petrovic, Phys. Rev. B **83**, 180503(R) (2011).

[26] D. M. Wang, J. B. He, T.-L. Xia, and G. F. Chen, Phys. Rev. B **83**, 132502 (2011).

[27] H. Ryu, M. Abeykoon, K. Wang, H. Lei, N. Lazarevic, J. B. Warren, E. S. Bozin, Z. V. Popovic, and C. Petrovic, Phys. Rev. B **91**, 184503 (2015).

[28] H. Lei, E. S. Bozin, K. Wang, and C. Petrovic, Phys. Rev. B **84**, 060506(R) (2011).

[29] G. Huan and M. Greenblatt, J. Less Common Met. **156**, 247 (1989).

[30] J. A. Mydosh, *Spin Glasses: An Experimental Introduction* (Taylor and Francis, London, 1993).

[31] I. A. Campbell, Phys. Rev. B **37**, 9800 (1988).

[32] D. Chu, G. G. Kenning, and R. Orbach, Phys. Rev. Lett. **72**, 3270 (1994).

[33] N. Lazarevic, M. Abeykoon, P. W. Stephens, H. Lei, E. S. Bozin, C. Petrovic, and Z. V. Popovic, Phys. Rev. B **86**, 054503 (2012).

[34] N. Lazarević, M. Radonjić, M. Šćepanović, H. Lei, D. Tanasković, C. Petrovic, and Z. V. Popović, Phys. Rev. B **87**, 144305 (2013).

[35] N. Lazarević, H. Lei, C. Petrovic, and Z. V. Popović, Phys. Rev. B **84**, 214305 (2011).

[36] Y. Texier, J. Deisenhofer, V. Tsurkan, A. Loidl, D. S. Inosov, G. Friemel, and J. Bobroff, Phys. Rev. Lett. **108**, 237002 (2012).

[37] A. Charnukha, A. Cvitkovic, T. Prokscha, D. Pröpper, N. Ocelic, A. Suter, Z. Salman, E. Morenzoni, J. Deisenhofer, V. Tsurkan, A. Loidl, B. Keimer, and A. V. Boris, Phys. Rev. Lett. **109**, 017003 (2012).

[38] Y. J. Yan, M. Zhang, A. F. Wang, J. J. Ying, Z. Y. Li, W. Qin, X. G. Luo, J. Q. Li, J. Hu, and X. H. Chen, Sci. Rep. **2**, 212 (2012).

[39] S. Mukherjee, M. N. Gastiasoro, P. J. Hirschfeld, and B. M. Andersen, Phys. Rev. B **88**, 014519 (2013).

[40] M. Yi, D. H. Lu, R. Yu, S. C. Riggs, J.-H. Chu, B. Lv, Z. K. Liu, M. Lu, Y.-T. Cui, M. Hashimoto, S.-K. Mo, Z. Hussain, C. W. Chu, I. R. Fisher, Q. Si, and Z.-X. Shen, Phys. Rev. Lett. **110**, 067003 (2013).

[41] R. Yu and Q. Si, Phys. Rev. Lett. **110**, 146402 (2013).

[42] R. Yu, J.-X. Zhu, and Q. Si, Phys. Rev. Lett. **106**, 186401 (2011).

[43] T. Berlijn, P. J. Hirschfeld, and W. Ku, Phys. Rev. Lett. **109**, 147003 (2012).

[44] L. Craco, M. S. Laad, and S. Leoni, Phys. Rev. B **84**, 224520 (2011).

[45] F. Lu, J. Z. Zhao, and W. H. Wang, J. Phys. Condens. Matter **24**, 495501 (2012).

Raman spectroscopy of $K_x Co_{2-y} Se_2$ single crystals near the ferromagnet–paramagnet transition

You may also be interested in:

Evidence of superconductivity-induced phonon spectra renormalization in alkali-doped iron selenides
M Opai, N Lazarevi, M Šepanovi et al.

Effect of ferromagnetic ordering on phonons in KCo2Se2
Urszula D Wdowik, Grzegorz Jago and Przemysaw Piekarz

Superconductivity in alkali metal intercalated iron selenides
A Krzton-Maziopa, V Svitlyk, E Pomjakushina et al.

Raman scattering in superconducting NdO1xFxBiS2 crystals
Yong Tian, Anmin Zhang, Kai Liu et al.

An overview of the Fe-chalcogenide superconductors
M K Wu, P M Wu, Y C Wen et al.

Temperature dependent phonon frequency shift and structural stability of free-standing graphene: a spectral energy density analysis
P Anees, M C Valsakumar and B K Panigrahi

Electron—phonon coupling in cuprate and iron-based superconductors revealed by Raman scattering
Zhang An-Min and Zhang Qing-Ming

Raman spectroscopy of $K_xCo_{2-y}Se_2$ single crystals near the ferromagnet–paramagnet transition

M Opačić[1], **N Lazarević**[1], **M M Radonjić**[2,3], **M Šćepanović**[1], **Hyejin Ryu**[4,5,6], **Aifeng Wang**[4], **D Tanasković**[3], **C Petrovic**[4,5] **and Z V Popović**[1]

[1] Center for Solid State Physics and New Materials, Institute of Physics Belgrade, University of Belgrade, Pregrevica 118, 11080 Belgrade, Serbia
[2] Center for Electronic Correlations and Magnetism, Theoretical Physics III, Institute of Physics, University of Augsburg, D-86135 Augsburg, Germany
[3] Scientific Computing Laboratory, Institute of Physics Belgrade, University of Belgrade, Pregrevica 118, 11080 Belgrade, Serbia
[4] Condensed Matter Physics and Materials Science Department, Brookhaven National Laboratory, Upton, NY 11973-5000, USA
[5] Department of Physics and Astronomy, Stony Brook University, Stony Brook, NY 11794-3800, USA

E-mail: nenad.lazarevic@ipb.ac.rs

Abstract

Polarized Raman scattering spectra of the $K_xCo_{2-y}Se_2$ single crystals reveal the presence of two phonon modes, assigned as of the A_{1g} and B_{1g} symmetry. The absence of additional modes excludes the possibility of vacancy ordering, unlike in $K_xFe_{2-y}Se_2$. The ferromagnetic (FM) phase transition at $T_c \approx 74$ K leaves a clear fingerprint on the temperature dependence of the Raman mode energy and linewidth. For $T > T_c$ the temperature dependence looks conventional, driven by the thermal expansion and anharmonicity. The Raman modes are rather broad due to the electron–phonon coupling increased by the disorder and spin fluctuation effects. In the FM phase the phonon frequency of both modes increases, while an opposite trend is seen in their linewidth: the A_{1g} mode narrows in the FM phase, whereas the B_{1g} mode broadens. We argue that the large asymmetry and anomalous frequency shift of the B_{1g} mode is due to the coupling of spin fluctuations and vibration. Our density functional theory (DFT) calculations for the phonon frequencies agree rather well with the Raman measurements, with some discrepancy being expected since the DFT calculations neglect the spin fluctuations.

Keywords: Raman spectroscopy, electron–phonon, lattice dynamics

(Some figures may appear in colour only in the online journal)

1. Introduction

In the last few years considerable attention was focused on the iron-based superconductors in an effort to gain deeper insight into their physical properties and to determine the origin of high-T_c superconductivity [1–4]. Discovery of superconductivity in alkali-doped iron chalcogenides, together with its uniqueness among the iron based superconductors, challenged the physical picture of the superconducting mechanism in iron pnictides [5]. The absence of hole pockets even suggested the possibility for the different type of pairing mechanism [6]. Another striking feature in $K_xFe_{2-y}Se_2$ was the presence of the intrinsic nano to mesoscale phase separation between an insulating phase and a metallic/superconducting phase [7–10]. The insulating phase hosts antiferromagnetically, $\sqrt{5} \times \sqrt{5}$ ordered iron vacancies, whereas the superconducting stripe-like phase is free of vacancies [7]. The theoretical study of

Huang *et al* [11] revealed that proximity effects of the two phases result in the Fermi surface deformation due to inter-layer hopping and, consequently, suppression of superconductivity. On the other hand, a large antiferromagnetic order protects the superconductivity against interlayer hopping, thus explaining relatively high T_c in $K_xFe_{2−y}Se_2$ [11]. However, the correlation between the two phases and its impact on superconductivity are still not fully understood.

Although the absolute values of resistivity are much smaller for the Ni-member of the $K_xM_{2−y}Se_2$ (M = transition metal) series than for the iron member, this material does not exhibit superconductivity down to $0.3\,K$ [12]. As opposed to $K_xFe_{2−y}Se_2$, vacancy ordering has not been observed in the $K_xNi_{2−y}Se_2$ single crystal [13]. These materials, together with the Co- and Ni-doped $K_xFe_{2−y}Se_2$ single crystals, have very rich structural, magnetic and transport phase diagrams. This opens a possibility for fine tuning of their physical properties by varying the sample composition [14, 15]. First results obtained on $K_xCo_{2−y}Se_2$ single crystal revealed the ferromagnetic ordering below $T_c \sim 74\,K$, as well as the absence of the superconducting phase [16].

Raman spectroscopy is a valuable tool not only for measuring vibrational spectra, but it also helps in the analysis of structural, electronic and magnetic properties, and phase transitions. There are several recent studies of the influence of the antiferromagnetic order, [17, 18] ferromagnetism, [19, 20] and magnetic fluctuations [21] on the Raman spectra.

In this paper the Raman scattering study of the $K_xCo_{2−y}Se_2$ single crystal ($x = 0.3$, $y = 0.1$), together with the lattice dynamics calculations of KCo_2Se_2, is presented. The polarized Raman scattering measurements were performed in the temperature range from $20\,K$ up to $300\,K$. The observation of only two Raman active modes when measuring from the $(0\,0\,1)$-oriented samples suggests that the $K_xCo_{2−y}Se_2$ single crystal has no ordered vacancies. The temperature dependence of the energy and linewidth of the observed Raman modes reveals a clear fingerprint of the phase transition. A large linewidth of the B_{1g} mode and its Fano line shape indicate the importance of spin fluctuations.

The rest of the manuscript is organized as follows. Section 2 contains a brief description of the experimental and numerical methods, section 3 are the results, and section 4 contains a discussion of the phonon frequencies and linewidths and their temperature dependencies. Section 5 summarizes the results.

2. Experiment and numerical method

Single crystals of $K_xCo_{2−y}Se_2$ were grown by the self-flux method, as described in [12]. The elemental analysis was performed using energy-dispersive x-ray spectroscopy (EDX) in a JEOL JSM-6500 scanning electron microscope. Raman scattering measurements were performed on freshly cleaved $(0\,0\,1)$-oriented samples with size up to $3 \times 3 \times 1\ mm^3$, using a TriVista 557 Raman system equipped with a nitrogen-cooled CCD detector, in a backscattering micro-Raman configuration. The 514.5 nm line of an Ar^+/Kr^+ ion gas laser was used as an excitation source. A microscope objective with $50 \times$ magnification was used for focusing the laser beam. All
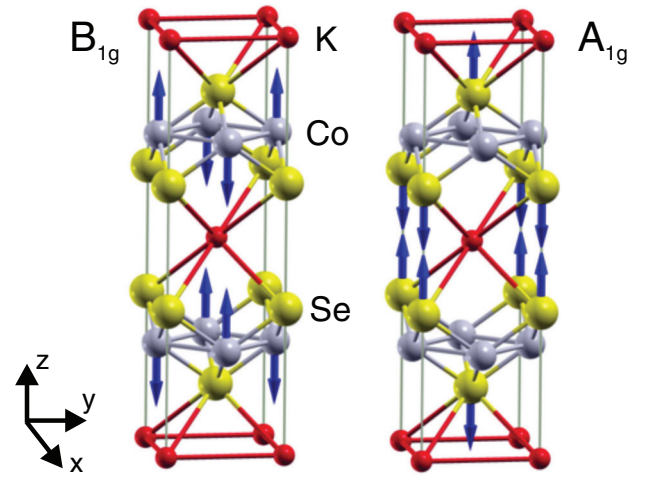

Figure 1. Unit cell of KCo_2Se_2 single crystal, together with the displacement patterns of the A_{1g} and B_{1g} Raman modes.

measurements were carried out at low laser power, in order to minimize local heating of the sample. Low temperature measurements were performed using KONTI CryoVac continuous flow cryostat with 0.5 mm thick window. Spectra were corrected for the Bose factor.

The electronic structure of the ferromagnetic (FM) and paramagnetic (PM) phases is calculated within the density functional theory (DFT), and the phonon frequencies at the Γ-point are obtained within the density functional perturbation theory (DFPT) [22]. All calculations are performed using the QUANTUM ESPRESSO package [23]. We have used projector augmented-wave (PAW) pseudo-potentials with Perdew–Burke–Ernzerhof (PBE) exchange-correlation functional with nonlinear core correction and Gaussian smearing of 0.005 Ry. The electron wave-function and the density energy cutoffs are 40 Ry and 500 Ry, respectively. The Brillouin zone is sampled with a $16 \times 16 \times 8$ Monkhorst–Pack k-space mesh. The phonon frequencies were calculated with relaxed unit cell parameters and, for comparison, with the unit cell size taken from the experiments and the relaxed positions of only Se atoms. The forces acting on individual atoms in the relaxed configuration were smaller than $10^{−4}$ Ry/a.u. and the pressure smaller than 0.5 kbar.

3. Results

KCo_2Se_2 crystallizes in the tetragonal crystal structure of $ThCr_2Si_2$-type, $I4/mmm$ space group, which is shown in figure 1. The experimental values of the unit cell parameters are $a = 3.864(2)$ Å and $c = 13.698(2)$ Å [24]. The potassium atoms are at $2a$: $(0, 0, 0)$, Co atoms at $4d$: $(0, \frac{1}{2}, \frac{1}{4})$, and Se atoms at $4e$: $(0, 0, z)$ Wyckoff positions, with the experimental value $z = 0.347$.

The KCo_2Se_2 single crystal consists of alternatively stacked K ions and CoSe layers, isostructural to the KFe_2Se_2 [25]. Factor group analysis for the $I4/mmm$ space group yields a normal mode distribution at the Brillouin-zone center, which is shown in table 1. According to the selection rules, when measuring from the $(0\,0\,1)$-plane of the sample, only two

Table 1. Atomic types with their Wyckoff positions and the contribution of each site to the Γ-point phonons, the Raman tensors and the selection rules for the $K_xCo_{2-y}Se_2$ single crystal (*I4/mmm* space group).

Atoms	Wyckoff positions	Irreducible representations
K	2a	$A_{2u} + E_u$
Co	4d	$A_{2u} + B_{1g} + E_g + E_u$
Se	4e	$A_{1g} + A_{2u} + E_g + E_u$

Raman tensors

$$\hat{R}_{A_{1g}} = \begin{pmatrix} |a|\exp i\varphi_a & 0 & 0 \\ 0 & |a|\exp i\varphi_a & 0 \\ 0 & 0 & |b|\exp i\varphi_b \end{pmatrix} \qquad \hat{R}_{B_{1g}} = \begin{pmatrix} |c|\exp i\varphi_c & 0 & 0 \\ 0 & -|c|\exp i\varphi_c & 0 \\ 0 & 0 & 0 \end{pmatrix}$$

$$\hat{R}_{E_g} = \begin{pmatrix} 0 & 0 & |e|\exp i\varphi_e \\ 0 & 0 & 0 \\ |e|\exp i\varphi_e & 0 & 0 \end{pmatrix} \qquad \hat{R}_{E_g} = \begin{pmatrix} 0 & 0 & 0 \\ 0 & 0 & |f|\exp i\varphi_f \\ 0 & |f|\exp i\varphi_f & 0 \end{pmatrix}$$

Activity and selection rules

$$\Gamma_{\text{Raman}} = A_{1g}(\alpha_{xx+yy}, \alpha_{zz}) + B_{1g}(\alpha_{xx-yy}) + 2E_g(\alpha_{xz}, \alpha_{yz})$$

$$\Gamma_{IR} = 2A_{2u}(\mathbf{E}\|\mathbf{z}) + 2E_u(\mathbf{E}\|\mathbf{x}, \mathbf{E}\|\mathbf{y})$$

$$\Gamma_{\text{acoustic}} = A_u + E_u$$

modes (A_{1g} and B_{1g}) are expected to be observed in the Raman scattering experiment. Displacement patterns of the experimentally observable Raman modes are illustrated in figure 1. The A_{1g} (B_{1g}) mode represents the vibrations of the Se (Co) ions along the c-axis, whereas the E_g modes (which are not observable for our scattering configuration) involve the vibration of both Co and Se ions within the (0 0 1)-plane.

Figure 2 shows polarized Raman scattering spectra of the $K_xCo_{2-y}Se_2$ single crystal, measured from the (0 0 1)-plane of the sample at room temperature, in different sample orientations. Only two modes, at about 187 and 198 cm^{-1}, are observed, which is in agreement with the selection rules for (0 0 1)-oriented samples. In some iron-chalcogenide compounds, the appearance of additional Raman active modes due to the iron vacancy ordering and, consequently, symmetry lowering, has been observed [8, 26]. The absence of additional phonon modes in figure 2 suggests that in $K_xCo_{2-y}Se_2$ single crystals vacancy ordering does not occur in our samples.

Selection rules imply that the A_{1g} mode may be observed for any sample orientation, provided that the polarization vector of the incident light $\mathbf{e}_i$ is parallel to the scattered light polarization vector $\mathbf{e}_s$, whereas it vanishes if these vectors are perpendicular. On the other hand, the intensity of the B_{1g} mode strongly depends on the sample orientation ($I_{B_{1g}} \sim |c|^2\cos^2(\theta + 2\beta)$), where $\theta = \angle(\mathbf{e}_i, \mathbf{e}_s)$ and $\beta = \angle(\mathbf{e}_i, \mathbf{x})$ [8]. This implies that, in parallel polarization configuration ($\theta = 0°$), the intensity of the B_{1g} mode is maximal when the sample is oriented so that $\mathbf{e}_i\|\mathbf{x}$, gradually decreases with increasing β and finally vanishes for $\beta = 45°$. In crossed polarization configuration ($\theta = 90°$), B_{1g} mode intensity decreases from its maximal value for $\beta = 45°$ to zero, which reaches when $\beta = 0°$. From figure 2 it can be seen that the intensity of the Raman mode at about 187 cm^{-1} coincides with theoretically predicted behavior for the B_{1g} mode; thereby, this phonon mode is assigned accordingly. The phonon mode at ∼198 cm^{-1}, which is present in Raman spectra only for the parallel polarization configuration ($\theta = 0°$) and whose intensity is independent on
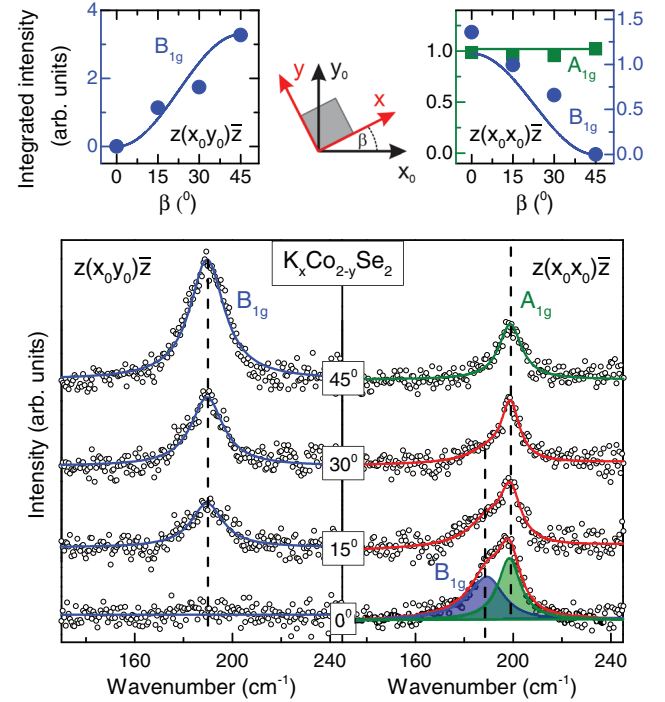
Figure 2. Upper panel: integrated intensity of the observed Raman modes as a function of the crystal orientation with respect to the laboratory axes $\mathbf{x_0}$ and $\mathbf{y_0}$. In order to estimate the intensity of the modes, phonon at 198 cm^{-1} was fitted with Lorentzian, whereas an asymmetric Raman mode appearing at 187 cm^{-1} was fitted with Fano line shape. Lower panel: Raman scattering spectra of $K_xCo_{2-y}Se_2$ single crystal measured at room temperature, in various sample orientations ($\mathbf{x} = (1\,0\,0)$, $\mathbf{y} = (0\,1\,0)$).

the sample orientation, can be assigned as the A_{1g} mode. The intensity ratio of the two Raman modes can be obtained from the spectrum measured in ($\theta = 0°$, $\beta = 0°$) scattering geometry as $I_{B_{1g}}/I_{A_{1g}} \approx 1.38$. Having in mind that the A_{1g} mode intensity is given by [8] $I_{A_{1g}} \sim |a|^2\cos^2\theta$, the ratio of the appropriate Raman tensor components can be estimated as $|c|/|a| \approx 1.17$.

Table 2. Optimized lattice constants and internal coordinate z_{Se} in the FM and PM solution.

	a (Å)	c (Å)	z_{Se}
FM^{rel}	3.893	13.269	0.350
PM^{rel}	3.766	13.851	0.368
FM^{fixed}	3.864	13.698	0.3486
PM^{fixed}	3.864	13.698	0.3496
Exper.	3.864	13.698	0.347

Note: The next two rows give the relaxed z_{Se} when the unit cell size is taken from the experiment, and the last row contains the atomic positions from the experiment [24].

The experimentally determined frequencies are compared with those obtained with DFT numerical calculations. The experimental lattice constants [24] are shown in table 2, together with their values from the DFT calculation which relaxes or keeps fixed the unit cell size. The DFPT phonon frequencies obtained using the fully relaxed atomic positions in both FM and PM phases are given in table 3, with the corresponding values obtained with the fixed unit cell size and relaxed only fractional coordinate z_{Se} given in the parenthesis. The equilibrium atomic positions in the FM solution are given by $a = 3.893$ Å, $c = 13.269$ Å, and $z_{Se} = 0.350$. The corresponding phonon frequencies are 199.5 cm^{-1} for A_{1g} mode and 171.2 cm^{-1} for B_{1g} mode. When we enforce the PM solution, we obtain $a = 3.766$ Å, $c = 13.851$ Å, and $z_{Se} = 0.368$, and 212.6 cm^{-1}, 176.6 cm^{-1} for the frequencies of the A_{1g} and B_{1g} mode, respectively. These values agree rather well with the experimental data, and agree with recently published numerical results [27][7]. They can be used to confirm the experimental assignment of the modes, but cannot resolve subtle changes of the phonon frequencies near the FM–PM transition. This level of discrepancy is expected for metallic materials with magnetic ordering since the DFT calculations neglect spin fluctuations, as discussed in some detail in the next section (see also [21]). A rather large difference between the calculated frequencies in the two phases is due to the relatively large change in the unit cell size. This difference between the unit cell sizes in the FM and PM phases is overestimated in the calculation which neglects spin fluctuations. For comparison, we also calculated the frequencies keeping the experimental values of the unit cell size, and relaxing just the coordinate z_{Se} of the Se atoms, which is often done in the case of iron based superconductors and related compounds [21]. This gives $z_{Se} = 0.3486$ in the FM solution and $z_{Se} = 0.3496$ in the PM solution, while the change in the phonon frequencies between the two solutions is much smaller, see table 3 and a discussion in section 4.

Polarized Raman scattering spectra of $K_xCo_{2-y}Se_2$ single crystals, measured at various temperatures from the $(0\,0\,1)$-plane of the sample, are presented in figure 3. The orientation of the sample is chosen so that each of the observable modes appears in a different polarization configuration. A pronounced feature in the spectra is an asymmetric Fano profile of the B_{1g} mode, persisting down to low temperatures, as well as its large linewidth compared to isostructural $K_xFe_{2-y}Se_2$ [8, 28]. This feature should by mainly due to the spin

fluctuations influencing the B_{1g} vibrational mode which modulates the distances between the magnetic Co atoms. A detailed discussion of the frequency and linewidth temperature dependence is given in the next section.

4. Discussion

There are several factors that affect the phonon frequencies (energies) and linewidths, and their changes across the FM–PM transition. In general, the temperature dependence of the phonon frequency of the mode i, $\omega_i(T)$, is influenced by thermal expansion and magnetostriction, anharmonicity effects, electron–phonon and magnetic exchange interaction (spin-phonon coupling) [29, 30]

$$\omega_i(T) - \omega_i(T_0) = \Delta\omega_i(T) = (\Delta\omega_i)_{latt} + (\Delta\omega_i)_{anh} \\ + (\Delta\omega_i)_{el-ph} + (\Delta\omega_i)_{sp-ph}. \quad (1)$$

The first term is the frequency shift due to the change of the unit cell size caused by the thermal effects and magnetostriction. $(\Delta\omega_i)_{anh}$ is the anharmonic frequency shift. $(\Delta\omega_i)_{el-ph}$ appears due to the change in the electron–phonon interaction primarily influenced by changes in the electronic spectrum near the Fermi level, and $(\Delta\omega_i)_{sp-ph}$ is the spin-phonon contribution caused by the modulation of exchange interaction by lattice vibrations.

In our case of $K_xCo_{2-y}Se_2$, for temperatures above T_c, $\omega_i(T)$ decreases and $\Gamma_i(T)$ (full width at half-maximum, FWHM) increases with increasing temperature for A_{1g} and B_{1g} modes, similar as in the Raman spectra of many other materials. However, they show anomalous behavior near T_c, see figure 4. In the following, we analyze $\omega_i(T)$ and $\Gamma_i(T)$ more closely.

4.1. Phonon frequencies

The frequencies of the A_{1g} and B_{1g} modes change by less than 2 percent in the temperature range between 20 K and 250 K. The red solid lines in figures 4(a)–(c) represent the fits of the phonon energy temperature dependence (see below), following the frequencies of the two modes in the high-temperature PM phase. The red dotted line is the extrapolation to $T = 0$. For $T > T_c$, the temperature dependence of the frequency looks conventional for both modes: the frequency decreases with increasing temperature. This behavior is expected both due to the thermal expansion and the anharmonicity. These two effects can be standardly analyzed as follows.

The temperature dependent frequency of the vibrational mode i is given by

$$\omega_i(T) = \omega_{0,i} + \Delta_i(T), \quad (2)$$

where $\omega_{0,i}$ denotes the temperature independent term and $\Delta_i(T)$ can be decomposed as [19, 31, 32]

$$\Delta_i(T) = \Delta_i^V + \Delta_i^A. \quad (3)$$

Δ_i^V describes a change of the Raman mode energy as a consequence of the lattice thermal expansion and can be expressed with [31]

---

[7] There is typo in table 3 of [27] in the frequency of the B_{1g} mode.

Table 3. The experimental phonon energies measured at 20 K in the FM phase and the extrapolated value to 0 K from the PM phase (see the text).

Symmetry	Activity	Experiment FM (cm^{-1})	Experiment PM (cm^{-1})	Calculation FM (cm^{-1})	Calculation PM (cm^{-1})	Main atomic displacements
A_{1g}	Raman	201.9	201.3	199.5 (193.2)	212.6 (193.1)	Se(z)
B_{1g}	Raman	195.3	194.2	171.2 (172.7)	176.6 (168.1)	Co(z)
E_g^1	Raman			93.1 (100.7)	92.7 (99.0)	Co(xy), Se(xy)
E_g^2	Raman			237.9 (237.6)	257.2 (235.6)	Co(xy), Se(xy)
A_{2u}^1	IR			115.1 (99.0)	113.7 (102.9)	K(z), Se(-z)
A_{2u}^2	IR			246.7 (241.4)	250.9 (241.4)	Co(z), K(-z)
E_u^1	IR			97.9 (95.0)	100.1 (95.0)	K(xy)
E_u^2	IR			239.0 (229.7)	231.0 (229.9)	Co(xy), Se(-xy)

Note: The phonon frequencies at the Γ point are calculated with fully relaxed atomic positions. The frequencies obtained with only relaxed internal coordinate are given in parenthesis.
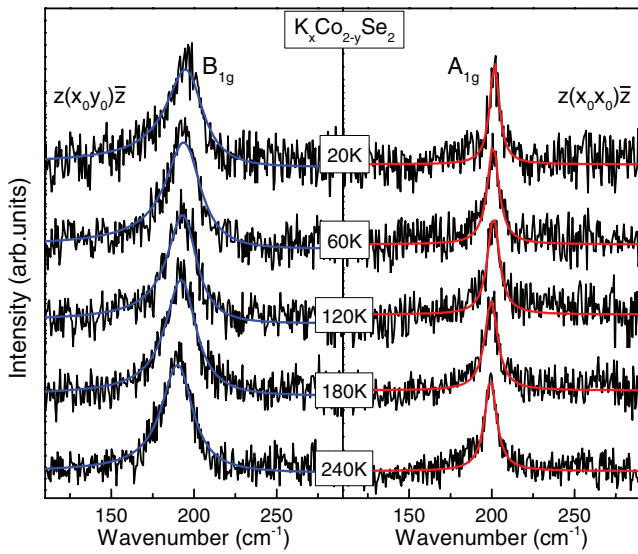

Figure 3. Temperature dependent Raman spectra of K$_x$Co$_{2-y}$Se$_2$ single crystal in parallel (left panel) and crossed (right panel) polarization configuration ($\mathbf{x_0} = \frac{1}{\sqrt{2}}(1\,1\,0), \mathbf{y_0} = \frac{1}{\sqrt{2}}(\bar{1}\,1\,0)$). The solid lines represent fits of the experimental spectra with the Lorentzian (A_{1g} mode) and the Fano profile (B_{1g} mode).

$$\Delta_i^V = \omega_{0,i}\left(e^{-3\gamma_i \int_0^T \alpha(T')dT'} - 1\right), \qquad (4)$$

where γ_i is the Grüneisen parameter of the Raman mode i and $\alpha(T)$ is the thermal expansion coefficient of a considered single crystal. Δ_i^A represents the anharmonic contribution to the Raman mode energy. If we assume, for simplicity, that anharmonic effects are described by three-phonon processes, this term is given by [31, 33]

$$\Delta_i^A = -C_i\left(1 + \frac{2\lambda_{p-p,i}}{e^{\hbar\omega_{0,i}/2k_BT} - 1}\right), \qquad (5)$$

where C is the anharmonic constant and $\lambda_{p-p,i}$ is a fitting parameter which describes the phonon–phonon coupling, including the nonsymmetric phonon decay processes.

The relative importance of the thermal expansion and anharmonicity to frequency changes is, to the best of our knowledge, not yet firmly established for pnictides and

chalcogenides. In several cases [13, 17] the anharmonic formula, equation (5), is used for the $\omega(T)$ fit. We follow here the arguments from [19, 28, 34] that $\omega(T)$ is dominated by the thermal expansion. To the best of our knowledge, the thermal expansion coefficient $\alpha(T)$ of the K$_x$Co$_{2-y}$Se$_2$ single crystal is unknown. For estimating the lattice thermal expansion contribution to the phonon energy change, the coefficient $\alpha(T)$ for FeSe, given in [35], is used. The best fit shown in our figure 4 is obtained with $\omega_{0,A_{1g}} = 201.3$ cm^{-1}, $\gamma_{A_{1g}} = 1.23$ and $\omega_{0,B_{1g}} = 194.2$ cm^{-1}, $\gamma_{B_{1g}} = 1.7$.

There exists a shift in phonon frequencies as the temperature is lowered below T_c. This shift does not show clear discontinuity (as well as the corresponding shift in the linewidths) and no additional modes are registered in the Raman spectra, which suggest that the FM–PM transition is continuous, without structural changes. There are several causes of the sudden frequency change as the sample gets magnetized. It can change due to the magnetostriction, modulation of the magnetic exchange by lattice vibrations (spin-phonon coupling), and due to the changes in the electron–phonon interaction due to spin polarization and changes in the electronic spectrum.

The effect of spin-phonon interactions, caused by the modulation of magnetic exchange interaction by lattice vibrations, may be quantitatively examined within the framework developed in [29] for insulating magnets, and recently applied also to several itinerant ferromagnets [36–39]. In this model, the shift of the Raman mode energy due to the spin-phonon interaction is proportional to the spin–spin correlation function $\langle S_i|S_j\rangle$ between nearest magnetic ions. This term should have the same temperature dependence as $(M(T)/M_0)^2$, where $M(T)$ is the magnetization per magnetic ion at a temperature T and M_0 is the saturation magnetization,

$$\Delta\omega(T) = \omega_{\text{exp}}(T) - \omega_{\text{fit}}(T) \propto \pm\left(\frac{M(T)}{M_0}\right)^2, \qquad (6)$$

where $\omega_{\text{fit}}(T)$ is the extrapolation from the high-temperature data. This model does not predict the sign of the phonon energy shift—softening or hardening. From the inset in figure 4(c) it can be seen that the B_{1g} mode energy renormalization scales well with the $(M(T)/M_0)^2$ curve. However, the effect of the
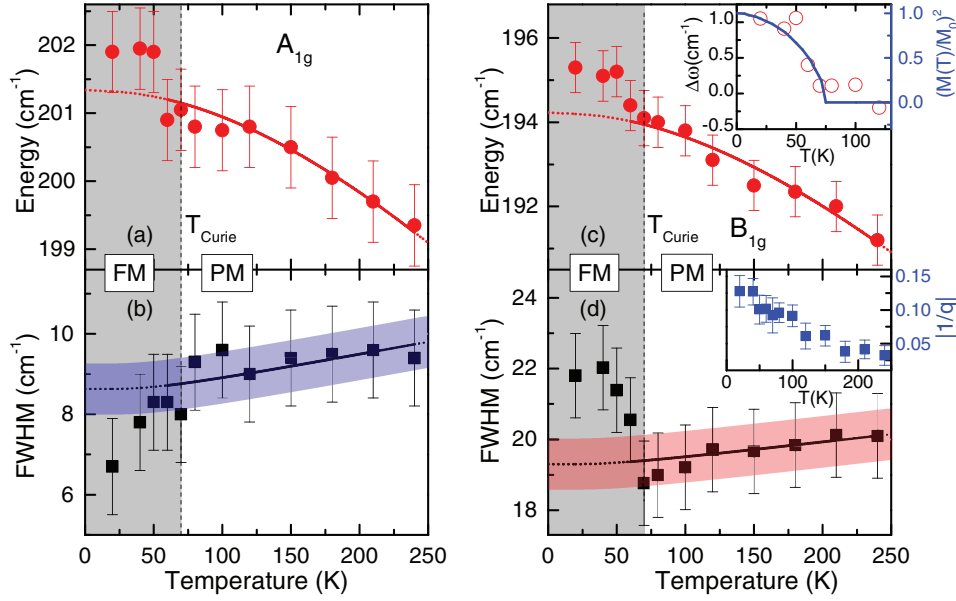
Figure 4. Temperature dependence of the energy and linewidth for the A_{1g} (a), (b) and B_{1g} (c), (d) Raman modes of the $K_xCo_{2-y}Se_2$ single crystal. Solid lines are a theoretical fit (see the text) and the dotted lines are the extrapolation to the FM phase. Upper inset: temperature dependence of the B_{1g} mode frequency, compared with the $(M(T)/M(0))^2$ curve. Lower inset: measure of the electron-mediated photon–phonon coupling ($1/q$) of the B_{1g} mode as a function of temperature.

magnetostriction (change of the unit cell size due to the magnetization) cannot be excluded based just on this plot, especially since the A_{1g} mode corresponding to the vibrations of nonmagnetic Se ions also shows a similar shift in frequency.

The DFT calculations can give us some guidance for understanding of the changes of the phonon frequencies and linewidths, but one has to be aware of its limitations. The DFT calculations (see table 2) give a rather large magnetostriction, i.e. rather large change in the size of the unit cell between the FM and PM phases (*a* changes by 3.2% and *c* by 4.3%). This leads to very large changes in the phonon frequencies, see table 3. The calculated frequencies are lower in the FM phase, as opposed to the experimental data. This already points to the limitations of the DFT calculations, which is expected near the phase transition. A similar conclusion is also present in [21]. The DFT ignores spin fluctuations which often leads to quantitative discrepancy in various physical quantities [40] and, in some cases, even predicts wrong phases. In the case of $K_xCo_{2-y}Se_2$, the DFT calculations correctly predict the FM ground state, but the calculated magnetic moment $m = 0.947\ \mu_B$ is much larger than the experimental value $m \approx 0.72\ \mu_B$ [16]. This already shows the importance of correlations and quantum fluctuations which are neglected within the DFT. Strong correlation effects can be captured using screened hybrid functional [41] or within the dynamical mean field theory combined with DFT (LDA+DMFT) [42], which is beyond our present work.

Since the magnetostriction effects are overestimated in the DFT calculations with relaxed unit cell size, we repeated the DFT (DFPT) calculations keeping the experimental value for the unit cell size and relaxing only the fractional coordinate (positions of the Se atoms). This is often done in the literature on iron based superconductors and related compounds [21]. Our calculated frequencies are given in the parenthesis

in table 3. We see that the frequency changes between the two phases are small, in better agreement with the experiment.

4.2. Phonon linewidths

The phonon linewidths of the A_{1g} and B_{1g} modes are very large, $\Gamma_{i,A_{1g}} \sim 10\ cm^{-1}$ and $\Gamma_{i,B_{1g}} \sim 20\ cm^{-1}$, which implies the importance of disorder (impurities, nonstoichiometry, lattice imperfections) in measured samples. In general, the broadening of the phonon lines can be a consequence of the electron–phonon interaction, disorder, spin fluctuations and anharmonicity effects. The temperature dependence of the linewidth in the PM phase is, however, very weak, which indicates that the anharmonicity effects are small. The DFT calculation of the linewidth is usually based on the Allen's formula, [43] $\Gamma_{q,i} = \pi N(E_F)\lambda_{q,i}\omega_{q,i}^2$. Here, $N(E_F)$ is the density of states (DOS) at the Fermi level, $\lambda_{q,i}$ is the electron–phonon coupling constant, and $\omega_{q,i}^2$ is the phonon frequency of the mode i and wavevector $\mathbf{q}$. A straightforward implementation of Allen's formula in the $\mathbf{q} \to 0$ limit corresponding to the Γ point is, however, unjustified, as explained for example in [44, 45]. In addition, structural disorder and impurities break the conservation of the momentum, which means that phonons with finite wave vectors also contribute to the Raman scattering spectra. The standard DFT calculation for the Brillouin zone averaged electron–phonon coupling constant λ gives too small value to explain the large width of the Raman lines in pnictides and chalcogenides, [33] and several other metallic systems like MgB_2 [44] and fullerides [46]. A correct estimate of the phonon linewidth can be obtained only by explicitly taking into account the disorder and electron scattering which enhances the electron–phonon interaction, [44, 46] which is beyond the standard DFT approach and scope of the present work.

The Raman mode linewidth is not directly affected by the lattice thermal expansion. Assuming that the three-phonon processes represent the leading temperature dependent term in the paramagnetic phase, full width at half-maximum, $\Gamma_i(T)$, is given by

$$\Gamma_i(T) = \Gamma_{0,i}\left(1 + \frac{2\lambda_{p-p,i}}{e^{\hbar\omega_{0,i}/2k_BT} - 1}\right) + A_i. \quad (7)$$

The first term represents the anharmonicity induced effects, where $\Gamma_{0,i}$ is the anharmonic constant. The second term A_i includes the contributions from other scattering channels, i.e. structural disorder and/or coupling of phonons with other elementary excitations, like particle-hole and spin excitations. These effects, typically, depend very weakly on temperature, but can become important near the phase transition. The best fit parameters are $\lambda_{p-p,i} = 0.2$ for both modes, $A_{A_{1g}} = 6.6$ cm^{-1} and $A_{B_{1g}} = 17.3$ cm^{-1}. The value $\Gamma_{0,i} = 2$ cm^{-1} is adopted from [28] for related compound K$_x$Fe$_{2-y}$Se$_2$, where the anharmonic effects dominate the temperature dependence. We see that $\lambda_{p-p,i}$ assumes values much smaller than 1. Small and sometimes irregular changes in $\Gamma_i(T)$ are also observed in other materials whose Raman spectra are considered to be dominated by spin fluctuations [21, 33]. Therefore, we believe that a simple separation of $\Gamma_i(T)$ to the anharmonic and temperature independent term, which works well in many systems, is not appropriate for itinerant magnetic systems like K$_x$Co$_{2-y}$Se$_2$. We conclude that the spin fluctuations and electron–phonon coupling are likely to affect the linewidth even above T_c.

The electron–phonon interaction strength is proportional to the density of states at the Fermi level $N(E_F)$. Our DFT calculations for the DOS agree with those in [47]. The calculated DOS in the FM phase, $N(E_F) = 3.69$ eV^{-1}, is smaller than, $N(E_F) = 5.96$ eV^{-1}, in the PM phase. (Though, in reality, it is possible that the DOS significantly differs from the one given by the DFT calculations due to the spin fluctuations and disorder effects.) Therefore, one expects that the phonon line is narrower in the FM phase than in the PM phase. This is indeed the case for the A_{1g} mode, but the opposite is observed for the B_{1g} mode.

It is also interesting to note that the B_{1g} mode is much more asymmetric than the A_{1g} mode and almost twice broader. These two observations are in striking similarity with the Raman spectra in the quasi-one-dimensional superconductor K$_2$Cr$_3$As$_3$ [21]. In this material the vibrational mode that modulates the distance between the magnetic Cr atoms also features large asymmetry and linewidth. In our case, the distances between the magnetic Co ions are modulated by the vibrations of the B_{1g} mode, see figure 1. This leads us to the conclusion that the anomalous features of the B_{1g} mode are the consequence of spin fluctuations coupled to the electronic structure via lattice vibrations (in addition to the magnetostriction and spin polarization, which change the electronic spectrum near the Fermi level and, therefore, affect the electron–phonon interaction for both modes). It should be noted that similar anomalous properties of B_{1g} phonon were experimentally observed in the cuprate high-temperature superconductor YBa$_2$Cu$_3$O$_7$ [48, 49], and

explained as a consequence of the out-of-phase nature of this mode which couples to oxygen-oxygen in-plane charge fluctuations [50–52]. In the case of iron-based superconductors and related compounds, the chalcogen atoms and Fe (or Co) are not in the same plane and phonons of A_{1g} symmetry can also directly couple with the electrons. A satisfactory agreement of theory and Raman experiments remains to be established [53].

The asymmetric B_{1g} phonon line can be described by the Fano profile [21, 36, 54, 55]

$$I(\omega) = I_0\frac{(\epsilon + q)^2}{1 + \epsilon^2}, \quad (8)$$

where $\epsilon = 2(\omega - \omega_0)/\Gamma$, ω_0 is the bare phonon frequency, Γ is the linewidth. I_0 is a constant and q is the Fano asymmetry parameter. It serves as a measure of a strength of the electron–phonon coupling: an increase in $|1/q|$ indicates an increase in the electron–phonon interaction, more precisely, an increase in the electron-mediated photon–phonon coupling function [51, 53]. From the inset of figure 4(d) it can be seen that $|1/q|$ increases as the temperature is lowered and reaches the highest values around T_c, when the spin fluctuations are the strongest. Spin fluctuations increase the electron–phonon scattering, similarly does the disorder. Technically, the electronic Green function acquires an imaginary component of the self energy due to the spin fluctuations, and this implies the increase in the damping term in the phonon self-energy, as explained in, e.g. [44]. This leads us to conclude that the spin fluctuations strongly enhance the electron–phonon interaction for the B_{1g} vibrational mode affecting its frequency and linewidth near T_c.

5. Conclusion

In summary, the Raman scattering study of the K$_x$Co$_{2-y}$Se$_2$ ($x = 0.3, y = 0.1$) single crystals and lattice dynamics calculations of the KCo$_2$Se$_2$, have been presented. Two out of four Raman active phonons are experimentally observed and assigned. The lack of any additional modes indicates the absence of vacancy ordering. The Raman spectra show sudden changes in the phonon energy and linewidth near the FM–PM phase transition. Above T_c the energy and linewidth temperature dependence of the A_{1g} and B_{1g} modes look conventional, as expected from the thermal expansion and anharmonicity effects. The linewidth, though, has very weak temperature dependence even above T_c which may be the consequence of the proximity of the phase transition and spin fluctuations. The B_{1g} vibrational mode has particularly large linewidth and features a Fano profile, which is likely the consequence of the magnetic exchange coupled to the vibrations of the Co atoms. Interestingly, the A_{1g} mode linewidth decreases below T_c, whereas the linewidth of the B_{1g} mode increases. The DFT calculations generally agree with the measured phonon frequencies. However, fine frequency differences in the two phases cannot be correctly predicted since the DFT calculations do not account for the spin fluctuation effects.

Acknowledgments

References

[1] Stewart G R 2011 *Rev. Mod. Phys.* **83** 1589–652
[2] Wei B, Qing-Zhen H, Gen-Fu C, Green M A, Du-Ming W, Jun-Bao H and Yi-Ming Q 2011 *Chin. Phys. Lett.* **28** 086104
[3] Liu R H *et al* 2011 *Europhys. Lett.* **94** 27008
[4] Ma L, Ji G F, Dai J, Lu X R, Eom M J, Kim J S, Normand B and Yu W 2012 *Phys. Rev. Lett.* **109** 197002
[5] Dagotto E 2013 *Rev. Mod. Phys.* **85** 849–67
[6] Zhang Y M *et al* 2011 *Nat. Mater.* **10** 273–7
[7] Li W *et al* 2012 *Nat. Phys.* **8** 126–30
[8] Lazarević N, Abeykoon M, Stephens P W, Lei H, Bozin E S, Petrovic C and Popović Z V 2012 *Phys. Rev.* B **86** 054503
[9] Ding X, Fang D, Wang Z, Yang H, Liu J, Deng Q, Ma G, Meng C, Hu Y and Wen H-H 2013 *Nat. Commun.* **4** 1897
[10] Louca D, Park K, Li B, Neuefeind J and Yan J 2013 *Sci. Rep.* **3** 2047
[11] Huang S-M, Mou C-Y and Lee T-K 2013 *Phys. Rev.* B **88** 174510
[12] Lei H, Abeykoon M, Wang K, Bozin E S, Ryu H, Graf D, Warren J B and Petrovic C 2014 *J. Phys.: Condens. Matter* **26** 015701
[13] Lazarević N, Radonjić M, Šćepanović M, Lei H, Tanasković D, Petrovic C and Popović Z V 2013 *Phys. Rev.* B **87** 144305
[14] Ryu H, Wang K, Opacic M, Lazarevic N, Warren J B, Popovic Z V, Bozin E S and Petrovic C 2015 *Phys. Rev.* B **92** 174522
[15] Ryu H, Abeykoon M, Wang K, Lei H, Lazarevic N, Warren J B, Bozin E S, Popovic Z V and Petrovic C 2015 *Phys. Rev.* B **91** 184503
[16] Yang J, Chen B, Wang H, Mao Q, Imai M, Yoshimura K and Fang M 2013 *Phys. Rev.* B **88** 064406
[17] Um Y J *et al* 2012 *Phys. Rev.* B **85** 064519
[18] Popović Z V, Lazarević N, Bogdanović S, Radonjić M M, Tanasković D, Hu R, Lei H and Petrovic C 2014 *Solid State Commun.* **193** 51–5
[19] Eiter H-M, Jaschke P, Hackl R, Bauer A, Gangl M and Pfleiderer C 2014 *Phys. Rev.* B **90** 024411
[20] Kirillov D, Suzuki Y, Antognazza L, Char K, Bozovic I and Geballe T H 1995 *Phys. Rev.* B **51** 12825–8
[21] Zhang W-L, Li H, Xia D, Liu H W, Shi Y-G, Luo J L, Hu J, Richard P and Ding H 2015 *Phys. Rev.* B **92** 060502
[22] Baroni S, de Gironcoli S, Dal Corso A and Giannozzi P 2001 *Rev. Mod. Phys.* **73** 515–62
[23] Gianozzi P *et al* 2009 *J. Phys.: Condens. Matter* **21** 395502
[24] Huan G and Greenblatt M 1989 *J. Less-Common Met.* **156** 247–57
[25] Guo J, Jin S, Wang G, Wang S, Zhu K, Zhou T, He M and Chen X 2010 *Phys. Rev.* B **82** 180520
[26] Lazarević N, Lei H, Petrovic C and Popović Z V 2011 *Phys. Rev.* B **84** 214305
[27] Wdowik U D, Jaglo G and Piekarz P 2015 *J. Phys.: Condens. Matter* **27** 415403
[28] Opačić M, Lazarević N, Šćepanović M, Ryu H, Lei H, Petrovic C and Popović Z V 2015 *J. Phys.: Condens. Matter* **27** 485701
[29] Granado E, García A, Sanjurjo J A, Rettori C, Torriani I, Prado F, Sánchez R D, Caneiro A and Oseroff S B 1999 *Phys. Rev.* B **60** 11879–82
[30] Gupta R, Sood A K, Metcalf P and Honig J M 2002 *Phys. Rev.* B **65** 104430
[31] Menéndez J and Cardona M 1984 *Phys. Rev.* B **29** 2051–9
[32] Haro E, Balkanski M, Wallis R F and Wanser K H 1986 *Phys. Rev.* B **34** 5358–67
[33] Rahlenbeck M, Sun G L, Sun D L, Lin C T, Keimer B and Ulrich C 2009 *Phys. Rev.* B **80** 064509
[34] Gnezdilov V, Pashkevich Y G, Lemmens P, Wulferding D, Shevtsova T, Gusev A, Chareev D and Vasiliev A 2013 *Phys. Rev.* B **87** 144508
[35] Böhmer A E, Hardy F, Eilers F, Ernst D, Adelmann P, Schweiss P, Wolf T and Meingast C 2013 *Phys. Rev.* B **87** 180505
[36] Kumar A, Chaudhary S, Pandya D K and Sharma S K 2014 *Phys. Rev.* B **90** 024302
[37] Iliev M N, Abrashev M V, Litvinchuk A P, Hadjiev V G, Guo H and Gupta A 2007 *Phys. Rev.* B **75** 104118
[38] Laverdière J, Jandl S, Mukhin A A, Ivanov V Y, Ivanov V G and Iliev M N 2006 *Phys. Rev.* B **73** 214301
[39] Kumar D, Kumar S and Sathe V G 2014 *Solid State Commun.* **194** 59–64
[40] Yin Z P, Haule K and Kotliar G 2011 *Nat. Mater.* **10** 932–5
[41] Yin Z P, Kutepov A and Kotliar G 2013 *Phys. Rev.* X **3** 021011
[42] Haule K, Shim J H and Kotliar G 2008 *Phys. Rev. Lett.* **100** 226402
[43] Allen P B 1972 *Phys. Rev.* B **6** 2577–9
[44] Cappelluti E 2006 *Phys. Rev.* B **73** 140505
[45] Calandra M and Mauri F 2005 *Phys. Rev.* B **71** 064501
[46] Aksenov V L and Kabanov V V 1998 *Phys. Rev.* B **57** 608–12
[47] Bannikov V V, Shein I R and Ivanovskii A L 2012 *Phys. B: Condens. Matter* **407** 271–5
[48] Ruf T, Thomsen C, Liu R and Cardona M 1988 *Phys. Rev.* B **38** 11985–7
[49] Macfarlane R M, Rosen H and Seki H 1987 *Solid State Commun.* **63** 831–4
[50] Barišić S, Kupčić I and Batistić I 1989 *Int. J. Mod. Phys.* B **03** 2051–63
[51] Devereaux T P, Virosztek A and Zawadowski A 1995 *Phys. Rev.* B **51** 505–14
[52] Kupčić I and Barišić S 2007 *Phys. Rev.* B **75** 094508
[53] García-Martínez N A, Valenzuela B, Ciuchi S, Cappelluti E, Calderón M J and Bascones E 2013 *Phys. Rev.* B **88** 165106
[54] Iliev M N, Jandl S, Popov V N, Litvinchuk A P, Cmaidalka J, Meng R L and Meen J 2005 *Phys. Rev.* B **71** 214305
[55] Lazarević N, Popović Z V, Hu R and Petrovic C 2010 *Phys. Rev.* B **81** 144302

Small influence of magnetic ordering on lattice dynamics in TaFe$_{1.25}$Te$_3$

M. Opačić,[1] N. Lazarević,[1] D. Tanasković,[2] M. M. Radonjić,[2] A. Milosavljević,[1] Yongchang Ma,[3,4]
C. Petrovic,[3] and Z. V. Popović[1,5]

[1]*Center for Solid State Physics and New Materials, Institute of Physics Belgrade, University of Belgrade, Pregrevica 118, 11080 Belgrade, Serbia*

[2]*Scientific Computing Laboratory, Center for the Study of Complex Systems, Institute of Physics Belgrade, University of Belgrade, Pregrevica 118, 11080 Belgrade, Serbia*

[3]*Condensed Matter Physics and Materials Science Department, Brookhaven National Laboratory, Upton, New York 11973-5000, USA*

[4]*School of Materials Science and Engineering, Tianjin University of Technology, Tianjin 300384, People's Republic of China*

[5]*Serbian Academy of Sciences and Arts, Knez Mihailova 35, 11000 Belgrade, Serbia*

Raman scattering spectra of zigzag spin chain TaFe$_{1.25}$Te$_3$ single crystal are presented in a temperature range from 80 to 300 K. Nine Raman active modes of A_g and B_g symmetry are clearly observed and assigned by probing different scattering channels, which is confirmed by lattice dynamics calculations. Temperature dependence of the Raman modes linewidth is mainly governed by the lattice anharmonicity. The only deviation from the conventional behavior is observed for A_g symmetry modes in a vicinity of the magnetic phase transition at $T_N \approx 200$ K. This implies that the electron-phonon interaction weakly changes with temperature and magnetic ordering, whereas small changes in the spectra near the critical temperature can be ascribed to spin fluctuations.

I. INTRODUCTION

The discovery of superconductivity in La(O$_{1-x}$F$_x$)FeAs in 2008 [1] initiated an intensive search for new iron-based superconducting materials, in order to obtain better understanding of their physical properties and the mechanism of high-T_c superconductivity [2–4]. Novel iron-based materials, however, are not only superconducting, but can also exhibit various types of magnetic ordering. In some cases the magnetic phase transition is continuous [5–8], whereas in others it is accompanied by structural changes [9–15], or even by a nanoscale coexistence of antiferromagnetic (AFM) and superconducting domains [16–18].

TaFe$_{1+y}$Te$_3$ was synthesized and characterized about 25 years ago [19,20]. It is a layered system consisting of FeTe chains, along the b axis, separated by a Ta/Te network in between; see Fig. 1. These layers are parallel to the natural cleavage plane. There are also additional Fe ions, Fe2, randomly occupying interstitial sites [21–23]. TaFe$_{1+y}$Te$_3$ features anisotropic charge transport with metallic resistivity within the plane and insulating in the direction normal to the FeTe layers [23]. The first study of magnetic structure implies that TaFe$_{1+y}$Te$_3$ is composed of double zigzag spin chains with antiferromagnetic ordering of Fe1 spins [22]. The newest neutron diffraction measurements suggest that spin ordering within zigzag chains is ferromagnetic, whereas these zigzag chains couple antiferromagnetically [23], as shown in Fig. 1(b). However, the exact interaction mechanism is not clearly resolved.

There is a similarity between TaFe$_{1+y}$Te$_3$ and the extensively studied Fe$_{1+y}$Te compound since they are correlated bad metals which order antiferromagnetically below $T_N \approx$ 200 K and 70 K, respectively [10,23], both having rather large magnetic moments on Fe ions, $\approx$2 μ_B/Fe. TaFe$_{1+y}$Te$_3$, however, forms ferromagnetic (FM) zigzag spin chains which couple antiferromagnetically between the layers, whereas the Fe spins in Fe$_{1+y}$Te form a bicollinear AFM structure. The magnetic phase transition in Fe$_{1+y}$Te is accompanied by the structural change from a tetragonal to a monoclinic, as opposed to TaFe$_{1+y}$Te$_3$ where a continuous transition to the AFM phase is observed in thermodynamic and transport measurements [22]. Just like in Fe$_{1+y}$Te, interest in spin chain and ladder materials [24] stems not only from their block-AFM states similar to parent compounds of iron-based superconductors [25], but also from superconductivity. It is worth noting that spin 1/2 copper oxide ladder structures host a spin gap and superconductivity upon doping [26–28]. In contrast to superconductivity in copper oxide ladder materials that was rather rare and with critical temperatures rather small when compared to highest achieved in copper square lattices [29,30], iron-ladder materials feature T_c's similar to the highest found in Fe-based superconductors [31].

Raman spectra provide additional information on magnetic ordering and electron-phonon coupling. There exist several Raman studies of the phonon spectra of iron based materials near the superconducting or magnetic phase transition [32,33]. While no anomalies were observed in 1111 compounds [34,35], the Raman spectra show anomalous behavior near the spin density wave (SDW) transition in some of the 122 and 11 compounds [15,36–38], which was ascribed to the phonon renormalization due to the opening of the SDW or superconducting gap, or to the structural transition. Large anomalies were observed also in ferromagnetic K$_x$Co$_{2-y}$Se$_2$ [5], which was ascribed to the effect of electron-phonon coupling and spin fluctuations. Fe$_{1+y}$Te phonon spectra feature unusually large anomalies near the magnetic phase transition, as seen in sudden changes in the phonon frequencies and linewidths, due to the phonon modulation of magnetic interactions and structural phase transition [11–13]. Therefore, it is of interest to examine lattice dynamics in the normal state of iron-spin chain and ladder materials and compare it to materials like Fe$_{1+y}$Te. To the best of our knowledge, there are no published data on lattice dynamics of TaFe$_{1+y}$Te$_3$.

In this paper we present polarized Raman scattering spectra of TaFe$_{1.25}$Te$_3$ single crystal measured in a temperature range from 80 to 300 K. Nine out of 15 Raman active modes are
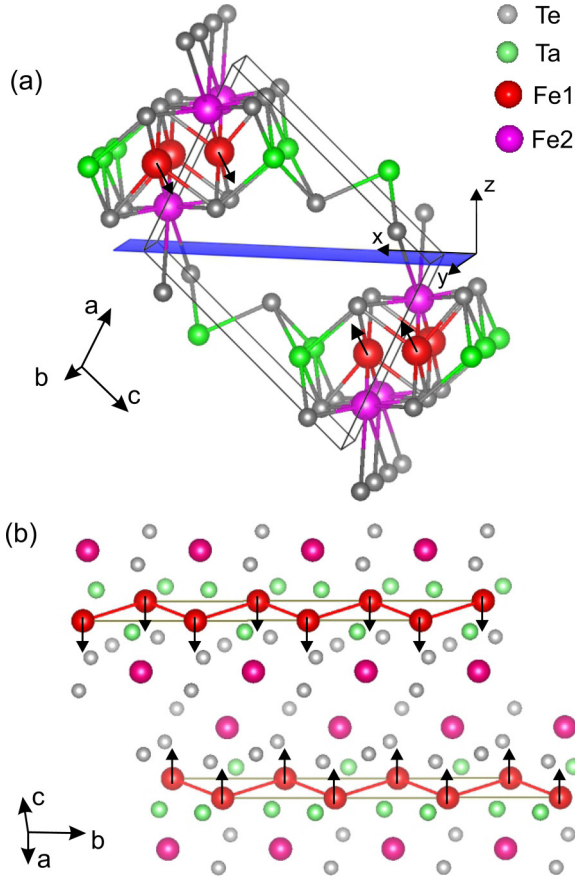
FIG. 1. (a) Structure of the $TaFe_{1.25}Te_3$ single crystal together with the natural cleavage plane $[\bar{1}01]$. $\mathbf{x} = 1/\sqrt{2}(\bar{1}0\bar{1})$ and $\mathbf{y} = (010)$ correspond to our laboratory system. (b) A view of the $TaFe_{1.25}Te_3$ structure along the *b* axis. Two neighboring chains of Fe1 spins point in a parallel direction, forming a ferromagnetic zigzag chain, whereas spins of neighboring zigzag chains order antiferromagnetically. One should note that Fe2 is present with occupancy of 0.25.

observed and assigned using the selection rules for different polarization configurations and lattice dynamics calculations. In a sharp contrast to the related FeTe compound, $TaFe_{1.25}Te_3$ Raman spectra do not show significant changes near $T_N \approx$ 200 K, which clearly indicates that the phase transition is continuous. Temperature dependence of the frequency and linewidth is conventional, driven by the anharmonicity effects, except very near T_N where some of phonon lines slightly broaden which should be the consequence of spin fluctuations near the critical temperature. These results indicate very small changes in the electron-phonon coupling and in the Fermi surface in the measured temperature range.

II. EXPERIMENT AND NUMERICAL METHOD

Single crystals were grown using the self-flux method, as described elsewhere [19]. Raman scattering measurements were performed on freshly cleaved $(\bar{1}01)$-oriented samples, using Jobin Yvon T64000 Raman system, equipped with a nitrogen-cooled CCD detector, in the backscattering micro-Raman configuration. The 532 nm line of a solid state laser was used as an excitation source. A microscope objective with

$50\times$ magnification was used for focusing the laser beam. All measurements were performed at low laser power, to reduce local heating of the sample. For low temperature measurements KONTI CryoVac continuous flow cryostat with 0.5 mm thick window was used. All spectra were corrected for the Bose factor. For extracting the data from the Raman spectra, phonon modes were fitted with a Lorentzian profile.

The electronic structure is calculated for stoichiometric $TaFeTe_3$ in the paramagnetic phase within the density functional theory (DFT), and the phonon frequencies at the Γ-point are obtained within the density functional perturbation theory (DFPT) [39], using the QUANTUM ESPRESSO package [40]. We have used projector augmented wave (PAW) pseudopotentials with Perdew-Burke-Ernzerhof (PBE) exchange-correlation functional with nonlinear core correction and Gaussian smearing of 0.01 Ry. The electron wave function and the density energy cutoffs were 64 Ry and 782 Ry, respectively. The Brillouin zone is sampled with $8 \times 8 \times 8$ Monkhorst-Pack *k*-space mesh. The phonon frequencies were calculated with the unit cell size taken from the experiments and the relaxed positions of atoms within the unit cell. The forces acting on individual atoms in the relaxed configuration were smaller than 10^{-4} Ry/a.u.

III. RESULTS AND DISCUSSION

$TaFe_{1+y}Te_3$ crystallizes in the monoclinic crystal structure, which is shown in Fig. 1. The space group is $P2_1/m$ (unique axis *b*), with two formula units per unit cell [19,20]. The experimental values of the unit cell parameters are $a = 7.436$ Å, $b = 3.638$ Å, $c = 10.008$ Å, and $\beta = 109.17°$. All atoms (including the excess Fe), are at $2e$ Wyckoff positions, with fractional coordinates given in Table I.

The factor group analysis (FGA) for $P2_1/m$ space group yields the following normal mode distribution at the Γ point:

$$\Gamma_{Raman} = 10A_g + 5B_g,$$
$$\Gamma_{IR} = 4A_u + 8B_u,$$
$$\Gamma_{acoustic} = A_u + 2B_u.$$

The Raman spectra were measured from the $(\bar{1}01)$ plane of the sample, which is the natural cleavage plane [23,42]. From the Raman tensors given in Table II, the A_g phonon modes are expected to be observable in the (xx) and (yy) scattering configurations. The B_g modes can be observed only in (xy) polarization configuration.

TABLE I. Experimental fractional coordinates of $TaFe_{1.25}Te_3$ taken from Ref. [19]. In the parentheses are the calculated values for $TaFeTe_3$.

Atom type	x	y	z
Ta	0.8340 (0.8331)	0.25	0.3007 (0.2987)
Fe1	0.6147 (0.6223)	−0.25	0.0890 (0.0988)
Fe2	0.7686	0.25	−0.0047
Te1	0.4392 (0.4326)	0.25	0.1860 (0.1637)
Te2	0.9835 (0.9842)	−0.25	0.1589 (0.1584)
Te3	0.2179 (0.2192)	0.25	0.4970 (0.5028)

TABLE II. Upper panel: atomic species (all of them are at $2e$ Wyckoff positions) and the contribution of each atom to the Γ-point phonons, the corresponding Raman tensors for the TaFeTe$_3$ single crystal ($P2_1/m$ space group) [41]. Lower panel: the calculated (for the stoichiometric TaFeTe$_3$) and experimental phonon energies at 100 K (for the TaFe$_{1.25}$Te$_3$ single crystal).

Atoms			Irreducible representations		
Ta, Fe1, Te1, Te2, Te3			$2A_g + A_u + B_g + 2B_u$		
		Raman tensors			
$\hat{R}_{A_g} = \begin{pmatrix} a & 0 & d \\ 0 & b & 0 \\ d & 0 & c \end{pmatrix}$			$\hat{R}_{B_g} = \begin{pmatrix} 0 & e & 0 \\ e & 0 & f \\ 0 & f & 0 \end{pmatrix}$		
Raman active			Infrared active		
Symmetry	Calc. (cm^{-1})	Expt. (cm^{-1})	Symmetry	Calc. (cm^{-1})	Expt. (cm^{-1})
A_g^1	36.2		A_u^1	42.8	
B_g^1	43.8		B_u^1	54.9	
B_g^2	57.9	61.6	B_u^2	94.4	
A_g^2	63.8	62.3	A_u^2	101.4	
A_g^3	75.3	68.5	B_u^3	111.3	
A_g^4	104.4	90	A_u^3	131.1	
B_g^3	105.1		B_u^4	143.2	
A_g^5	124.6		B_u^5	160.4	
B_g^4	127.2	130.4	B_u^6	188.6	
A_g^6	149.8	155	B_u^7	227.9	
A_g^7	164.9	165	A_u^4	231.1	
A_g^8	191		B_u^8	289.4	
B_g^5	217.1	222.3			
A_g^9	241.9	223.9			
A_g^{10}	276.22				

Raman scattering spectra of TaFe$_{1.25}$Te$_3$ single crystals, measured at 100 K in three different polarization configurations, are presented in Fig. 2. By using the selection rules, we assign the Raman peaks appearing in the (xx) and (yy) polarization configuration as the A_g ones. This conclusion is supported by the lattice dynamics calculations, given in Table II. By comparing the calculated values of A_g mode energies with those of the peaks appearing in the (xx) and (yy) spectra, we can unambiguously assign four Raman modes (A_g^4, A_g^6, A_g^7, and A_g^9). The broad structure around 65 cm^{-1} probably originates from the A_g^2 and A_g^3 modes, although the contribution of the A_g^1 mode (with calculated energy of 42.7 cm^{-1}) cannot be excluded. The peaks at 57.9 cm^{-1} and 130 cm^{-1} that are clearly visible in (xy) but absent in (yy) configuration are assigned as B_g^2 and B_g^4 modes, respectively. The low intensity peak at ≈ 220 cm^{-1}, that becomes clearly observable at low temperatures, is tentatively assigned as B_g^5 mode, although the contribution from the leakage of A_g^9 mode cannot be excluded. The origin of the two very broad structures at about 70 cm^{-1} and 160 cm^{-1}, which are pronounced in the (xy) configuration, is not completely clear. Aside from providing additional charge, Fe2 atoms may contribute to momentum transfer scattering, in line with the pronounced quasielastic continuum, present in all the scattering configurations. Consequently, contribution from single-phonon scattering away from Γ point becomes observable, which is theoretically predicted [43,44] and experimentally observed

[45,46]. Although we cannot exclude the possibility of two- and, in particular, double-phonon contributions, we believe it is less likely due to the nature of the processes and since they usually have more pronounced contribution to A channel (for arbitrary irreducible symmetry μ of C_{2h} holds $\mu \otimes \mu \ni A$).

The normal modes of the selected A_g and B_g vibrations, as obtained by the lattice dynamics calculations, are shown in Fig. 3. The low energy B_g^2 mode represents vibrations of Te and Ta atoms which tend to elongate the (Ta,Fe)Te tetrahedra in the xy plane. B_g^4 phonon originates mainly from Ta and Te atom vibrations in directions opposite to each other, whereas A_g^4 mode represents dominantly vibrations of another Te atom in the xy plane. A_g^7 and A_g^9 modes originate from the vibrations of Fe and Te atoms which tend to rotate the tetrahedra around the x axis.

The DFT calculations are in very good agreement with the measured Raman spectra, specially having in mind the strength of electronic correlations in iron based compounds and the presence of additional Fe2 atoms in the measured sample. We restricted to the nonmagnetic DFT calculations. This is because small changes in the phonon energies due to the magnetic ordering cannot be reliably captured since the DFT does not treat strong correlation and spin-fluctuations effects. Our DFT calculations for the electronic band structure agree with the results from Ref. [42]. The calculated electronic dispersions are in rather good agreement with the ARPES measurements [42], which indicates that the main effect of the interstitial Fe2 ion is to provide additional charge and shift
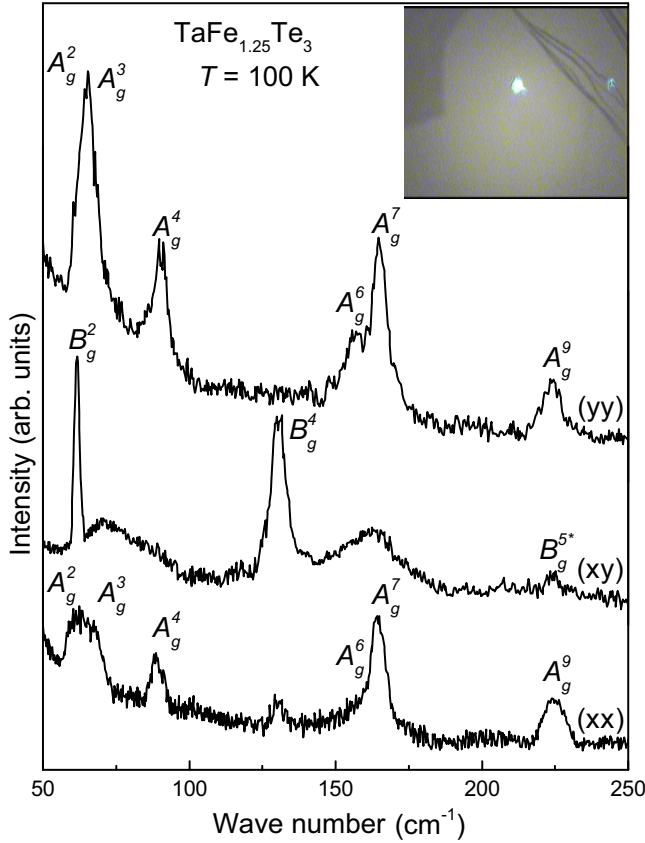
FIG. 2. Polarized Raman scattering spectra of $TaFe_{1.25}Te_3$ single crystal measured at 100 K in various polarizations. The notation in parentheses indicates the polarization directions of the incident and scattered light according to Fig. 1(a). Inset: surface of the probed $TaFe_{1.25}Te_3$ single crystal.

the Fermi level. This conclusion is supported with a small difference between the relaxed and experimental fractional coordinates; see Table I.
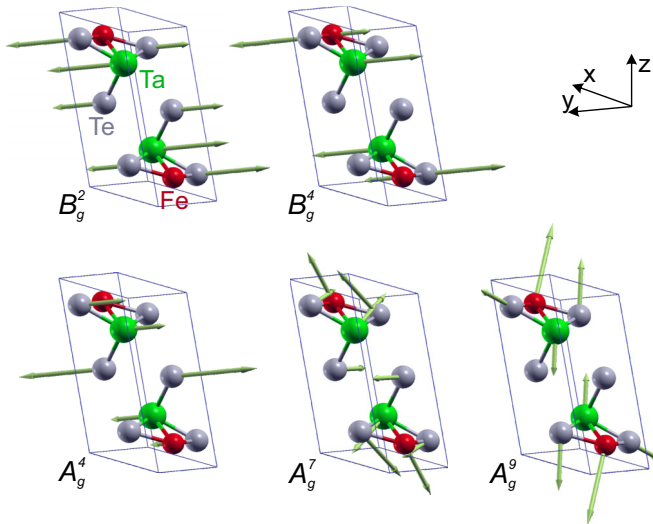

FIG. 3. Unit cell of $TaFeTe_3$ single crystal with the displacement patterns of several A_g and B_g Raman modes. Arrow lengths are proportional to the square root of the interatomic forces.
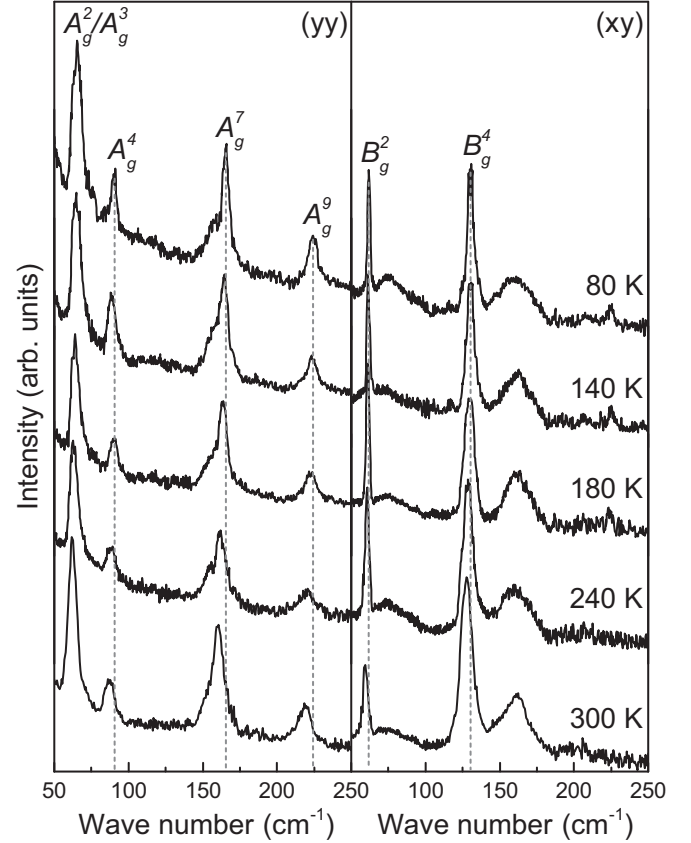
FIG. 4. Temperature dependent Raman scattering spectra of $TaFe_{1.25}Te_3$ single crystal in the (yy) (left panel) and (xy) (right panel) polarization.

In order to analyze the changes of the Raman spectra near the AFM transition at $T_N \approx 200$ K, we have performed measurements in a temperature range from 80 K up to 300 K. Raman spectra of $TaFe_{1.25}Te_3$ single crystal, measured at different temperatures in the (yy) and (xy) scattering configurations, are given in Fig. 4. In the following, we perform the temperature analysis of the energy and the linewidth for five most clearly observed modes.

The temperature dependence of the Raman mode energy is usually described with [47,48]

$$\omega_i(T) = \omega_{0,i} + \Delta_i^V(\gamma_i, \alpha_i(T)) + \Delta_i^A(C_i), \tag{1}$$

where $\omega_{0,i}$ is a temperature independent contribution to the Raman mode energy. The second term represents a change of the phonon energy induced by the lattice thermal expansion and depends on the Grüneisen parameter γ_i and the thermal expansion coefficient $\alpha_i(T)$. The term Δ_i^A describes the anharmonicity induced change of the Raman mode energy which is a function of the anharmonic constant C_i. Both Δ_i^V and Δ_i^A have qualitatively the same temperature dependence. Since there are no reported experimental data on the temperature dependence of the lattice parameters for $TaFe_{1+y}Te_3$, we didn't attempt to fit the data, and the black dotted lines in Figs. 5 and 6 are guides to the eye. The $\omega_i(T)$ curves follow the "standard" [5,15,37,49,50] continuous decrease in energy with temperature, with very small anomalies near T_N except for the A_g^4 mode.
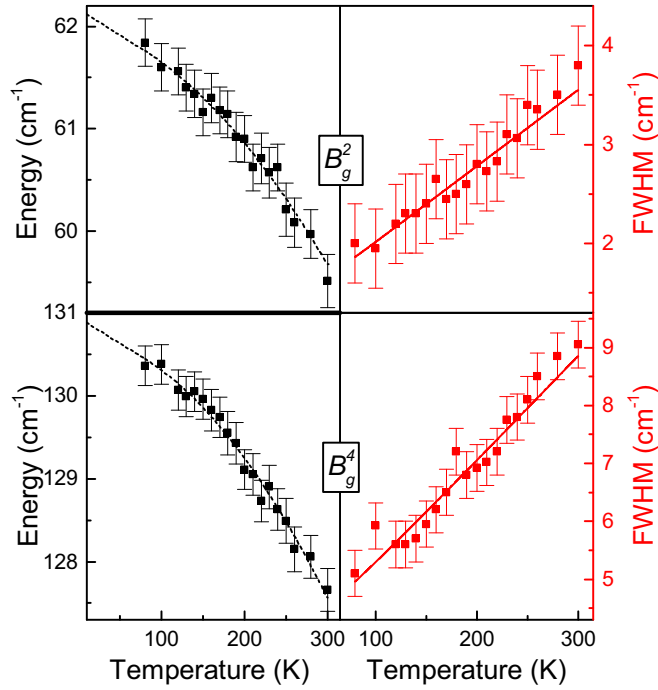
FIG. 5. Temperature dependence of the energy and linewidth for the B_g^2 and B_g^4 Raman modes of the TaFe$_{1.25}$Te$_3$ single crystal. The red lines are fitted according to Eq. (2), whereas black lines are guides to the eye.

The temperature dependences of the linewidth of selected B_g and A_g modes are given in the right panels of Figs. 5 and 6, respectively. While the B_g^2 and B_g^4 phonon modes do not show significant deviation from the usual behavior due to the anharmonicity effects, with gradual broadening with increasing temperature, the A_g^4, A_g^7, and A_g^9 modes exhibit moderate additional broadening above 200 K. The red lines present a fit to the standard formula for the temperature dependent linewidth due to the anharmonicity [11,47,51]:

$$\Gamma_i(T) = \Gamma_{0,i}\left(1 + \frac{2}{e^{\hbar\omega_{0,i}/2k_BT} - 1}\right) + A_i, \qquad (2)$$

where $\Gamma_{0,i}$ is the anharmonic constant and A_i is the constant term due to the disorder and electron-phonon interaction [52]. The deviation from these anharmonicity curves is most pronounced around T_N (see the insets of Fig. 6).

We can observe that all Raman modes have moderate linewidth and exhibit small anomalies near T_N. This shows that the phase transition is continuous, in agreement with the thermodynamic and transport measurements [22]. Small anomalies in the phonon spectra, which are restricted only to the vicinity of the phase transition, imply that the electron-phonon interaction of Raman active modes does not change with temperature. This is in agreement with the recent ARPES measurements which show negligible change of the Fermi surface across the AFM transition [42], indicating that the magnetic transition is not driven by the Fermi surface instability. The anomalies in the linewidth of some phonon modes near T_N are likely the signature of the increased scattering by spin fluctuations near the phase transition [51,53].
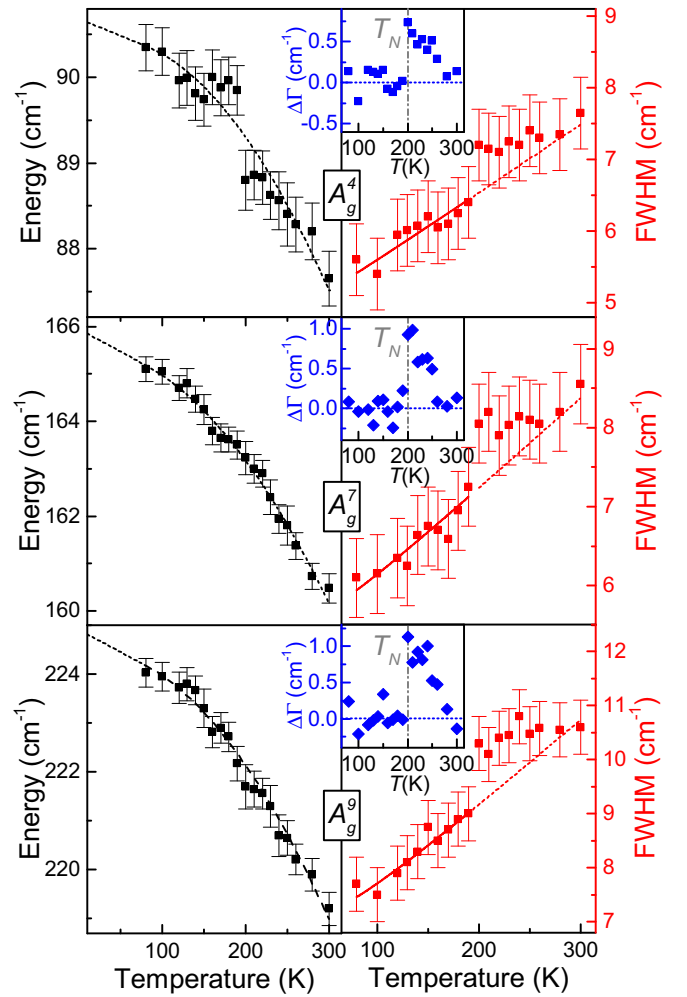

FIG. 6. Energy and linewidth of the A_g^4, A_g^7, and A_g^9 Raman modes of the TaFe$_{1.25}$Te$_3$ single crystal as a function of temperature. The red lines are plotted according to Eq. (2), and the black dotted lines are guides to the eye. The insets represent deviations of the Raman mode linewidth from the anharmonic form.

The density of states (DOS) at the Fermi level is not large. This can be concluded from the ARPES experiments [42] which have shown three bands crossing the Fermi level but with strong dispersion, while several relatively flat bands are found only well below the Fermi level. The DFT calculations also give moderate values for the DOS, $N(E_F) \approx 1\,\mathrm{eV}^{-1}/\mathrm{f.u.}$, after the Fermi level is shifted due to the additional charge provided by the Fe2 atoms. This value for the DOS also suggests that the electron-phonon coupling is not strong in TaFe$_{1.25}$Te$_3$, since it is proportional to $N(E_F)$.

TaFe$_{1.25}$Te$_3$ has a similar moment size as Fe$_{1+y}$Te, $\approx 2\mu_B$/Fe. However, the differences in the magnetic ordering and crystal structure cause different phonon properties of these two compounds. Namely, the phonon lines in the Raman spectra of Fe$_{1+y}$Te have very large linewidth and pronounced anomalies both in the frequency and in the linewidth near the first order phase transition [11,13]. Small anomalies in the Raman spectra of TaFe$_{1.25}$Te$_3$ as compared to Fe$_{1+y}$Te can be ascribed to the continuous, second order nature of the AFM transition and smaller electron-phonon coupling due to lower DOS at the

Fermi level. Also, the monoclinic angle β in the TaFe$_{1.25}$Te$_3$ unit cell significantly differs from $90°$ and therefore the form of the vibrational modes is different.

IV. CONCLUSION

In summary, we have performed the Raman scattering study of the zigzag spin chain TaFe$_{1.25}$Te$_3$ single crystal, together with the lattice dynamics calculations of TaFeTe$_3$. By analyzing the Raman spectra in different polarization configurations and using numerical calculations we have assigned nine Raman active modes predicted by the FGA. Very good agreement between the experimental frequencies and those calculated for the stoichiometric compound shows that the excess iron atoms weakly influence the phonon energies but provide momentum conservation for the phonon scattering away from Γ point. The temperature dependence of the frequency and the linewidth of the B_g Raman modes looks conventional, governed by the anharmonicity effects. While in a broad temperature range the behavior of the A_g modes is also conventional, there are clear anomalies near the AFM transition. The anomalies in the frequency and the linewidth are in the form of small kinks near T_N. This implies that the electron-phonon interaction and the DOS at the Fermi level are approximately constant in the measured temperature range. The increase in the linewidth near T_N is likely due to the coupling of spin fluctuations and vibration near the second order phase transition.

[1] Y. Kamihara, T. Watanabe, M. Hirano, and H. Hosono, J. Am. Chem. Soc. **130**, 3296 (2008).

[2] L. Ma, G. F. Ji, J. Dai, X. R. Lu, M. J. Eom, J. S. Kim, B. Normand, and W. Yu, Phys. Rev. Lett. **109**, 197002 (2012).

[3] B. Wei, H. Qing-Zhen, C. Gen-Fu, M. A. Green, W. Du-Ming, H. Jun-Bao, and Q. Yi-Ming, Chin. Phys. Lett. **28**, 086104 (2011).

[4] G. R. Stewart, Rev. Mod. Phys. **83**, 1589 (2011).

[5] M. Opačić, N. Lazarević, M. M. Radonjić, M. Šćepanović, H. Ryu, A. Wang, D. Tanasković, C. Petrovic, and Z. V. Popović, J. Phys.: Condens. Matter **28**, 485401 (2016).

[6] Z. S. Gönen, P. Fournier, V. Smolyaninova, R. Greene, F. M. Araujo-Moreira, and B. Eichhorn, Chem. Mater. **12**, 3331 (2000).

[7] H. Lei, H. Ryu, A. I. Frenkel, and C. Petrovic, Phys. Rev. B **84**, 214511 (2011).

[8] F. Han, X. Wan, B. Shen, and H.-H. Wen, Phys. Rev. B **86**, 014411 (2012).

[9] M. H. Fang, H. M. Pham, B. Qian, T. J. Liu, E. K. Vehstedt, Y. Liu, L. Spinu, and Z. Q. Mao, Phys. Rev. B **78**, 224503 (2008).

[10] S. Li, C. de la Cruz, Q. Huang, Y. Chen, J. W. Lynn, J. Hu, Y.-L. Huang, F.-C. Hsu, K.-W. Yeh, M.-K. Wu, and P. Dai, Phys. Rev. B **79**, 054503 (2009).

[11] V. Gnezdilov, Y. Pashkevich, P. Lemmens, A. Gusev, K. Lamonova, T. Shevtsova, I. Vitebskiy, O. Afanasiev, S. Gnatchenko, V. Tsurkan, J. Deisenhofer, and A. Loidl, Phys. Rev. B **83**, 245127 (2011).

[12] Y. J. Um, A. Subedi, P. Toulemonde, A. Y. Ganin, L. Boeri, M. Rahlenbeck, Y. Liu, C. T. Lin, S. J. E. Carlsson, A. Sulpice, M. J. Rosseinsky, B. Keimer, and M. Le Tacon, Phys. Rev. B **85**, 064519 (2012).

[13] Z. V. Popović, N. Lazarević, S. Bogdanović, M. M. Radonjić, D. Tanasković, R. Hu, H. Lei, and C. Petrovic, Solid State Commun. **193**, 51 (2014).

[14] K.-Y. Choi, D. Wulferding, P. Lemmens, N. Ni, S. L. Bud'ko, and P. C. Canfield, Phys. Rev. B **78**, 212503 (2008).

[15] M. Rahlenbeck, G. L. Sun, D. L. Sun, C. T. Lin, B. Keimer, and C. Ulrich, Phys. Rev. B **80**, 064509 (2009).

[16] F. Chen, M. Xu, Q. Q. Ge, Y. Zhang, Z. R. Ye, L. X. Yang, J. Jiang, B. P. Xie, R. C. Che, M. Zhang, A. F. Wang, X. H. Chen, D. W. Shen, J. P. Hu, and D. L. Feng, Phys. Rev. X **1**, 021020 (2011).

[17] W. Li, H. Ding, P. Deng, K. Chang, C. Song, K. He, L. Wang, X. Ma, J.-P. Hu, P. Chen, and Q.-K. Xue, Nat. Phys. **8**, 126 (2012).

[18] N. Lazarević, M. Abeykoon, P. W. Stephens, H. Lei, E. S. Bozin, C. Petrovic, and Z. V. Popović, Phys. Rev. B **86**, 054503 (2012).

[19] M. Badding, J. Li, F. DiSalvo, W. Zhou, and P. Edwards, J. Solid State Chem. **100**, 313 (1992).

[20] J. Neuhausen, E. Potthoff, W. Tremel, J. Ensling, P. Gütlich, and R. Kremer, Z. Naturforsch. B **48**, 797 (1993).

[21] C. Perez Vicente, M. Womes, J. C. Jumas, L. Sanchez, and J. L. Tirado, J. Phys. Chem. B **102**, 8712 (1998).

[22] R. H. Liu, M. Zhang, P. Cheng, Y. J. Yan, Z. J. Xiang, J. J. Ying, X. F. Wang, A. F. Wang, G. J. Ye, X. G. Luo, and X. H. Chen, Phys. Rev. B **84**, 184432 (2011).

[23] X. Ke, B. Qian, H. Cao, J. Hu, G. C. Wang, and Z. Q. Mao, Phys. Rev. B **85**, 214404 (2012).

[24] E. Dagotto, Rev. Mod. Phys. **85**, 849 (2013).

[25] W. Li, C. Setty, X. H. Chen, and J. Hu, Front. Phys. **9**, 465 (2014).

[26] E. Dagotto, J. Riera, and D. Scalapino, Phys. Rev. B **45**, 5744 (1992).

[27] E. Dagotto and T. M. Rice, Science **271**, 618 (1996).

[28] E. Dagotto, Rep. Prog. Phys. **62**, 1525 (1999).

[29] M. Uehara, T. Nagata, J. Akimitsu, H. Takahashi, N. Môri, and K. Kinoshita, J. Phys. Soc. Jpn. **65**, 2764 (1996).

[30] A. Hisada, K. Matsubayashi, Y. Uwatoko, N. Fujiwara, G. Deng, E. Pomjakushina, K. Conder, D. M. Radheep, R. Thiyagarajan, S. Esakkimuthu, and S. Arumugam, J. Phys. Soc. Jpn. **83**, 073703 (2014).

[31] H. Takahashi, A. Sugimoto, Y. Nambu, T. Yamauchi, Y. Hirata, T. Kawakami, M. Avdeev, K. Matsubayashi, F. Du, C. Kawashima, H. Soeda, S. Nakano, Y. Uwatoko, Y. Ueda, T. J. Sato, and K. Ohgushi, Nat. Mater. **14**, 1008 (2014).

[32] A.-M. Zhang and Q.-M. Zhang, Chin. Phys. B **22**, 087103 (2013).

[33] M. Opačić and N. Lazarević, J. Serb. Chem. Soc. **82**, 957 (2017).

[34] L. Zhang, T. Fujita, F. Chen, D. L. Feng, S. Maekawa, and M. W. Chen, Phys. Rev. B **79**, 052507 (2009).

[35] Y. Gallais, A. Sacuto, M. Cazayous, P. Cheng, L. Fang, and H. H. Wen, Phys. Rev. B **78**, 132509 (2008).

[36] V. Gnezdilov, Y. G. Pashkevich, P. Lemmens, D. Wulferding, T. Shevtsova, A. Gusev, D. Chareev, and A. Vasiliev, Phys. Rev. B **87**, 144508 (2013).

[37] A. P. Litvinchuk, B. Lv, and C. W. Chu, Phys. Rev. B **84**, 092504 (2011).

[38] K.-Y. Choi, P. Lemmens, I. Eremin, G. Zwicknagl, H. Berger, G. L. Sun, D. L. Sun, and C. T. Lin, J. Phys.: Condens. Matter **22**, 115802 (2010).

[39] S. Baroni, S. de Gironcoli, A. Dal Corso, and P. Giannozzi, Rev. Mod. Phys. **73**, 515 (2001).

[40] P. Gianozzi, S. Baroni, N. Bonini, M. Calandra, R. Car, C. Cavazzoni, D. Ceresoli, G. L. Chiarotti, M. Cococcioni, I. Dabo, A. D. Corso, S. de Gironcoli, S. Fabris, G. Fratesi, R. Gebauer, U. Gerstmann, C. Gougoussis, A. Kokalj, M. Lazzeri, L. Martin-Samos, N. Marzari, F. Mauri, R. Mazzarello, S. Paolini, A. Pasquarello, L. Paulatto, C. Sbraccia, S. Scandolo, G. Sclauzero, A. P. Seitsonen, A. Smogunov, P. Umari, and R. M. Wentzcovitch, J. Phys.: Condens. Matter **21**, 395502 (2009).

[41] D. L. Rousseau, R. P. Bauman, and S. P. S. Porto, J. Raman Spectrosc. **10**, 253 (1981).

[42] X. Min, W. Li-Min, P. Rui, G. Qing-Qin, C. Fei, Y. Zi-Rong, Z. Yan, C. Su-Di, X. Miao, L. Rong-Hua, M. Arita, K. Shimada, H. Namatame, M. Taniguchi, M. Matsunami, S. Kimura, S. Ming, C. Xian-Hui, Y. Wei-Guo, K. Wei, X. Bin-Ping, and F. Dong-Lai, Chin. Phys. Lett. **32**, 027401 (2015).

[43] R. Shuker and R. W. Gammon, Phys. Rev. Lett. **25**, 222 (1970).

[44] P. Benassi, O. Pilla, V. Mazzacurati, M. Montagna, G. Ruocco, and G. Signorelli, Phys. Rev. B **44**, 11734 (1991).

[45] H. Ryu, M. Abeykoon, K. Wang, H. Lei, N. Lazarevic, J. B. Warren, E. S. Bozin, Z. V. Popovic, and C. Petrovic, Phys. Rev. B **91**, 184503 (2015).

[46] B.-B. Zhang, N. Zhang, S.-T. Dong, Y. Lv, Y. B. Chen, S. Yao, S.-T. Zhang, Z.-B. Gu, J. Zhou, I. Guedes, D. Yu, and Y.-F. Chen, AIP Adv. **5**, 087111 (2015).

[47] J. Menéndez and M. Cardona, Phys. Rev. B **29**, 2051 (1984).

[48] H.-M. Eiter, P. Jaschke, R. Hackl, A. Bauer, M. Gangl, and C. Pfleiderer, Phys. Rev. B **90**, 024411 (2014).

[49] N. Lazarević, M. Radonjić, M. Šćepanović, H. Lei, D. Tanasković, C. Petrovic, and Z. V. Popović, Phys. Rev. B **87**, 144305 (2013).

[50] M. Opačić, N. Lazarević, M. Šćepanović, H. Ryu, H. Lei, C. Petrovic, and Z. V. Popović, J. Phys.: Condens. Matter **27**, 485701 (2015).

[51] M. N. Iliev, A. P. Litvinchuk, H.-G. Lee, C. W. Chu, A. Barry, and J. M. D. Coey, Phys. Rev. B **60**, 33 (1999).

[52] N. Lazarević, Z. V. Popović, R. Hu, and C. Petrovic, Phys. Rev. B **81**, 144302 (2010).

[53] M. N. Iliev, A. P. Litvinchuk, H.-G. Lee, C. L. Chen, M. L. Dezaneti, C. W. Chu, V. G. Ivanov, M. V. Abrashev, and V. N. Popov, Phys. Rev. B **59**, 364 (1999).

Journal of the Serbian Chemical Society

REVIEW

Lattice dynamics of iron chalcogenides: Raman scattering study

MARKO R. OPAČIĆ[1,2]* and NENAD Ž. LAZAREVIĆ[2]

[1]*Faculty of Electrical Engineering, Bulevar Kralja Aleksandra 73, University of Belgrade, Belgrade, Serbia and* [2]*Center for Solid State Physics and New Materials, Institute of Physics, Pregrevica 118, University of Belgrade, Belgrade, Serbia*

Abstract: The discovery of superconductivity in FeSe led to a new subclass of high-temperature superconductors – iron chalcogenides. Materials from this group exhibit variety of specific features, from superconductivity with relatively high critical temperatures to low-dimensional magnetic properties. This review presents the most important results regarding the iron chalcogenides, with special emphasis on their vibrational properties investigated by means of Raman spectroscopy. Temperature- and/or doping-dependent Raman scattering spectra of iron chalcogenides provide a valuable insight into the complex relationships between the vibrational, electronic and magnetic properties of these materials. The results presented in this review demonstrated that Raman spectroscopy provides new insights which may significantly improve our understanding of the fundamental properties of iron chalcogenides.

Keywords: superconductors; phonons; energy; linewidth.

CONTENTS

957

1. INTRODUCTION

Superconductivity (SC) is one of the greatest and the most striking phenomena discovered so far in the materials science. The history of SC began in 1911, when Kamerlingh-Onnes observed it in mercury below 4 K.[1] Since then, researchers made a great effort in searching for materials with as high as possible superconducting critical temperature T_c.

The breakthrough in the development of SC materials happened with the discovery of SC in oxide compounds. In 1975, $Ba(Pb,Bi)O_3$ was reported with $T_c \approx 13$ K,[2] which motivated further intensive studies. These investigations resulted in the discovery of SC in $La_{2-x}Ba_xCuO_2$ system ($T_c = 35$ K) – the first high-temperature superconductor,[3] as well as in $YBa_2Cu_3O_{7-x}$ compound ($T_c = 92$ K).[4] Numerous SC materials from this class were found in quick succession, from which $HgBa_2Ca_2Cu_3O_8$ ($T_c = 134$ K) should be mentioned.[5] All cuprate superconductors have distorted, oxygen-deficient, multi-layered perovskite structure. The most important property is an alternating multi-layer of CuO_2 planes, with intercalated layers containing Y, Ba, La, Sr,..., which act to stabilize the structure and to dope the carriers onto the CuO_2.[6–8] This structure causes a large anisotropy in normal conducting and superconducting properties.[6,8] Parent (undoped) compounds are Mott insulators, with long range antiferromagnetic (AFM) order at low temperatures.[7,8] Similarities between the AFM state of the undoped materials and doping-induced SC state indicate that the electron–electron interaction is more significant than electron-phonon interaction, making the SC unconventional.[9,10] It was argued that cuprates have d-wave pairing symmetry and one Fermi surface sheet.[11]

The first iron-based superconductor was discovered in 2006 (LaFePO, $T_c = = 5$ K).[12] However, until 2008, when Kamihara et al.[13] found SC in $LaFeAsO_{1-x}F_x$ with $T_c = 26$ K (43 K under high pressure), it was widely believed that only cuprates belong to the class of unconventional high-T_c superconductors. This discovery led to a new class of the so-called iron pnictide SC which includes several types of materials, denoted according to their crystal structure: 1111-compounds (LaFePO, LaFeAsO, $SmFeAsO_{1-x}$ with $T_c = 56$ K[14]), 122-family ($Ba_{0.6}K_{0.4}Fe_2As_2$ with $T_c = 38$ K[15]), 111-compounds (MFeAs, $T_c = 18$ K[16]), etc. Crystal structure of these superconductors is given in Fig. 1. All these materials crystallize into the [FeAs]-layered structure, with spacer or charge reservoir blocks between the FeAs-layers.[17,18] The parent compounds are poor metals and it is widely believed that proximity to the magnetically ordered states induces SC, making them unconventional, like in the cuprates.[17,18] However, in iron pnictides SC and AFM order can coexist, contrary to the cuprates, where SC state emerges only after the AFM order is destroyed by doping.[18,19] Symmetry of the pairing wave function can be of the $s^{\pm}$-type,[20,21] although this is still under intensive debate.
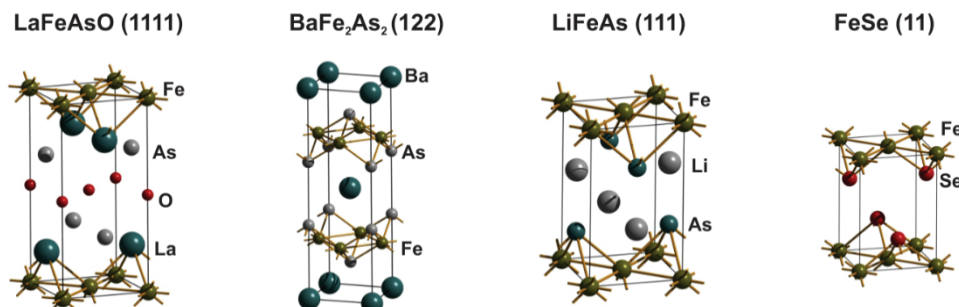
Fig. 1. Crystal structure of the representative iron-based superconductors.

FeSe is the first discovered material from one of the newest subclasses of iron-based superconductors – iron chalcogenides.[22] Its physical properties are extremely sensitive to doping on the chalcogen site, as well as to the Fe concentration, and T_c can be enhanced by applying pressure.[23,24] Intercalation of alkali metal between the FeSe layers led to the formation of $A_xFe_{2-y}Se_2$ (A = alkali metal) crystals with the defect 122* structure.[25] These materials exhibit very interesting properties, including the presence of AFM phase with ordered vacancies and vacancy-free SC/semiconducting phase, unconventional superconductivity with $T_c > 30$ K and large iron magnetic moments.[25–28] Absence of hole pockets at the Fermi surface suggests that the pairing mechanism may differ from the one in the pnictides. By cutting the layers of $FeSe_4$ tetrahedra, *e.g.*, removing every third Fe atom from these layers, one obtains a basic building block of the so-called spin-ladder compounds $BaFe_2Se_3$ ($BaFe_2S_3$).[29] These compounds have low-dimensional magnetic properties, which opened a new field in searching for new iron-based materials.[30–33]

In this article an overview of iron-chalcogenides is presented, but instead of a comprehensive review of their features, we focus our attention on the vibrational properties studied by Raman spectroscopy, as a suitable technique for investigating lattice and magnetic excitations of crystalline solids. It can also provide valuable information about coupling of phonons with electrons and charge-density waves and might even serve as a useful tool for probing the crystal symmetry.[34–36]

2. 11-TYPE MATERIALS

2.1. Crystal structure

Materials with the general formula FeCh (Ch = Se or Te), belonging to this group, have the simplest structure among all iron chalcogenides. They are built of edge-sharing $FeCh_4$ tetrahedra stacked along the crystallographic *c*-axis, see Fig. 1. At room temperature, they adopt the tetragonal crystal structure of the PbO type, space group *P4/nmm*.[22,37,38]

The crystal structure of FeSe at low temperatures is orthorombic, space group *Cmma*,[24,37,39] although it was initially proposed that $FeSe_{0.88}$ below $T_s \approx$ ≈ 100 K changes symmetry into triclinic, space group *P*-$\bar{1}$.[22] Structural transition temperature T_s for FeSe differs between various papers, depending strongly on the strain and sample stoichiometry.[37,40,41] Based on the temperature evolution of synchrotron X-ray diffraction profiles of $FeSe_{0.92}$,[37] it is concluded that T_s is about 70 K, whereas elsewhere[40] is showed that the phase transition in SC $Fe_{1.01}Se$ occurs at 90 K.

With Te-doping of FeSe crystals, the tetragonal-to-orthorombic structural transition moves toward lower temperatures and finally disappears for $FeTe_{0.507}Se_{0.493}$.[42] For low Te-content a miscible region with the local phase separation between two phases emerges.[23,43] These two phases have the same space group (*P4/nmm*) but different lattice parameters. With further increasing Te-concentration, the monoclinic structure appears at low temperatures (space group *P2₁/m*), instead of orthorombic.[38] Martinelli e*t al*.[38] reported tetragonal-to-monoclinic phase transition in $Fe_{1+y}Te_{1-x}Se_x$ crystals for $x \leq 0.1$, with increasing T_s as x decreases. For the end member $Fe_{1+y}Te$, the structural transition occurs around 70 K.

2.2. Physical properties

FeSe exhibits metallic behavior of electrical resistivity (ρ) from room temperature down to $T_c \approx 8$ K, where a sharp drop to zero resistance occurs.[22,23,43] Some authors[22] noticed a weak anomaly at about 100 K, which coincide with the anomaly in magnetic susceptibility $\chi(T)$, and attributed them to the structural transition. They observed almost temperature independent magnetic susceptibility for $T > T_c$, which led them to conclude that FeSe does not order magnetically.[22] However, recent inelastic neutron scattering experiments revealed stripe and Neel spin fluctuations over a wide energy range.[44] Susceptibility measurements also showed SC transition at about 8 K.[22,43] Temperature dependence of resistivity under various pressures is analyzed,[24] and the SC transition was noticed below 13.4 K for low pressures. With the increasing pressure, T_c rapidly increases and reaches maximal value of 37 K at about 6.6 GPa. With further pressurization, T_c decreases and at 13.9 GPa $T_c \approx 6$ K.[24] It was recently shown that an electronic nematic state develops below T_s,[45,46] suggesting that structural transition in FeSe may be driven by the orbital, magnetic and/or charge instability.

FeTe does not exhibit the SC transition.[38,43] Its resistivity weakly increases with decreasing temperature and exhibits an upturn at about 77 K, with rapid drop. Below the structural phase transition temperature $T_s = 70$ K FeTe has metallic behaviour.[38,43] Structural transition is followed by the AFM spin ordering, with $T_N \approx T_s$.[42] For $FeTe_{0.82}$ single crystals, magnetic susceptibility curve $\chi(T)$ exhibits two anomalies, at 65 and 125 K. Anomalous peak in $\rho(T)$ also appears at 65 K.[23] It was later shown that this behaviour is connected with the structural and

AFM phase transition.[47] Hall constant, R_H, is negative in the temperature range 10 K $\leq T \leq$ 160 K, indicating that charge carriers are dominantly electrons.[23]

Comprehensive study of physical properties of Fe(Se$_{1-x}$Te$_x$)$_{0.82}$, $0 \leq x \leq 1$, alloys is performed.[23] Maximal T_c of about 14 K is achieved for the sample with $x = 0.6$, and SC disappears in the end member ($x = 1$). Anomaly in the susceptibility at 125 K, similar to that in FeTe$_{0.82}$, persists for all samples with $x > 0.4$. It was shown that,[47] for the (FeSe$_{0.4}$Te$_{0.6}$)$_{0.82}$ sample, short range magnetic correlations appear below 75 K and rapidly enhance below 40 K, which coincide with anomalous temperature dependence of R_H in this temperature range, indicating the strong interplay between spin and charge degrees of freedom.[23] Samples with $0 \leq x \leq 0.15$ have metallic resistivity from room temperature down to T_c, whereas samples with $0.3 \leq x \leq 1$ have a weak upturn before approaching the SC transition temperature.[23] This is consistent with the results for FeTe$_{1-x}$Se$_x$, $0 < x \leq 0.2$, alloys,[38] where all samples show an upturn in $\rho(T)$ below 100 K, which weakens and shifts to lower temperature as x increases, and metallic behavior at lower temperatures. For $x \geq 0.05$, material become SC, and T_c increases with increasing Se content.[38] Similar resistivity curves were also obtained for FeSe$_{1-x}$Te$_x$ samples with low Se content, where it was found that T_c increases with x for $x \leq 0.75$, and $T_{c,max} = 15.3$ K for $x = 0.25$.[43]

2.3. Raman scattering studies

According to the factor group analysis (FGA) for the *P4/nmm* space group, four Raman active modes (A$_{1g}$+B$_{1g}$+2E$_g$) could be observed in the room-temperature Raman spectra of FeCh (Ch = Se or Te) materials. A$_{1g}$ mode represents vibrations of the Ch-ions, whereas B$_{1g}$ one represents Fe-ion vibrations along the *z*-axis. Twofold degenerate E$_g$ modes originate from Fe- and Ch-ion vibrations within the *ab*-plane.[39,48]

Vibrational properties of 11-iron chalcogenides were extensively studied by means of Raman spectroscopy.[48–52] Almost all authors observed and assigned, at room temperature, two Raman active modes, of A$_{1g}$ and B$_{1g}$ symmetry, allowed by the selection rules when measuring from the (001)-plane of the sample. The A$_{1g}$ mode was not observed in Fe$_{1.03}$Se$_{0.3}$Te$_{0.7}$ sample,[49] although in FeTe$_{0.92}$ sample it is present; it was suggested that it may be due to the vacancies introduced into the system with Se doping, or slightly different excess of Fe-ions. Energies of the A$_{1g}$ and B$_{1g}$ modes for different samples are compared in Table I. As can be seen, they are rather close. However, temperature dependence of Raman mode energy, $\omega(T)$, and linewidth, $\Gamma(T)$, differs substantially between various papers. The spectrum of FeSe single crystal,[39] is shown in Fig. 2.

Magnetic transition that exists in FeTe leaves a clear fingerprint on the behavior of B$_{1g}$ mode energy and linewidth.[48,50,52] Namely, the B$_{1g}$ mode exhibits significant softening and narrowing below $T_N \approx 70$ K (where it changes the sym-

metry to A_g[52]) for all samples except $Fe_{1.09}Te$. Besides that, both the B_{1g} mode energy and linewidth decrease with decreasing temperature[48,50,52] (Fig. 3) and it was shown[52] that they scales well with the normalized magnetic susceptibility, confirming that spin-phonon coupling substantially influence the behaviour of the $B_{1g}(Fe)$ mode.

TABLE I. Experimentally obtained energies of the A_{1g} and B_{1g} Raman modes at room temperature (except for FeSe,[51] for which data are shown at $T = 5$ K) for some FeCh single crystals

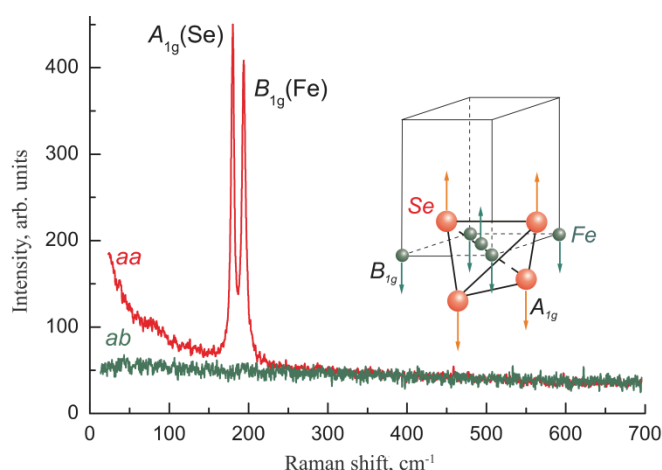| Wave number	$Fe_{1.05}Te$[48]	$Fe_{1.07}Te$[52]	$FeTe_{0.92}$[49]	$FeTe_{0.6}Se_{0.4}$[51]	FeSe[39]
$\bar{v}$ (A_{1g}) / cm^{-1}	155.2	156	159.1	161	179.8
$\bar{v}$ (B_{1g}) / cm^{-1}	201.4	198	196.3	202	193.9

Fig. 2. Polarized Raman scattering spectra of FeSe, room temperature. The inset shows the displacement patterns of the observed modes.[39] (Reprinted with permission from Ref. 39, copyright (2013) by the American Physical Society).

Absence of the B_{1g} phonon softening below T_N for $Fe_{1.09}Te$ single crystal[50] was ascribed to the significant Fe excess, which contributes to the filling up the gap in the spin-wave excitation spectrum with the low-energy spin fluctuations. Unlike the B_{1g} one, behaviour of the A_{1g} symmetry mode differs substantially. The only common feature is the large intrinsic linewidth, which is attributed[48] to the spin-orbital frustration, whereas elsewhere[52] is suggested that electron–phonon interaction may also play an important role.

The A_{1g} mode for $Fe_{1.051}Te$[48] hardens and broadens with decreasing temperature, showing a weak anomaly in $\omega(T)$ at T_s, followed by more rapid increase of $\Gamma(T)$ below T_s. Authors believe that the A_{1g} mode energy renormalization is caused by the phonon modulation of the magnetic interactions and by the anti-phase motion of Te-ions surrounding Fe-ions, which modulates exchange interaction. Rapid increase of the A_{1g} mode linewidth is attributed to the spin-orbital

frustration. Energy and linewidth of the A_{1g} mode for $Fe_{1.02}Te$ and $Fe_{1.09}Te$[50] remains almost constant at the temperatures up to 300 K. The A_{1g} mode energy and linewidth were analyzed[52] using phonon anharmonicity model and good agreement is obtained between experimental data and calculated spectra, indicating that they follow anharmonic temperature dependence.
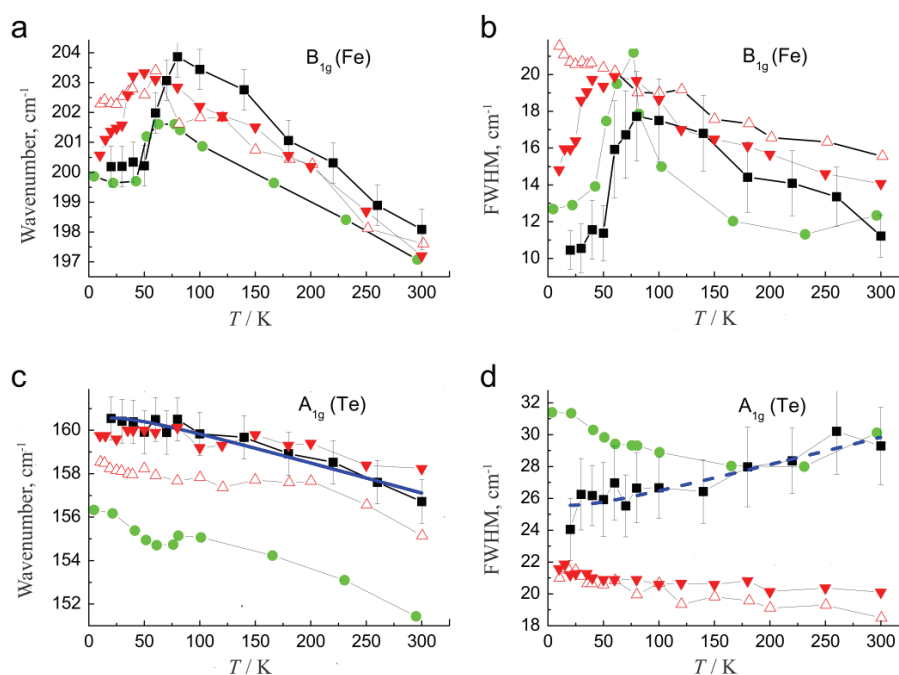

Fig. 3. Comparison of energy and linewidth temperature dependence for A_{1g} and B_{1g} Raman active modes of $Fe_{1+y}Te$ crystals. Filled circles represent data from Ref. 48, open triangles data from Ref. 50, $y = 0.09$, filled triangles data from Ref. 50, $y = 0.02$, and filled squares data from Ref. 52. Solid and dashed lines are calculated spectra using phonon anharmonicity model. (Reprinted from Ref. 52, copyright (2017) with permission from Elsevier).

Effect of Se doping on FeTe Raman spectra has also been investigated.[49,50,52] Um *et al.*[50] analyzed Raman spectra of Se-doped FeTe single crystals and showed that in the sample with the highest Se content ($Fe_{0.95}Te_{0.56}Se_{0.44}$) change of the A_{1g} and B_{1g} mode energy and linewidth with temperature is in agreement with the anharmonic picture: the phonon energy increases and the linewidth decreases with the decreasing temperature. By decreasing Se content, the energy and the linewidth of these modes gradually moves away from the conventional behaviour and for the $Fe_{1.00}Te_{0.78}Se_{0.22}$ crystal the B_{1g} phonon even broadens with decreasing temperature (Fig. 4). Absence of phonon renormalization at T_c for these SC samples is expected because their energies are much larger than the energy of the SC gap.[50]
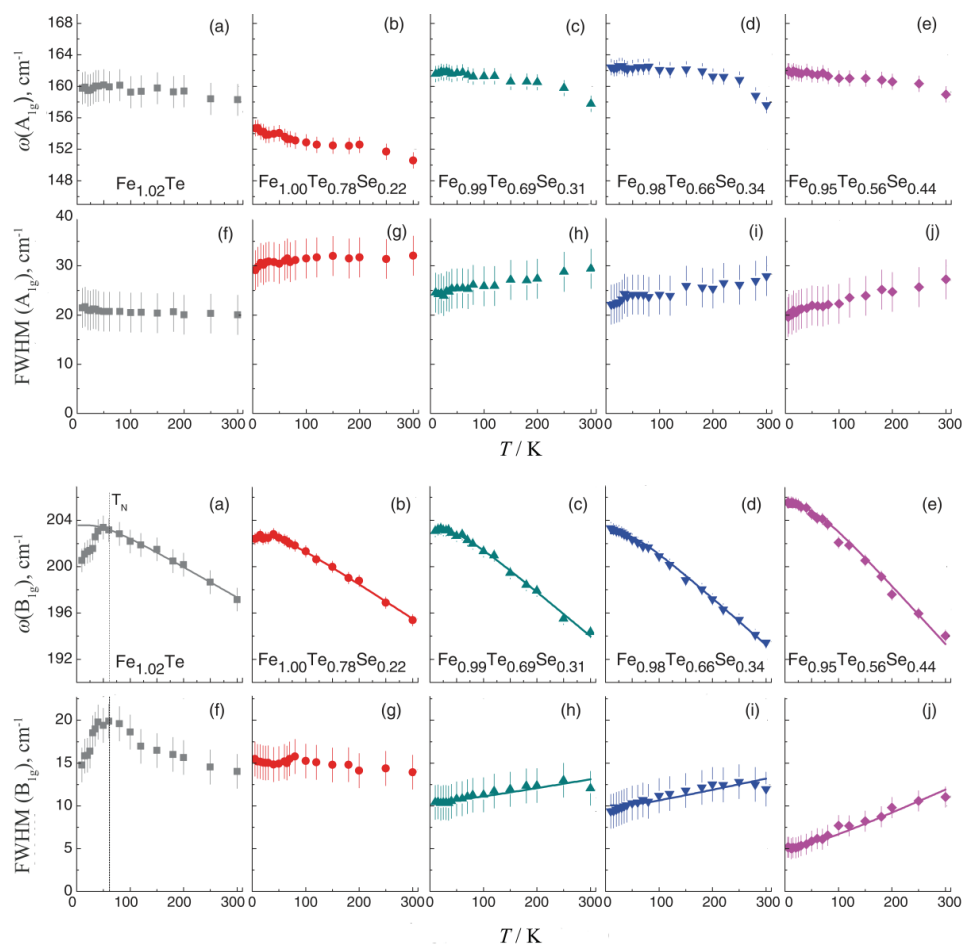
Fig. 4. Temperature dependence of the A_{1g} and B_{1g} mode frequency (ω) and f linewidth (FWHM) of the $Fe_{1.02}Te$, $Fe_{1.00}Te_{0.78}Se_{0.22}$, $Fe_{0.99}Te_{0.69}Se_{0.31}$, $Fe_{0.98}Te_{0.66}Se_{0.34}$ and $Fe_{0.95}Te_{0.56}Se_{0.44}$ samples.[50] (Reprinted with permission from Ref. 50, copyright (2012) by the American Physical Society).

More detailed analysis of the B_{1g} mode linewidth temperature dependence for Se-doped samples revealed that with decreasing Se content its intrinsic linewidth increases, which is attributed to the influence of the spin–phonon coupling, since lower Se (higher Te) content means stronger magnetic interactions. Raman spectra of Se-doped $Fe_{1+y}Te$ crystals were analyzed[52] with respect to the undoped case. It was observed that the A_{1g} and B_{1g} modes have opposite behaviour of energy and linewidth with Se doping: A_{1g} mode hardens and narrows whereas the B_{1g} one softens and broadens with increasing Se content. A_{1g} mode hardening is explained by the mass effect, whereas decreased linewidth is attributed to the lower electron–phonon interaction and/or to the excess Fe-ions. On the other

hand, B_{1g} mode broadening in $Fe_{1.02}Te_{0.6}Se_{0.4}$ compared with $Fe_{1.07}Te$ authors ascribed to the induced structural disorder, whereas phonon softening could be explained with the change in excess iron in these two single crystals. Qualitatively similar behaviour is presented[50] for the A_{1g} mode, whereas for the B_{1g} one the situation is almost opposite.

Temperature-dependent phonon Raman spectra of FeSe were analyzed in detail.[39] Room-temperature spectra consist of A_{1g} and B_{1g} modes, as expected from the selection rules. Due to the structural transition into the ortorhombic phase (*e.g.*, lowering of the rotational symmetry from C4 to C2), A_{1g} mode changes symmetry becoming A_g one, but without energy change, and three new modes appearing at higher energies can be of B_{2g}/B_{3g} symmetry, according to the *Cmma* space group. They emerge due to the splitting of E_g mode from the tetragonal phase. Both A_{1g} and B_{1g} mode energies vary smoothly with temperature, and large B_{1g} mode hardening with decreasing temperature is argued to be a consequence of the dynamical crossover from Fe spin state $S = 2$ to $S = 0$ with the lowering of temperature.[39] They suggested that smooth temperature dependence of the phonon linewidth at T_s indicates that orbital fluctuations do not have significant impact on the behavior of Raman modes. Highly polarized quasi-elastic response emerging in Raman spectra of the tetragonal phase, with maximal intensity at T_s, is considered as a fingerprint of electronic nematic fluctuations.[39,53] E_g mode splitting to $B_{2g}+B_{3g}$ phonons in FeSe, as a consequence of C4-symmetry breaking, is found to be only about 2.6 cm^{-1}, which is small in comparison to $Ba(Fe_{1-x}Co_x)_2As_2$, probably due to the lack of the magnetic order (Fig. 5).[54] This
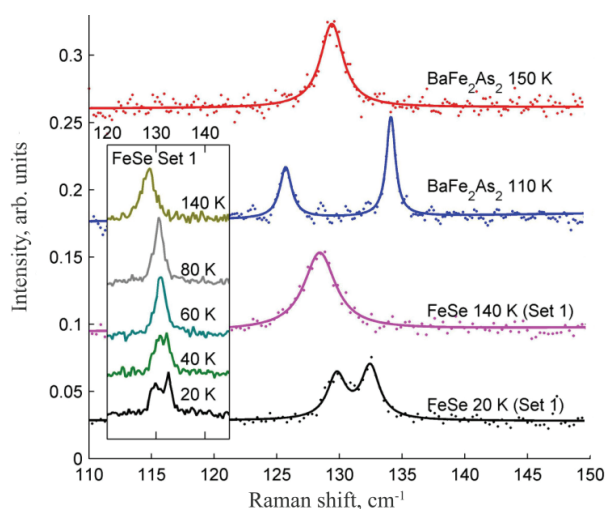

Fig. 5. Raman spectra of $BaFe_2As_2$ and FeSe single crystals. The inset shows temperature dependence of the FeSe Raman spectrum near 130 cm^{-1}, vertically offset for clarity.[54] (Reprinted with permission from Ref. 54, copyright (2016) by the American Physical Society).

splitting sets in below 65 K, where the spin-lattice relaxation rate is found to increase, which led to the conclusion that spin correlations have stronger influence to the lattice than the orbital interactions.[46]

3. 122*-TYPE MATERIALS

3.1. Crystal structure

The SC in this class was firstly discovered in a sample with the nominal composition $K_{0.8}Fe_2Se_2$, with the proposed tetragonal crystal structure of the $ThCr_2Si_2$-type, space group *I4/mmm*.[25] It consists of FeSe layers and K atoms stacked alternatively along the *z*-axis (Fig. 6a). Intercalation of the K atoms between the FeSe slabs significantly increases the lattice parameter *c* (decreasing
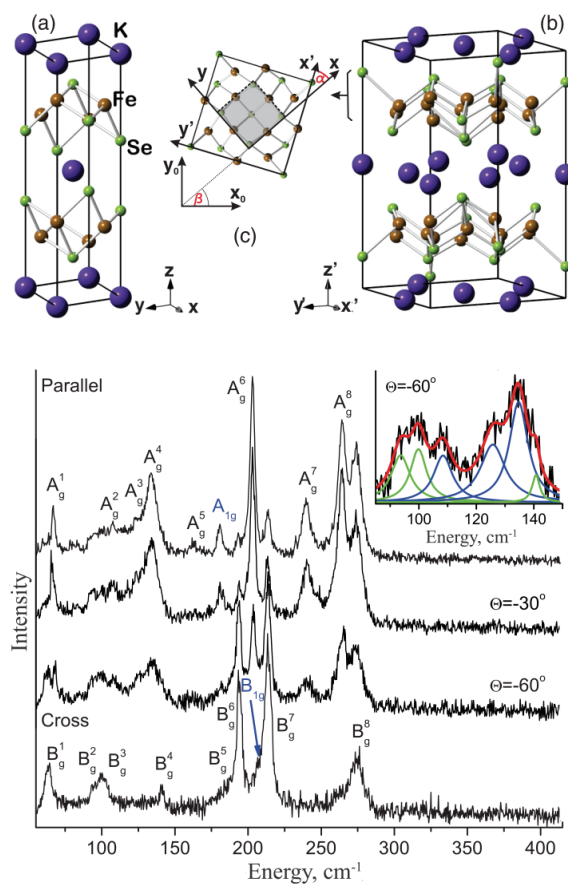

Fig. 6. Crystal structure of $K_xFe_{2-y}Se_2$ within: a) *I4/mmm* and b) *I4/m* unit cells; c) FeSe layer in the (001)-plane of the sample. The solid line represents *I4/m*, whereas shaded square illustrates *I4/mmm* unit cell. Angle between principal axes of the two phases is around 26.6°. Parallel: Raman spectra of $K_xFe_{2-y}Se_2$ measured at 85 K in various polarization configuration ($\Theta = \sphericalangle(\mathbf{e_i},\mathbf{e_s})$).[28]

dimensionality of the system), as well as the interlayer Fe–Fe spacing. $(Fe_2Se_2)^{\delta-}$ layers serve as conducting layers, whereas K^+ are charge carriers. Fe–Se–Fe bond angle is very close to the angle of the ideal tetrahedra (109.47°).[25]

However, the appearance of additional peaks in the neutron powder diffraction (NPD) spectra indicated that symmetry lowering to *I4/m* phase occurs, due to the Fe vacancies ordered into the √5×√5 superlattice in the FeSe plane (Fig. 6b).[26] Zavalij *et al.*[55] and Wang *et al.*[56] also suggested √5×√5 order of the iron vacancies. Fe vacancy order disappears at very high temperature (500 K ≤ T_s ≤ ≤ 578 K), depending on the sample composition,[26,57] and *I4/mmm* symmetry is achieved.

The application of the transmission electron microscopy, Chen *et al.*[58] showed that $K_xFe_{2-y}Se_2$ single crystals exhibit a mesoscopic phase separation between an insulating phase with √5×√5 vacancy order and SC/semiconducting phase free of vacancies (*i.e.*, with composition KFe_2Se_2, space group *I4/mmm*). This is also seen by Li e*t al.*[27] on $K_xFe_{2-y}Se_2$ thin films. PXRD measurements confirmed[28] the phase separation: experimental data were well described with the mixture of *I4/m* and *I4/mmm* space groups. Presence of both phases was also confirmed by Raman scattering measurements.[28,59–61] On the other hand, Bao *et al.*[62] reported phase separation between three phases (*I4/m*, *I4/mmm* and *Pmna*) in $K_xFe_{2-y}Se_2$ samples for 1.4 ≤ 2–*y* ≤ 1.6 and *x* > 0.85 (the samples have general formula $K_2Fe_3Se_4$) between T_s and $T^* \approx 350$ K, whereas below T^* only *I4/m* phase with ordered Fe vacancies persists. For Fe content 1.6 ≤ 2–*y* ≤ 1.7 the sample composition is described with $K_2Fe_4Se_5$ and below T_s their space group is *I4/m*.[62]

Doping of $K_xFe_{2-y}Se_2$ crystals on either chalcogen or transition metal site significantly affects their properties. It was recently shown[60] that the phase separation persists in Co-doped $K_xFe_{2-y}Se_2$ single crystals. However, when Co content is significant (*z* ≥ 0.92 in $K_xFe_{2-y-z}Co_zSe_2$), vacancy order was not observed and these samples belong to the *I4/mmm* space group.[60,63,64] Doping of $K_xFe_{2-y}Se_2$ with small Ni content also preserves the phase separation.[59] Similarly to the Co-doped case, in $K_xFe_{2-y-z}Ni_zSe_2$ samples with *z* ≥ 0.73 low symmetry *I4/m* phase disappears.[59] Pure $K_xNi_{2-y}Se_2$ crystallizes in the tetragonal crystal structure with *I4/mmm* space group, without any indications of vacancy ordering,[65–67] as well as his Co-counterpart. $K_xFe_{2-y}Se_2$ samples doped with S on chalcogen site exhibit iron vacancy order for all doping levels.[68,69]

3.2. Physical properties

Detailed investigations revealed that the physical properties of $K_xFe_{2-y}Se_2$ strongly depend on the sample composition, *i.e.*, K- and Fe-stoichiometry. Bao *et al.*[62] systematically studied few samples having general formula $K_xFe_{2-y}Se_2$ and obtained different properties for various sample compositions. Two samples with higher Fe and lower K content exhibit SC with $T_c \approx 30$ K and large resistivity just

above T_c. These samples show poor diamagnetic response below T_c. With the gradually increasing K content, a bump in $\rho(T)$ appears, which is attributed to the metal–insulator crossover, similarly to the results presented elsewhere:[25] above the peak, samples show semiconducting behaviour, whereas below the bump down to T_c, $\rho(T)$ has typical metallic character. Peak position is strongly dependent on the sample composition.[25,62] With the further increasing of K and the decreasing of Fe content, the gradual opening of transport activation gap was observed in the resistivity.[62]

Early studies of the magnetic properties of alkali metal iron selenides revealed that AFM order appears at $T_N \approx 560$ K, slightly below the Fe vacancy ordering temperature T_s.[26,62] The four magnetic moments from the nearest neighbouring Fe atoms order ferromagnetically (FM), whereas these FM blocks form the block-checkerboard AFM order, with very high magnetic moment (3.31 μ_B/Fe at 11 K).[26] SC transition strongly affects the magnetic order parameter, suggesting significant interaction between SC and AFM order.[26]

Recent studies indicated that SC in $K_xFe_{2-y}Se_2$ was highly influenced by the connectivity between SC phases and the proximity effects.[70,71] Three $K_xFe_{2-y}Se_2$ samples with different microstructure exhibited different T_c,[71] although they all have approximately the same fractional ratio of the SC area and similar resistive and magnetic properties. Huang *et al.*[71] showed that proximity effects, that is, the interlayer hopping and interlayer spin coupling, reduce T_c from the theoretically predicted 65 K to the experimentally observed 32 K. On the other hand, large AFM order results in a large SC order, thus explaining relatively high T_c.[71]

The chemical doping is an appropriate way to tune and control physical properties of materials, since it introduces changes in the structure and carrier density. Doping on the Fe site with other transition metals is detrimental for SC.[72] Namely, Cr-, Co- and Zn-doping rapidly suppresses SC in the $K_{0.8}Fe_{2-y}Se_2$, by inducing a large effective magnetic moment, thus destroying SC *via* a magnetic pair-breaking effect.[72] Recently reported study of Ni-doped $K_xFe_{2-y}Se_2$ single crystals[59] shows that small Ni content destroys SC, leading to the insulating behaviour, whereas with further Ni-doping metallic character of crystals gradually increases. It was also shown that these materials exhibit spin glass behaviour below critical temperature T_f of 10–50 K, depending on the Ni concentration.[59] $K_xNi_{2-y}Se_2$ have a local charge-density-wave state persisting up to 300 K.[65] Some authors[66] reported the metallic resistivity of $K_xNi_{2-y}Se_2$ single crystal up to the room temperature, without SC transition or bump in the $\rho(T)$, unlike the $K_xFe_{2-y}Se_2$. SC is suppressed probably due to the K and Ni deficiency, indicating the strong sensitivity to the sample composition. Magnetic measurements revealed that this material is Pauli paramagnet, with local magnetic moments much lower than in $K_xFe_{2-y}Se_2$.[66] Co-doped $K_xFe_{2-y}Se_2$ single crystals behave similarly to its Ni-counterparts.[60] Preliminary analysis of $K_xCo_{2-y}Se_2$ single crystals indi-

cate the FM phase transition at 74 K and absence of SC.[73] When S completely replaces Se in $K_xFe_{2-y}Se_2$, single crystal becomes a small-gap semiconductor, which is ascribed to the random scattering potential introduced by the Fe deficiency, and exhibits a spin glass behaviour below 32 K.[68,69]

3.3. Raman scattering studies

FGA for the *I4/m* space group predicts $9A_g$, $9B_g$ and $9E_g$ modes to be observed in the Raman scattering experiments,[28,61] whereas for the *I4/mmm* space group only four phonon modes ($A_{1g}+B_{1g}+2E_g$) are expected to be observed.[28,61,64,67] In most of the Raman scattering studies of $K_xFe_{2-y}Se_2$ single crystals, the phonon spectra with large number of modes are obtained, confirming the fact that Fe vacancy order reduces locally the symmetry to *I4/m*.[28,61,74–76] These spectra are very similar to each other; characteristic $K_xFe_{2-y}Se_2$ Raman spectrum is shown in Fig. 6. However, the symmetry analysis of the phonon spectra was performed assuming the different space groups in various papers. Temperature analysis of Raman spectra, as well as the line shape of some modes, also differs, as will be discussed.

First Raman study of $K_xFe_{2-y}Se_2$ was done by Zhang *et al.*[74] They assumed the *I4/m* space group for the single phase and thus assigned phonons which appeared in the parallel polarization configuration only as A_g symmetry modes, whereas those modes appearing in both polarization configurations were assigned as B_g ones. In that way 6 A_g and 5 B_g modes were assigned, with energies coinciding well with the lattice dynamics calculations. The most intriguing fact is a frequency jump at T_c for the Raman mode appearing at about 180 cm^{-1} in parallel polarization configuration, of unknown origin, since its energy did not match with any of the calculated A_g mode energies. Authors interpreted this behaviour as an evidence of specific connection between phonons and SC. This hardening was also observed,[75] where Raman spectra of three SC ($K_{0.8}Fe_{1.6}Se_2$, $Tl_{0.5}K_{0.3}Fe_{1.6}Se_2$ and $Tl_{0.5}Rb_{0.3}Fe_{1.6}Se_2$) and one non-SC sample ($KFe_{1.5}Se_2$) were analyzed in terms of *I4/m* space group (Fig. 7). It is suggested that this mode is local, originating from the nanoscopic region of filled Fe vacancies. By comparing the Raman spectra of $K_{0.8}Fe_{1.6}Se_2$ and $KFe_{1.5}Se_2$ single crystals, frequency shift of the Raman modes originating from Fe- and Se-ion vibrations was observed, due to the differences in the FeSe plane induced by the change of Fe content. Doping on the K site did not influence phonon spectra above 60 cm^{-1}, but induces additional modes in the low energy range, attributed to the change of local symmetry in the K layer.[75] *I4/m* space group is assumed also for $K_xFe_{2-y}Se_2$.[76] 16 Raman modes at room temperature was observed, some of them with Fano line shape, attributed to the coupling of the vibrations with AFM spin fluctuations. Authors agreed that three new phonon modes appear below 250 K, due to the structural transition, *i.e.* symmetry lowering from the *I4/m* to the *I4* phase.[76]
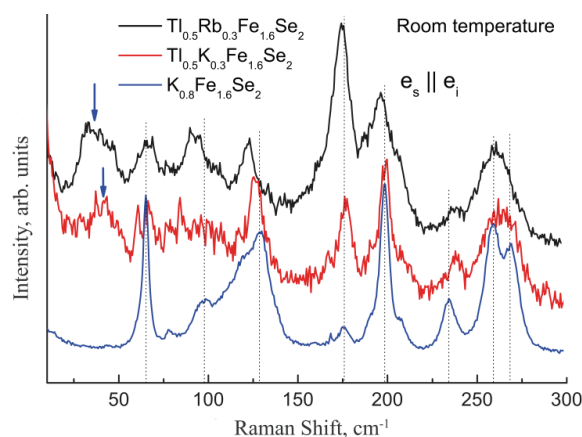
Fig. 7. Raman spectra of the three superconducting crystals measured at room temperature. Additional modes, appearing below 60 cm^{-1} in the Tl- and Rb-substituted samples, are denoted by blue arrows. Dotted lines are guides indicating the peak positions.[75] (Reprinted with permission from Ref. 75, copyright (2012) by the American Physical Society).

Unlike to the presentations by some authors,[74–76] Raman spectra of $K_xFe_{2-y}Se_2$ were analyzed[28,61] in terms of both *I4/m* and *I4/mmm* space groups. Raman modes from the *I4/mmm* space group were assigned.[28] It was determined that the A_{1g} mode appears at about 180 cm^{-1}, whereas energy of the B_{1g} mode is 207 cm^{-1}. It is interesting to note that this A_{1g} phonon is probably the same Raman mode as that of the unknown origin,[74,75] with frequency jump at T_c. Large number of modes from the low symmetry *I4/m* phase were assigned[28] by means of detailed symmetry analysis and measurements in various polarization configurations. A_g and B_g mode energies coincide with other data,[74] which can be seen from Table II. Detailed temperature-dependent Raman scattering study of SC $K_xFe_{2-y}Se_2$ and non-SC $K_xFe_{1.8}Co_{0.2}Se_2$ is given.[61] Similar spectra of the two crystals indicate that phase separation is preserved with small amount of Co doped at the Fe-site. Analysis of the temperature-dependent Raman spectra revealed the phonon energies temperature dependence is dominantly driven by the lattice thermal expansion, whereas the impact of phonon anharmonicity is negligible. The renormalization of the A_{1g} phonon energy below T_c was observed only for the SC sample (Fig. 8), which led to the conclusion that it is induced by the SC gap opening, in line with the theoretically expected behaviour.[77]

Room temperature Raman spectra of Ni- and Co-doped $K_xFe_{2-y}Se_2$ crystals give valuable insight into the structural changes of $K_xFe_{2-y}Se_2$ with doping. Recent Raman studies[59,60] revealed that increasing Co and Ni content have similar influence on phonon spectra of these materials. When Ni (Co) content is low, large number of modes are present in Raman spectra (Fig. 9), in accordance with the symmetry lowering due to the Fe-vacancy ordering, *i.e.*, presence of *I4/m* phase,

TABLE II. Comparison of experimentally observed wavenumbers (in cm^{-1}) at room temperature for the selected A_g and B_g symmetry modes of $K_xFe_{2-y}Se_2$ single crystals[28,74]

Ref.	A_g^4	A_g^6	A_g^8	B_g^7	B_g^8
28	134	203	264	214	274
74	134.6	202.9	264.6	214.3	274.9
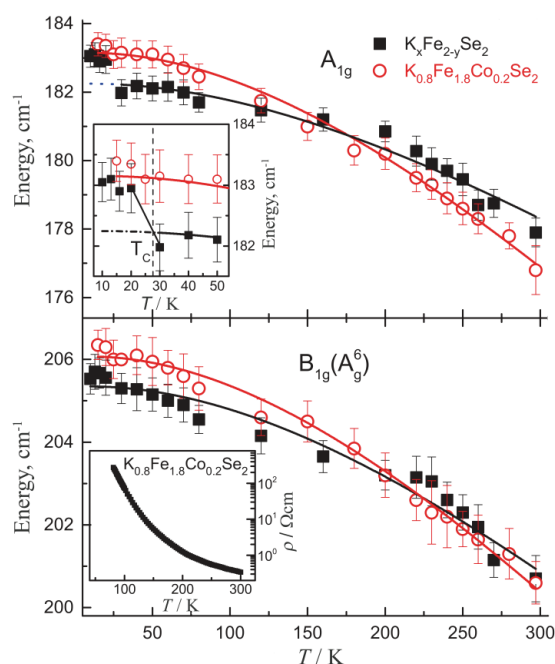
Fig. 8. Temperature dependence of A_{1g} and B_{1g} mode energy in $K_xFe_{2-y}Se_2$ and $K_{0.8}Fe_{1.8}Co_{0.2}Se_2$ single crystals. Inset: An enlarged view of A_{1g} temperature dependence in a low temperature region near T_c.[61]

as in pure $K_xFe_{2-y}Se_2$.[28] Broad asymmetric structures, appearing in Raman spectra of both series of samples for the intermediate Ni (Co) concentrations, were attributed to the large structural disorder. At high Ni (Co) concentrations, as well as for pure $K_xNi_{2-y}Se_2$[67] and $K_xCo_{2-y}Se_2$,[64] only two modes can be observed in Raman spectra, confirming the lack of any vacancy order. Appearance of the A_{1g} mode in the whole series gives a clear evidence that *I4/mmm* phase persists for all Ni (Co) concentrations.[59,60] Detailed Raman scattering studies of $K_xNi_{2-y}Se_2$[67] and $K_xCo_{2-y}Se_2$ single crystals[64] support the findings given elsewhere.[59,60] As opposed to the A_{1g} phonon that appears at similar energies in these two compounds,[64,67] the B_{1g} phonon energy (representing vibrations of the transition metal ions) differs substantially (Table III). Besides that, by measuring from the (010)-plane of $K_xNi_{2-y}Se_2$, one E_g mode is clearly observed (Fig. 10) whereas the other, low intensity E_g mode, was confirmed by numerical calculations. Large intrinsic line-
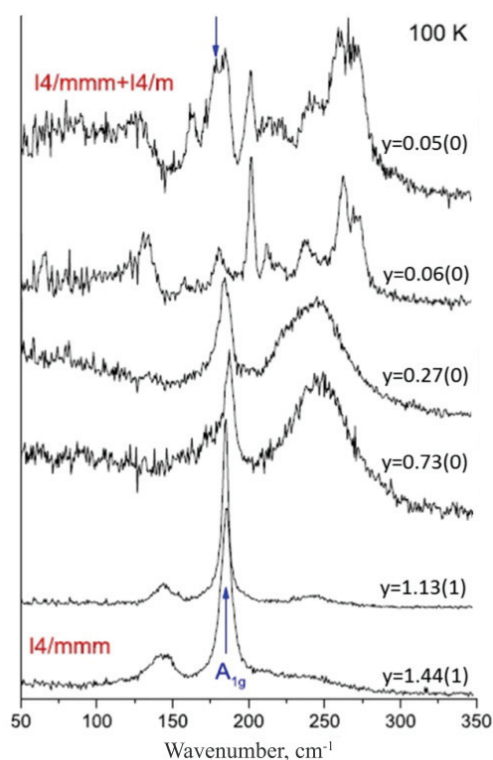
Fig. 9. Raman spectra of $K_xFe_{2-x-y}Ni_ySe_2$ single crystal series measured from the (001)-plane at 100 K.[59]

width of the B_{1g} phonon, together with the mode asymmetry, is believed to originate from the structural disorder, although the impact of the electron–phonon interaction cannot be excluded.[67] Similar features of the B_{1g} phonon are also observed in $K_xCo_{2-y}Se_2$, where it was argued that they are mainly caused by the spin fluctuations coupled to the electronic structure *via* lattice vibrations.[64] Temperature dependence of A_{1g} and B_{1g} mode energy in $K_xCo_{2-y}Se_2$ in the paramagnetic phase is governed by the lattice thermal expansion and phonon anharmonicity, whose relative importance is not yet firmly established. Change of phonon linewidths is well described with the lattice anharmonicity model. Both phonon modes have energy jump below the FM transition temperature T_c, but the A_{1g} mode exhibits sharpening with further cooling, whereas the B_{1g} mode broadens (Fig. 11). Sudden frequency change of the observed Raman mode energies as the sample gets magnetized can occur due to the magnetostriction effects, spin-phonon coupling and/or changes in the electron–phonon interaction caused by the spin polarization and changes in the electronic spectrum.[64]

As opposed to $K_x(Co, Ni)_{2-y}Se_2$, phonon spectra of $K_{0.88}Fe_{1.63}S_2$ consists of large number of modes, originating from the *I4/m* phase. This confirms symmetry lowering due to the Fe-vacancy order, but without phase separation, unlike the

$K_xFe_{2-y}Se_2$.[78] 6 A_g and 8 B_g modes were assigned by measuring the spectra from the (001)-plane of the sample.

TABLE III. Experimentally obtained energies of the A_{1g} and B_{1g} Raman modes (in cm^{-1}) at room temperature for $K_xM_{2-y}Se_2$ single crystals (M = Fe, Co or Ni)

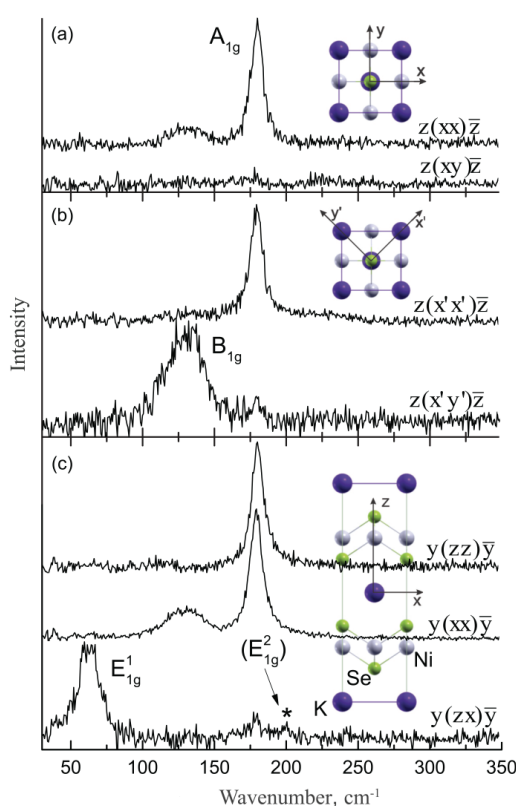| Wave number	$K_xFe_{2-y}Se_2$[28]	$K_xCo_{2-y}Se_2$[64]	$K_xNi_{2-y}Se_2$[67]
$\omega(A_{1g})$	180	197	178
$\omega(B_{1g})$	207	187	134

Fig. 10. Room temperature Raman spectra of $K_{0.95}Ni_{1.86}Se_2$ single crystals measured in various scattering configurations ($\mathbf{x}$ = [100], $\mathbf{y}$ = [010], $\mathbf{x'}$ = = $1/\sqrt{2}$ [110], $\mathbf{y'}$ = $1\sqrt{2}$ /[1 1 0], $\mathbf{z}$ = = b[001]).[67]

4. IRON-BASED SPIN-LADDER MATERIALS

4.1. Crystal structure

The most studied materials among the iron-containing spin-ladder compounds with the general formula AFe_2X_3 (A = K, Rb, Cs, Ba and X = Ch) are barium–iron-chalcogenides, $BaFe_2(S,Se)_3$. The ladder structure of these compounds can be considered as obtained by cutting the layers of edge-sharing $FeSe_4$ tetrahedra of the two-dimensional 11-iron chalcogenides, *i.e.*, removing every third Fe atom from the FeSe layers. $BaFe_2(S,Se)_3$ crystals consists of one-dimensional
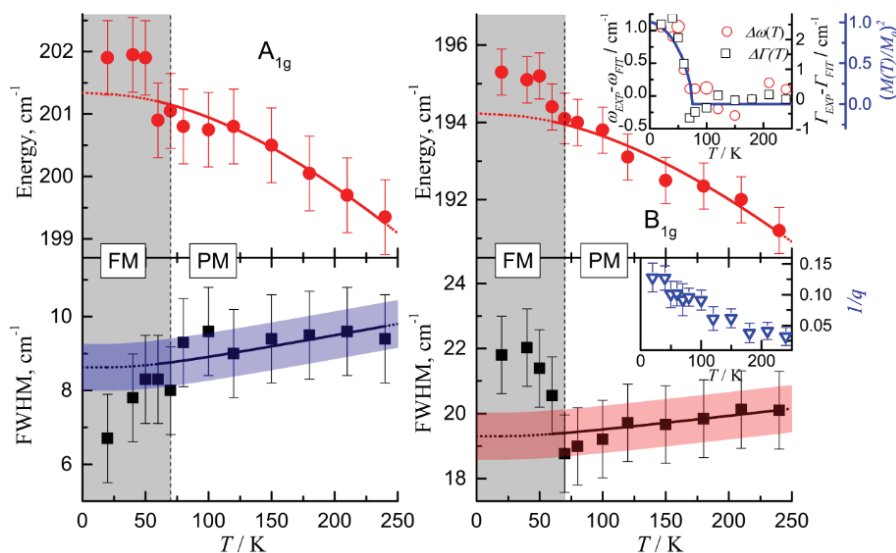
Fig. 11. Temperature dependence of the energy and linewidth (FWHM) for the A_{1g} and B_{1g} Raman modes of $K_xCo_{2-y}Se_2$ single crystal. Solid lines are the theoretical fits which take into account lattice thermal expansion and phonon–phonon scattering for energy and linewidth temperature dependence, respectively. The dotted lines are the extrapolation to 0 K. Shaded area denotes temperature range of the ferromagnetic phase. Inset of B_{1g} energy: temperature dependence of the B_{1g} mode frequency, compared with $(M(T)/M(0))^2$ curve. Inset of B_{1g} FWHM: measure of the electron–phonon coupling ($1/q$) of the B_{1g} mode as a function of temperature.[64]

$[Fe_2(S,Se)_3]^{2-}$ double chains, propagating along the long ladder direction („lag'') and Ba^{2+} as separators (Fig. 12). In $BaFe_2S_3$ the double chains extend along the *a*-axis, whereas in $BaFe_2Se_3$ the ladder lag is along the *b*-axis.[33,79] There are two important structural differences between these two materials. Namely, two different Fe–Fe distances along the ladder lag exist in $BaFe_2Se_3$, whereas in $BaFe_2S_3$ all Fe–Fe distances are the same. Moreover, $[Fe_2Se_3]^{2-}$ double chains are tilted off the *bc*-plane, with opposite tilting directions of the two neighbouring layers, whereas in $BaFe_2S_3$ there is no tilting. Due to the slight structural differences, $BaFe_2Se_3$ and $BaFe_2S_3$ crystals, although both orthorhombic, are not isostructural. $BaFe_2S_3$ has *Cmcm* space group, whereas space group of $BaFe_2Se_3$ is *Pnma*, both with four formula units per unit cell.[79]

$BaFe_2Se_2O$ is the first layered iron-oxychalcogenide with alkali earth metal. It consists of Fe–Se(O) layers and Ba^{2+}, stacked alternatively along the *c*-axis, similar with $BaFe_2Se_3$ and $BaFe_2S_3$. Fe–Se(O) double chains are bridged by the oxygen atoms along the *a*-axis and propagate along the *b*-axis. However, the intralayer structure differs from those in previously described spin-ladder materials. Different Fe–Se and Fe–O distances cause Fe atoms to be located in highly dis-

torted (asymmetric) tetrahedra, whose angle significantly deviates from the ideal value. Crystal structure is orthorombic (*Pmmn* space group), with two formula units per unit cell.[80]
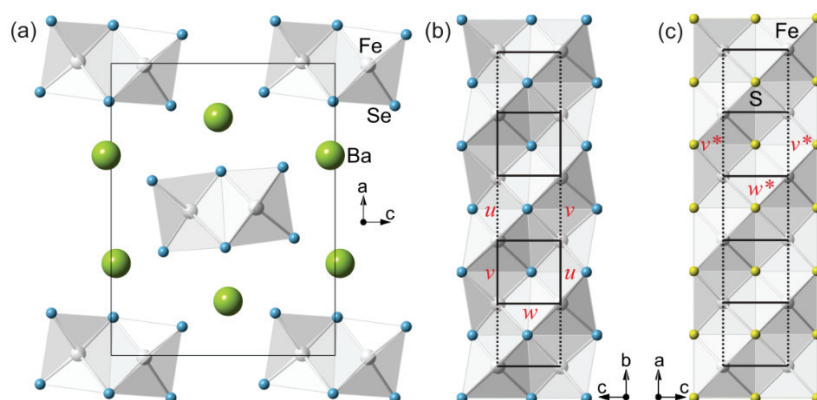

Fig. 12. Crystal structure of $BaFe_2Se_3$ and $BaFe_2S_3$. a) Projection of the $BaFe_2Se_3$ crystal in the (010)-plane; b) double chain of $[Fe_2Se_3]^{2-}$ tetrahedra propagating along the *b*-axis; c) $[Fe_2S_3]^{2-}$ double chain in the (010) plane. *w* and w^* denote Fe–Fe distances along short ladder directions ("rungs"), whereas *u*, *v* and v^* represent Fe–Fe distances along the ladder legs.[81]

4.2. Physical properties

$BaFe_2S_3$ has semiconducting $\rho(T)$, with very low resistivity.[82,83] The change of slope in resistivity occurs at about 275 K,[82] where inverse molar magnetic susceptibility has a broad hump.[83] This material also exhibits negative magnetoresistive effect of about 10 % at low temperatures. The divergence between ZFC (zero field-cooled) and and FC (field-cooled) magnetic susceptibility below 25 K points out to the spin-glass behaviour, which is confirmed by other measurements.[83] Strong intrachain AFM coupling of the ions, together with the additional crystal field splitting due to the neighbouring Fe atoms and direct Fe–Fe interactions cause ground state with $S = 0$.[83] Takahashi *et al.*[30] recently measured the resistivity of $BaFe_2S_3$ single crystals under various pressures and found the gradual suppression of insulating behaviour with increasing pressure, with metal––insulator transition at about 11 GPa. With further increasing pressure, this material exhibits SC below $T_c = 14$ K. The increased metallicity of the sample at higher pressures is caused by the anisotropic compression of the crystal.[30] NPD measurements indicate the stripe-type magnetic order, with magnetic moment 1.2 μ_B (at 4 K) per Fe site. These moments form FM units along the rung direction, whereas these units order antiferromagnetically along the lag direction.[30]

$BaFe_2Se_3$ single crystal also has semiconducting $\rho(T)$ properties, similar to $BaFe_2S_3$, but without magnetoresistive effect.[33] Large diversity of susceptibilities for different field directions indicatesmagnetic anisotropy.[29,33] The transition in

magnetic susceptibility at 255 K for all field directions is attributed to the crossover from short-range to long-range AFM order.[33] This transition was not observed,[29] since a divergence of ZFC and FC magnetic susceptibilities is attributed to the spin-glass behavior with $T_f \approx 50$ K.

Resistivity measurements on $BaFe_2Se_2O$ single crystals revealed the insulating behaviour. At $T_a = 240$ K, there is anomaly in resistivity, allowing their fitting below T_a with the relation $\rho = \rho_0 \exp\{(E_a/k_BT)^\alpha\}$, $\alpha < 1$, which means that thermal activation is less effective at low temperatures and the other mechanism is responsible for electron trapping.[80] Authors proposed the existence of long range AFM order below 240 K, which is confirmed by the strong peak in differential magnetic susceptibility $\partial\chi/\partial T$ at T_a. Anisotropy in the magnetic susceptibility indicates that the easy axis of magnetization is in the ab-plane. Besides that, a sudden decrease of susceptibility below 115 K, with much less anisotropy, was attributed to the spin-singlet dimers, believed to be formed at low temperatures.[80] All iron ions in $BaFe_2Se_2O$ are in Fe^{2+} state and high spin state, and this compound can be considered as $S = 2$ spin-ladder system, with the dominant AFM superexchange interaction along the ladder rungs.[32]

4.3. Raman scattering studies

Raman spectra of $BaFe_2Se_2O$ were analysed.[31] In the optical part of the spectra 6 (of 6) A_g modes and 2 out of 2 B_{1g} modes were observed and assigned (Fig. 13) whereas the remaining modes (of B_{2g} and B_{3g} symmetry) could not be observed by measuring from the (001)-plane of the sample. Three new modes appearing below $T_N = 240$ K are attributed to the crystal structure and/or crystal symmetry change. Analysis of the Raman mode energy and linewidth depend-
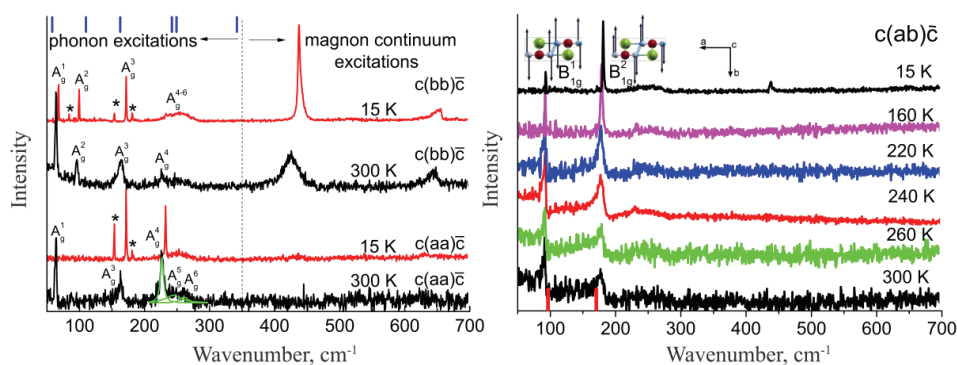

Fig. 13. Left: the (aa) and (bb) polarized Raman spectra of $BaFe_2Se_2O$ single crystals measured at room temperature and at 15 K. Vertical bars denote calculated values of the A_g Raman active modes. New modes appearing below 240 K are denoted by asterisks. Right: the (ab) polarized Raman spectra of $BaFe_2Se_2O$ single crystals measured at various temperatures. Vertical bars denote calculated values of the B_{1g} symmetry modes. Insets show normal modes of the two B_{1g} symmetry vibrations.[31]

ence on temperature showed significant hardening and narrowing of A_g modes below T_N. B_{1g} modes asymmetry above T_N (persisting in the region of short-range magnetic order) is believed to originate from the spin fluctuations.[31]

Besides the optical phonon modes, two broad and asymmetric structures appear in the Raman spectra of $BaFe_2Se_2O$ single crystals at higher energies, in $c(bb)\bar{c}$ polarization only (which coincides with the spin orientations). Therefore, they are assigned as two-magnon continuum modes.[31] These structures are shown in Fig. 14. From the ratio $T_N/T_{max} = 0.53$ (where T_{max} denotes temperature where magnetic susceptibility has a maximum), it was concluded that $BaFe_2Se_2O$ is a quasi-2D magnetic system. From the onset of the magnetic continuum, which should correspond to $2\Delta_S$ (where Δ_S is a spin gap energy), it was estimated $\Delta_S \approx$ ≈ 27 meV. Magnon modes disappear above 623 K, $e.g.$, 2.6 T_N[31] in agreement with the other results indicating that the short-range magnetic order in oxychalcogenides persists at least up to 2 T_N.[84]
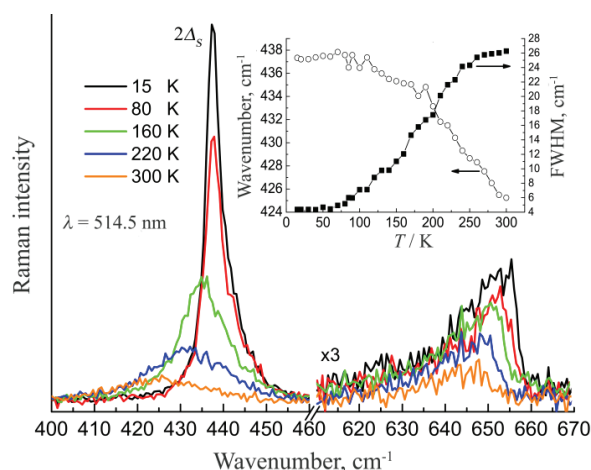

Fig. 14. Raman scattering spectra of $BaFe_2Se_2O$ single crystals measured at various temperatures between 15 and 300 K in $c(bb)\bar{c}$ polarization configuration. Only 400–670 cm^{-1} spectral range is shown. Inset: energy (circles) and linewidth (squares) of the $2\Delta_S$ (spin gap) mode as a function of temperature.[31]

Phonon properties of $BaFe_2S_3$ and $BaFe_2Se_3$ were analysed.[81] By measuring from the (110)-plane of the $BaFe_2S_3$ sample, in parallel polarization configurations 5 (of 5) A_g symmetry modes and 5 out of 6 B_{1g}, the symmetry modes were clearly observed. In crossed polarization configuration B_{2g} and B_{3g} modes could appear in the Raman spectra; therefore, the assignation was done with the help of lattice dynamics calculations. Three such modes were observed in phonon spectra.

On the other hand, lower symmetry of $BaFe_2Se_3$ single crystals compared to $BaFe_2S_3$, caused more Raman active modes to be observed in the phonon spectra. Indeed, by measuring from the (100)-plane of the sample, 9 (of 11) A_g symmetry

modes were observed in parallel polarization configuration, whereas in the crossed one three additional modes were assigned as of B_{3g} symmetry.[81]

The temperature analysis of phonon energy and linewidth was performed in terms of lattice thermal expansion and phonon anharmonicity for both $BaFe_2S_3$ and $BaFe_2Se_3$ single crystals. It turned out that the contribution of the phonon––phonon scattering to the Raman mode energy temperature dependence is negligible. The sudden change of slope of energy and linewidth temperature dependence of the A_g^4 mode at about 275 K (where the hump in inverse molar magnetic susceptibility and change of slope in resistivity also occur) in $BaFe_2S_3$ is attributed to the AFM spin ordering within the ladder lag from the short-range to the long-range state, without spin ordering of the whole crystal, followed by the change in the electronic structure. The energies of the all analyzed modes in $BaFe_2Se_3$ sharply increase below T_N, which was ascribed to the spin–phonon coupling. This mechanism is also responsible for the deviation from the usual anharmonic behaviour of the phonon linewidth.[81]

5. SUMMARY AND CONCLUSIONS

The results discussed in this review clearly demonstrate that Raman spectroscopy is a very powerful technique for investigating the vibrational properties of iron chalcogenides. Moreover, almost all structural and magnetic transitions leave a clear fingerprint on the vibrational spectra of 11, 122* and spin-ladder iron-based superconductors, reviewed in this article, through the appearance of new phonon modes or a sudden change in the phonon energy and/or linewidth.

Raman spectra of Fe(Te, Se) single crystals measured from the *ab*-plane consist of two modes, assigned as A_{1g} and B_{1g} ones. Magnetic transition in FeTe causes softening and narrowing of the B_{1g} (Fe) mode. With Se doping of FeTe crystals the A_{1g} mode hardens and narrows, whereas the B_{1g} ones softens and broadens, compared to the pure FeTe. Large B_{1g} mode hardening observed for FeSe is explained as a consequence of the dynamical crossover between different Fe spin states. Electronic nematic fluctuations leave a fingerprint through highly polarized quasielastic response in the Raman spectra of FeSe in the tetragonal phase.

Vibrational spectra of $K_xFe_{2-y}Se_2$ single crystals have large number of phonon peaks. Some authors assigned them according only to the *I4/m* space group, whereas the others assume the existence of *I4/mmm* and *I4/m* phases, which is confirmed by the other techniques. Renormalization of the A_{1g} mode energy at T_c in SC $K_xFe_{2-y}Se_2$ and the absence of renormalization in non-SC isostructural $K_xFe_{1.8}Co_{0.2}Se_2$ indicates that it is induced by the opening of SC gap, confirming that this mode indeed represents the *I4/mmm* phase vibration. Raman studies also revealed that doping of $K_xFe_{2-y}Se_2$ single crystals with different amount of Co and Ni significantly affects their crystal structure. When Ni (Co) content is low, large number of modes points out to the presence of both *I4/mmm* and *I4/m*

phases. At high dopant concentrations, as well as for pure $K_x(Co, Ni)_{2-y}Se_2$, only two modes, of A_{1g} and B_{1g} symmetry, appear in phonon spectra, confirming the lack of ordered vacancies. Spin-dependent electron-phonon coupling and magnetostriction effects leave a clear fingerprint on the vibrational spectra of $K_xCo_{2-y}Se_2$, through a strong deviations of the phonon energy and the linewidth temperature dependence from the anharmonic behaviour.

The magnetic ordering manifests itself through the impact on energy, linewidth and lineshape of the observed phonon modes of spin-ladder iron-based systems $BaFe_2S_3$, $BaFe_2Se_3$ and $BaFe_2Se_2O$. Besides that, the analysis of the two-magnon continuum modes of $BaFe_2Se_2O$ allows the estimation of the spin gap energy and classification of this material as a quasi-2D magnetic system.

Future work could be concentrated on the high pressure Raman scattering studies, as well as on the investigations of possible new materials from this class that will be produced by the doping of the existing ones. The results presented in this paper show that Raman spectroscopy is an invaluable tool which can expand our knowledge of the fundamental properties of iron chalcogenides.

И З В О Д
ДИНАМИКА РЕШЕТКЕ ГВОЖЂЕ-ХАЛКОГЕНИДА – ИСПИТИВАЊА МЕТОДОМ РАМАНОВЕ СПЕКТРОСКОПИЈЕ

МАРКО Р. ОПАЧИЋ[1,2] и НЕНАД Ж. ЛАЗАРЕВИЋ[2]

[1]*Електротехнички факултет Универзитета у Београду, Булевар краља Александра 73, Београд* и[2]*Центар за физику чврстог стања и нове материјале, Институт за физику, Прегревица 118, Београд*

Откриће суперпроводног кристала FeSe значило је појаву нове подкласе високотемпературских суперпроводника – гвожђе-халкогенида. Материјали из ове групе имају разна специфична својства, од суперпроводљивости са релативно високим критичним температурама до нискодимензионалних магнетних особина. Овај прегледни рад приказује најважније резултате везане за гвожђе-халкогениде, са посебним нагласком на њихове вибрационе особине, испитиване методом Раманове спектроскопије. Раманови спектри гвожђе-халкогенида у зависности од температуре и допирања пружају значајан увид у комплексне везе између вибрационих, електронских и магнетних особина ових материјала. Резултати приказани у овом прегледном раду показују да Раманова спектроскопија пружа нове информације које могу значајно побољшати разумевање фундаменталних својстава гвожђе-халкогенида.

REFERENCES

1. H. Kamerlingh Onnes, *Commun. Phys. Lab. Univ. Leiden* **120b** (April 1911), reprinted in *Proc. K. Ned. Akad. Wet.* **13** (1911) 1274
2. A. W. Sleight, J. L. Gillson, P. E. Bierstedt, *Solid State Commun.* **17** (1975) 27
3. J. G. Bednorz, K. A. Müller, *Z. Angew. Phys., B* **64** (1986) 189

4. C. W. Chu, P. H. Hor, R. L. Meng, L. Gao, Z. J. Huang, Y. Q. Wang, *Phys. Rev. Lett.* **58** (1987) 908
5. C. W. Chu, P. H. Hor, R. L. Meng, L. Gao, Z. J. Huang, *Science* **235** (1987) 567
6. M. A. Kastner, R. J. Birgeneau, G. Shirane, Y. Endoh, *Rev. Mod. Phys.* **70** (1998) 897
7. P. A. Lee, N. Nagaosa, X.-G. Wen, *Rev. Mod. Phys.* **78** (2006) 17
8. E. Dagotto, *Rev. Mod. Phys.* **66** (1994) 763
9. P. Monthoux, A. V. Balatsky, D. Pines, *Phys. Rev. Lett.* **67** (1991) 3448
10. D. J. Scalapino, *Phys. Rep.* **250** (1995) 329
11. C. C. Tsuei, J. R. Kirtley, C. C. Chi, Lock-See Yu-Jahnes, A. Gupta, T. Shaw, J. Z. Sun, M. B. Ketchen, *Phys. Rev. Lett.* **73** (1994) 593
12. Y. Kamihara, H. Hiramatsu, M. Hirano, R. Kawamura, H. Yanagi, T. Kamiya, H. Hosono, *J. Am. Chem. Soc.* **128** (2006) 10012
13. Y. Kamihara, T. Watanabe, M. Hirano, H. Hosono, *J. Am. Chem. Soc.* **130** (2008) 3296
14. Z.-A. Ren, G.-C. Che, X.-L. Dong, J. Yang, W. Lu, W. Yi, X.-L. Shen, Z.-C. Li, L.-L. Sun, F. Zhou, *Europhys. Lett.* **83** (2008) 17002
15. M. Rotter, M. Tegel, D. Johrendt, *Phys. Rev. Lett.* **101** (2008) 107006
16. X. C. Wang, Q. Q. Liu, Y. X. Lv, W. B. Gao, L. X. Yang, R. C. Yu, F. Y. Li, C. Q. Jin, *Solid State Commun.* **148** (2008) 538
17. M. D. Lumsden, A. D. Christianson, *J. Phys.: Condens. Matter* **22** (2010) 203203
18. D. C. Johnston, *Adv. Phys.* **59** (2010) 803
19. H. Chen, Y. Ren, Y. Qiu, Wei Bao, R. H. Liu, G. Wu, T. Wu, Y. L. Xie, X. F. Wang, Q. Huang, X. H. Chen, *Europhys. Lett.* **85** (2009) 17006.
20. I. I. Mazin, D. J. Singh, M. D. Johannes, M. H. Du, *Phys. Rev. Lett.* **101** (2008) 057003
21. A. D. Christianson, E. A. Goremychkin, R. Osborn, S. Rosenkranz, M. D. Lumsden, C. D. Malliakas, I. S. Todorov, H. Claus, D. Y. Chung, M. G. Kanatzidis, R. I. Bewley, T. Guidi, *Nature* **456** (2008) 930
22. F.-C. Hsu, J.-Y. Luo, K.-W. Yeh, T.-K. Chen, T.-W. Huang, P.-M. Wu, Y.-C. Lee, Y.-L. Huang, Y.-Y.Chu, D.-C. Yan, M.-K. Wu, *Proc. Natl. Acad. Sci. U.S.A.* **105** (2008) 14262
23. M. H. Fang, H. M. Pham, B. Qian, T. J. Liu, E. K. Vehstedt, Y. Liu, L. Spinu, Z. Q. Mao, *Phys. Rev., B* **78** (2008) 224503
24. S. Margadonna, Y. Takabayashi, Y. Ohishi, Y. Mizuguchi, Y. Takano, T. Kagayama, T. Nikagawa, M. Takata, K. Prassides, *Phys. Rev., B* **80** (2009) 064506
25. J. Guo, S. Jin, G. Wang, S. Wang, K. Zhu, T. Zhou, M. He, X. Chen, *Phys. Rev., B* **82**(2010) 180520
26. W. Bao, Q. Huang, G. F. Chen, M. A. Green, D. M. Wang, J. B. He, X. Q. Wang, Y. Qiu, *Chin. Phys. Lett.* **28** (2011) 086104
27. W. Li, H. Ding, P. Deng, K. Chang, C. Song, K. He, L. Wang, X. Ma, J.-P. Hu, X. Chen, Q.-K. Xue, *Nat. Phys.* **8** (2012) 126
28. N. Lazarević, M. Abeykoon, P. W. Stephens, H. Lei, E. S. Bozin, C. Petrovic, Z. V. Popović, *Phys. Rev., B* **86** (2012) 054503
29. B. Saparov, S. Calder, B. Sipos, H. Cao, S. Chi, D. J. Singh, A. D. Christianson, M. D. Lumsden, A. S. Sefat, *Phys. Rev., B* **84** (2011) 180409
30. H. Takahashi, A. Sugimoto, Y. Nambu, T. Yamauchi, Y. Hirata, T. Kawakami, M. Avdeev, K. Matsubayashi, F. Du, C. Kawashima, H. Soeda, S. Nakano, Y. Uwatoko, Y. Ueda, T. J. Sato, K. Ohgushi, *Nat. Mater.* **14** (2015) 1008
31. Z. V. Popović, M. Šćepanović, N. Lazarević, M. M. Radonjić, D. Tanasković, H. Lei, C. Petrovic, *Phys. Rev., B* **89** (2014) 014301

32. H. Kabbour, E. Janod, B. Corraze, M. Danot, C. Lee, M. H. Whangbo, L. Cario, *J. Am. Chem. Soc.* **130** (2008) 8261
33. H. Lei, H. Ryu, A. I. Frenkel, C. Petrovic, *Phys. Rev., B* **84** (2011) 214511
34. N. Lazarević, E. S. Bozin, M. Šćepanović, M. Opačić, H. Lei, C. Petrovic, Z. V. Popović, *Phys. Rev., B* **89** (2015) 224301
35. N. Lazarević, Z. V. Popović, R. Hu, C. Petrovic, *Phys. Rev., B* **83** (2011) 024302
36. N. Lazarević, Z. V. Popović, R. Hu, C. Petrovic, *Phys. Rev., B* **81** (2010) 144302
37. S. Margadonna, Y. Takabayashi, M. T. McDonald, K. Kasperkiewicz, Y. Mizuguchi, Y. Takano, A. N. Fitch, E. Suarde, K. Prassides, *Chem. Commun.* (2008) 5607
38. A. Martinelli, A. Palenzona, M. Tropeano, C. Ferdeghini, M. Putti, M. R. Cimberle, T. D. Nguyen, M. Affronte, C. Ritter, *Phys. Rev., B* **81** (2010) 094115
39. V. Gnezdilov, Y. G. Pashkevich, P. Lemmens, D. Wulferding, T. Shevtsova, A. Gusev, D. Chareev, A. Vasiliev, *Phys. Rev., B* **87** (2013) 114305
40. T. M. McQueen, A. J. Williams, P. W. Stephens, J. Tao, Y. Zhu, V. Ksenofontov, F. Casper, C. Felser, R. J. Cava, *Phys. Rev. Lett.* **103** (2009) 057002
41. S.-H. Baek, D.V. Efremov, J. M. Ok, J. S. Kim, Jeroen van den Brink, B. Büchner, *Phys. Rev., B* **93** (2016) 180502(R)
42. S. Li, C. de la Cruz, Q. Huang, Y. Chen, J. W. Lynn, J. Hu, Y.-L. Huang, F.-C. Hsu, K.-W. Yeh, M.-K. Wu, P. Dai, *Phys. Rev., B* **79** (2009) 054503
43. Y.Mizuguchi, F.Tomioka, S.Tsuda, T.Yamaguchi, and Y.Takano, *J. Phys. Soc. Jpn.* **78** (2009) 074712
44. Qisi Wang, Yao Shen, Bingying Pan, Xiaowen Zhang, K. Ikeuchi, K. Iida, A. D. Christianson, H. C. Walker, D. T. Adroja, M. Abdel-Hafiez, Xiaojia Chen, D. A. Chareev, A. N. Vasiliev, Jun Zhao, *Nat. Commun.* **7** (2016) 12182
45. S-H. Baek, D. V. Efremov, J. M. Ok, J. S. Kim, Jeroen van den Brink, B. Büchner, *Nat. Mater.* **14** (2015) 210
46. M. D. Watson, T. K. Kim, A. A. Haghighirad, N. R. Davies, A. McCollam, A. Narayanan, S. F. Blake, Y. L. Chen, S. Ghannadzadeh, A. J. Schofield, M. Hoesch, C. Meingast, T. Wolf, A. I. Coldea, *Phys. Rev., B* **91** (2015) 155106
47. W. Bao, Y. Qiu, Q. Huang, M. A. Green, P. Zajdel, M. R. Fitzsimmons, M. Zhernenkov, S. Chang, M. H. Fang, B. Qian, E. K. Vehstedt, J. Yang, H. M. Pham, L. Spinu, Z. Q. Mao, *Phys. Rev. Lett.* **102** (2009) 247001
48. V. Gnezdilov, Y. Pashkevich, P. Lemmens, A. Gusev, K. Lamonova, T. Shevtsova, I. Vitebskiy, O. Afanasiev, S. Gnatchenko, V. Tsurkan, J. Deisenhofer, A. Loidl, *Phys. Rev., B* **83** (2011) 245127
49. T.-L. Xia, D. Hou, S. C. Zhao, A. M. Zhang, G. F. Chen, J. L. Luo, N. L. Wang, J. H. Wei, Z.-Y. Lu, Q. M. Zhang, *Phys. Rev., B* **79** (2009) 140510
50. Y. J. Um, A. Subedi, P. Toulemonde, A. Y. Ganin, L. Boeri, M. Rahlenbeck, Y. Liu, C. T. Lin, S. J. E. Carlsson, A. Sulpice, M. J. Rosseinsky, B. Keimer, M. Le Tacon, *Phys. Rev., B* **85**(2012) 064519
51. K. Okazaki, S. Sugai, S. Niitaka, H. Takagi, *Phys. Rev., B* **83** (2011) 035103
52. Z. V. Popović, N. Lazarević, S. Bogdanović, M. M. Radonjić, D. Tanasković, Rongwei Hu, Hechang Lei, C. Petrovic, *Solid State Commun.* **193** (2014) 51
53. P. Massat, D. Farina, I. Paul, S. Karlsson, P. Strobel, P. Toulemonde, M.-A. Measson, M. Cazayous, A. Sacuto, S. Kasahara, T. Shibauchi, Y. Matsuda, Y. Gallais, *Proc. Natl. Acad. Sci. U.S.A.* **113** (2016) 9177

54. Yuwen Hu, Xiao Ren, Rui Zhang, Huiqian Luo, Shigeru Kasahara, Tatsuya Watashige, Takasada Shibauchi, Pengcheng Dai, Yan Zhang, Yuji Matsuda, Yuan Li, *Phys. Rev., B* **93** (2016) 060504(R)
55. P. Zavalij, W. Bao, X. F. Wang, J. J. Ying, X. H. Chen, D. M. Wang, J. B. He, X. Q. Wang, G. F. Chen, P.-Y. Hsieh, Q. Huang, M. A. Green, *Phys. Rev., B* **83** (2011) 132509
56. Z. Wang, Y. J. Song, X. L. Shi, Z. W. Wang, Z. Chen, H. F. Tian, G. F. Chen, J. G. Guo, H. X. Yang, J. Q. Li, *Phys. Rev., B* **83** (2011) 140505(R)
57. F. Ye, S. Chi, W. Bao, X. F. Wang, J. J. Ying, X. H. Chen, H. D. Wang, C. H. Dong, M. H. Fang, *Phys. Rev. Lett.* **107** (2011) 137003
58. F. Chen, M. Xu, Q. Q. Ge, Y. Zhang, Z. R. Ye, L. X. Yang, Juan Jiang, B. P. Xie, R. C. Che, M. Zhang, A. F. Wang, X. H. Chen, D. W. Shen, J. P. Hu, D. L. Feng, *Phys. Rev. X* **1** (2011) 021020
59. Hyejin Ryu, Milinda Abeykoon, Kefeng Wang, Hechang Lei, N. Lazarević, J. B. Warren, E. S. Bozin, Z. V. Popović, C. Petrovic, *Phys. Rev., B* **91** (2015) 184503
60. Hyejin Ryu, Kefeng Wang, M. Opačić, N. Lazarević, J. B. Warren, Z. V. Popović, C. Petrovic, *Phys. Rev., B* **92** (2015) 174522
61. M. Opačić, N. Lazarević, M. Šćepanović, H. Ryu, H. Lei, C. Petrovic, Z. V. Popović, *J. Phys.: Cond. Matter* **27** (2015) 485701
62. W. Bao, G. N. Li, Q. Huang, G. F. Chen, J. B. He, M. A. Green, Y. Qiu, D. M. Wang, J. L. Luo, M. M. Wu, *Chin. Phys. Lett.* **30** (2013) 027402
63. G. Huan, M. Greenblatt, *J. Less-Common Met.* **156** (1989) 247
64. M. Opačić, N. Lazarević, M. M. Radonjić, M. Šćepanović, H. Ryu, A. Wang, D. Tanasković, C. Petrovic, Z. V. Popović, *J. Phys.: Cond. Matter* **28** (2016) 485401
65. J. R. Neilson, A. Llobet, A. V. Stier, L. Wu, J. Wen, J. Tao, Y. Zhu, Z. B. Tesanovic, N. P. Armitage, T. M. McQueen, *Phys. Rev., B* **86** (2012) 054512
66. H. Lei, M. Abeykoon, K. Wang, E. S. Bozin, H. Ryu, D. Graf, J. B. Warren, C. Petrovic, *J. Phys.: Cond. Matter* **26** (2014) 015701
67. N. Lazarević, M. Radonjić, M. Šćepanović, H. Lei, D. Tanasković, C. Petrovic, Z. V. Popović, *Phys. Rev., B* **87** (2013) 144305
68. H. Lei, M. Abeykoon, E. S. Bozin, K. Wang, J. B. Warren, C. Petrovic, *Phys. Rev. Lett.* **107** (2011) 137002
69. H. Lei, M. Abeykoon, E. S. Bozin, C. Petrovic, *Phys. Rev., B* **83** (2011) 180503(R)
70. X. Ding, D. Fang, Z. Wang, H. Yang, J. Liu, Q. Deng, G. Ma, C. Meng, Y. Hu, H.-H. Wen, *Nat. Commun.* **4** (2013) 1897
71. S.-M. Huang, C.-Y. Mou, T.-K. Lee, *Phys. Rev., B* **88** (2013) 174510
72. D. Tan, C. Zhang, C. Xi, L. Ling, L. Zhang, W. Ton, Y. Yu, G. Feng, H. Yu, L. Pi, Z. Yang, S. Tan, Y. Zhang, *Phys. Rev., B* **84** (2011) 014502
73. J. Yang, B. Chen, H. Wang, Q. Mao, M. Imai, K. Yoshimura, M. Fang, *Phys. Rev., B* **88** (2013) 064406
74. A. M. Zhang, K. Liu, J. H. Xiao, J. B. He, D. M. Wang, G. F. Chen, B. Normand, Q. M. Zhang, *Phys. Rev., B* **85** (2012) 024518
75. A. M. Zhang, K. Liu, J. B. He, D. M. Wang, G. F. Chen, B. Normand, Q. M. Zhang, *Phys. Rev., B* **86** (2012) 134502
76. A. Ignatov, A. Kumar, P. Lubik, R. H. Yuan, W. T. Guo, N. L. Wang, K. Rabe, G. Blumberg, *Phys. Rev., B* **86** (2012) 134107
77. M. Cardona, *NATO ASI Ser., B* **372** (2002) 257.
78. N. Lazarević, H. Lei, C. Petrovic, Z. V. Popović, *Phys. Rev., B* **84** (2011) 214305
79. H. Hong, H. Steinfink, *J. Solid State Chem.* **5** (1972) 93

80. H. Lei, H. Ryu, V. Ivanovski, J. B. Warren, A. I. Frenkel, B. Cekic, W.-G. Yin, C. Petrovic, *Phys. Rev., B* **86** (2012) 195133
81. Z. V. Popović, M. Šćepanović, N. Lazarević, M. Opačić, M. M. Radonjić, D. Tanasković, H. Lei, C. Petrovic, *Phys. Rev., B* **91** (2015) 064303
82. W. Reiff, I. Grey, A. Fan, Z. Eliezer, H. Steinfink, *J. Solid State Chem.* **13** (1975) 32
83. Z. S. Gönen, P. Fournier, V. Smolyaninova, R. Greene, F. M. Araujo-Moreira, B. Eichhorn, *Chem. Mater.* **12** (2000) 3331
84. J. B. He, D. M. Wang, H. L. Shi, H. X. Yang, J. Q. Li, G. F. Chen, *Phys. Rev., B* **84** (2011) 205212.